Floris F. Noordhoek Hegt

Delft University of Technology

Atmospheric Water Extraction

Fresh Water Production Using
Ocean Thermal Energy

Floris F. Noordhoek Hegt

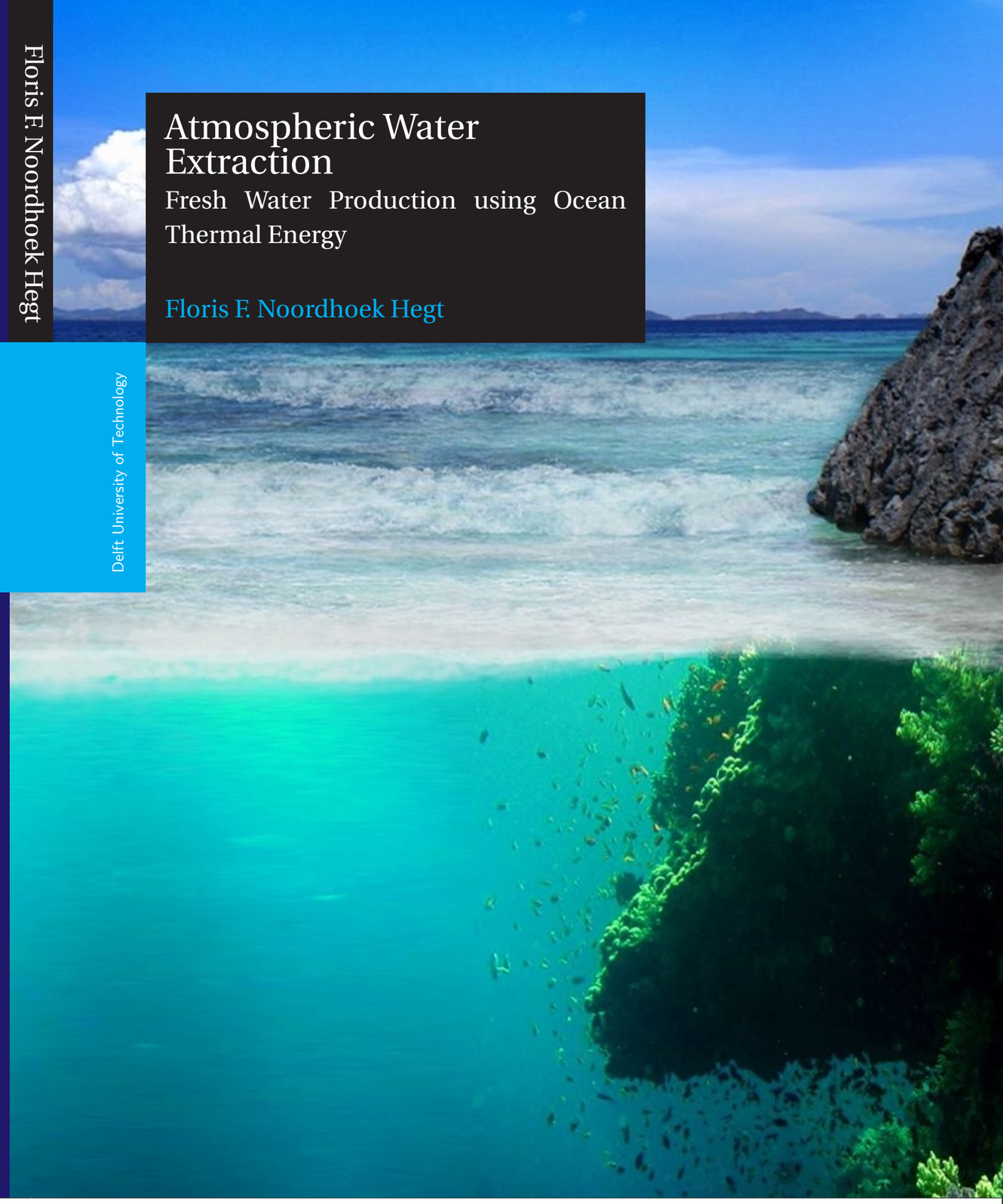

Atmospheric Water Extraction

Fresh Water Production using Ocean Thermal Energy

Floris F. Noordhoek Hegt

TU Delft Delft University of Technology

Challenge the future

Atmospheric Water Extraction

Fresh Water Production using Ocean Thermal Energy

by

Floris F. Noordhoek Hegt

to obtain the degree of Master of Science
in Sustainable Process & Energy Technology
at the Delft University of Technology,
to be defended publicly on August 24, 2017 at 10:00.

Student number:	4023455	
Report number:	-	
Project duration:	August 15, 2016 – August 24, 2017	
Thesis committee:	Dr. ir. C. A. Infante-Ferreira,	TU Delft, supervisor
	Prof. dr. ir. T. J. H. Vlugt,	TU Delft
	Dr. ir. M. J. B. M. Pourquie,	TU Delft
	Ir. B. J. Kleute,	Bluerise B. V.

This thesis is confidential and cannot be made public until August 24, 2022

TU Delft

Preface

This thesis project validates a fresh water production model with an experimental fresh water production setup that was previously designed by Lopez [30] and previously researched by van der Drift [49]. The fresh water production configuration makes use of high temperature and high relative humidity air in the tropics and condenses it against a cooled fresh water loop in a packed bed column. The system is expected to deliver fresh water at a competitive level once built at a larger scale.

The goal of this thesis is to finalize the experimental setup, restructure the model, and validate outputs from the model with the outputs from the experimental setup. This model can later be used to validate the possibility of Ocean Thermal Water Production (OTWP) at a competitive level, i.e. compete against desalination processes such as reverse osmosis and thermal desalination plants.

During the time frame of this master thesis project, I have had the pleasure to meet and work with many different people who each in their own way have helped me to complete this project. I would like to start by thanking the people at Bluerise for this wonderful opportunity and for the fun times in the office, during lunch, or at the ping pong table. Berend, Remi, Joost, Paul, Bram, and the Bluerise students, I thoroughly enjoyed working with all of you the past year and watching you bring this company one step closer to success.

This project could not have been done without the help of Tijmen Salet, my first partner in crime working on the OTWP experimental setup in September. Shortly after, a great team of BEP students helped to finalize the OTWP experimental setup until February, ensuring the outcome of the first useful experimental data and the start of the validation process. Thijs de Vries, Duco Delver and Erik van de Zande, many thanks to all of you. Many thanks also to Kees Aantjes, for the endless experimental work during lab hours and for the enjoyable company after lab hours. To Lieke van der Most, my successor for the OTWP project, it was great working with you over the summer, and I am interested to see where you will take this project in the future.

Throughout the year there has always been one person continuously helping and guiding his students on their way to obtaining the ir. title, building the next generation of engineers: Dr. ir. Infante Ferreira, I am forever grateful. Finally, I would like to thank my friends and family, for their endless love and support, and helping me get through the sometimes difficult times during this final project.

Floris F. Noordhoek Hegt
Delft, August 2017

Summary

Many regions in the world depend heavily on expensive desalinated water for fresh water consumption, in particular tropical areas. Current mainstream desalination technologies (Reverse Osmosis and Multi-Stage Flash Evaporation) are quite energy intensive and thus costly.

Today's challenge is to design a desalination system that could run with local available renewable energy and provide affordable fresh water, even in the most arid environments. A potential fresh water production method that differs from mainstream technologies is Ocean Thermal Water Production (OTWP). This method makes use of high temperature and high relative humidity air in the tropics and condenses it against a cooled fresh water loop in a packed bed column. The system is expected to deliver fresh water at a competitive level once built at a larger scale.

This master thesis project improves a previously researched OTWP model and validates the model by testing its output values against experiments done using an experimental setup at the TU Delft P&E laboratory.

Taking into account the previous work done during the thesis of van der Drift [49] and Lopez [30], the theoretical background for building an OTWP model has been further described and expanded in this thesis. Three different direct contact condensation theories have been thoroughly examined. The first two theories suggest that heat and mass in the DCD are transferred through a constant laminar film on the packing [38] [1] [4]. The third theory is an add on to the laminar film model, and suggests that heat and mass is also transferred through the creation and dynamics of small droplets within packings [34].

The model and its 4 main submodels are fine-tuned to be able to reproduce the thermodynamics occurring in the experimental setup. The model is tested under different steady state conditions using experiments, to provide insight on the model's robustness and reliability. The final improved simulation model is used to present conclusions on heat transfer, mass transfer and water production rates for the experimental setup. A brief economic analysis of the system is performed to arrive at an energy price of water for the OTWP experimental system.

Although the final energy price for the OTWP setup is quite unfavorable, 14 kWh/m^3 as opposed to 2-3.5 kWh/m^3 for current desalination systems, tips to improve a possible future pilot facility are proposed. Here high yield and low cost are key requirements, and the design of a future pilot facility needs to be optimized using these two pillars.

Contents

List of Figures xi

List of Tables xv

1 Introduction 1
- 1.1 Scope of the Research. . . . 3
- 1.2 Previous Work 3
  - 1.2.1 van der Drift Master Thesis 2014 3
  - 1.2.2 Bauer et al. Bachelor Thesis 2014 3
  - 1.2.3 Kreuk et al. 2015. . . . 4
  - 1.2.4 Lopez 2016 4
  - 1.2.5 Salet 2016. . . . 5
  - 1.2.6 Delver et al. 2017 5
- 1.3 Objectives. . . . 5
- 1.4 Approach 6
- 1.5 Report Organization 7

2 Theoretical Background 9
- 2.1 DCH-DH Condenser Model 10
- 2.2 Mass and Heat Transfer analysis, Humidification 12
  - 2.2.1 Mass Transfer Liquid Side 13
  - 2.2.2 Mass Transfer Gas Side. . . . 14
  - 2.2.3 Mass Transfer Evaporation 15
  - 2.2.4 Heat Transfer Liquid Side 17
  - 2.2.5 Heat Transfer Gas Side 19
  - 2.2.6 Heat Transfer Packing 21
- 2.3 Mass and Heat transfer Analysis, Dehumidification. . . . 21
  - 2.3.1 Mass Transfer Condensation 22
  - 2.3.2 Heat Transfer Liquid and Gas Side 23

3 Mass and Heat Transfer Correlations 27
- 3.1 Proof of heat and mass transfer analogy. . . . 27
- 3.2 Heat Transfer Correlations. . . . 29
- 3.3 Mass Transfer Correlations 30
  - 3.3.1 Klausner/Onda correlations 30
  - 3.3.2 Billet & Schultes Correlation 32
  - 3.3.3 Mackowiak's correlation 33
- 3.4 Pressure Drop 36
  - 3.4.1 Mackowiak Pressure Drop. . . . 36
  - 3.4.2 Billet & Schultes Pressure Drop. . . . 39
  - 3.4.3 Flooding Factor 39

4 Packed Bed Column Model **43**
4.1 Introduction . . . 43
4.2 Condenser . . . 45
4.2.1 Mass Flux Loop . . . 45
4.2.2 Temperature Loop . . . 46
4.3 Humidifier . . . 47
4.3.1 Explanation of Humidifier Model . . . 47
4.4 Heat Exchanger . . . 48
4.4.1 LMTD Working Principle . . . 49
4.4.2 Pressure Drop Heat Exchanger . . . 52
4.5 Pressure Loss Total System. . . . 53
4.5.1 Calculation Pressure Drop Piping . . . 54
4.5.2 Calculation other pressure drops. . . . 56

5 Validation **59**
5.1 Base Case Evaluation and Validation. . . . 62
5.1.1 Heat Transfer Evaluation . . . 62
5.1.2 Pressure Drop Evaluation . . . 66
5.1.3 Explanation of mass transfer and techno economic analysis . . . 67
5.1.4 Validation mass transfer and techno economics . . . 68
5.2 Changes in Relative Humidity. . . . 70
5.2.1 Heat Transfer . . . 70
5.2.2 Pressure Drop . . . 71
5.2.3 Mass transfer and techno economics . . . 72
5.3 Changes in nozzle type, inlet water temperature and air flow . . . 73
5.3.1 Heat transfer . . . 74
5.3.2 Pressure drop . . . 74
5.3.3 Mass transfer and techno economics . . . 75
5.4 Changes in Packing Height . . . 76
5.4.1 Heat transfer . . . 76
5.4.2 Pressure drop . . . 77
5.4.3 Mass transfer and techno economics . . . 77
5.5 Importance Evaporative Cooling . . . 79

6 Conclusions and Recommendations **81**
6.1 Main Conclusions . . . 81
6.2 Optimization Pilot Plant . . . 82
6.3 Improvements Experimental Setup: . . . 83
6.4 Recommendations: . . . 84

A Commissioning **87**
A.1 Analysis of Main Components . . . 87
A.1.1 Pumps & Nozzle . . . 88
A.1.2 **Nozzle** . . . 89
A.1.3 Heat Exchanger . . . 90
A.1.4 Direct Contact Condenser . . . 91
A.1.5 Tropical Air Generator . . . 93
A.1.6 Air Fan . . . 94

A.2 Methodology of Experiment 94
B Start-up and Shutdown of Experiment 97
C Measurement Scheme 103
D Billet & Schultes 107
E Packing Tables from Mackowiak 111
F MaxiPass 117
G Model Table Output 121
H Table Output Lopez Cond. 123
I Model Inputs 125
Bibliography 129

List of Figures

1.1 Humid air condensation on cold water pitcher 1
1.2 Natural Water Cycle, http://earthobservatory.nasa.gov/Features/Water/page2.php 2

2.1 Cooling Tower Diagram, obtained from http://www.coolingtowerproducts.com 9
2.2 Schematic representation of the DCD with differential control volume for liquid/gas heat and mass transfer with countercurrent flow, for evaporative cooling and cooling at saturation 11
2.3 Mollier Diagram showing adiabatic cooling (red line), cooling (blue line), and condensation along the saturation curve (yellow line) 13
2.4 liquid mass control volume 14
2.5 air/vapor mass control volume 15
2.6 Heat transfer between the packing, the liquid and the air/vapor mixture . . . 17
2.7 liquid enthalpy control volume 18
2.8 liquid specific enthalpy control volume 19
2.9 air enthalpy control volume 19
2.10 air specific enthalpy control volume 20
2.11 packing heat control volume 21
2.12 difference between control volumes during evaporation (humidification) and condensation (dehumidification) 22
2.13 Heat transfer between the packing, the liquid and the air/vapor mixture . . . 23
2.14 total liquid enthalpy control volume 24
2.15 total air enthalpy control volume 24
2.16 total liquid specific enthalpy control volume 25
2.17 total air specific enthalpy control volume 25

3.1 Seperation efficiency for 3 different Mellapak packings 41

4.1 Solidworks representation of the OTWP experimental setup 43
4.2 Schematic representation of the packed bed column model 44
4.3 Representation of condenser column 45
4.4 16 mm Pall rings random packing distributed in the condenser column 45
4.5 Solidworks representation of humidifier in the experimental setup 47
4.6 Solidworks representation of heat exchanger in the experimental setup 48
4.7 Redenko Cetetherm 410 Heat Exchanger in the experimental setup 48
4.8 Experimental data used for linear regression analysis to find constants z and w 50
4.9 Schematic representation of a counter current flow plate heat exchanger . . . 51
4.10 example of a countercurrent plate heat exchanger temperature diagram . . . 51
4.11 Correction factor F_t as a function of the NTU and number of passes [43] . . . 52
4.12 Counter-current flow, 1 pass, 5 channels per pass, 8 thermal plates, 10 plates total [43] 52

4.13 Counter-current flow, 2 passes, 5 channels per pass, 18 thermal plates, 20 plates total [43] . . . 52
4.14 Representation of piping in the experimental setup . . . 53
4.15 Moody Diagram from L.F. Moody [37] . . . 55
4.16 A representation of a disk gate valve, this is used to model the nozzle constriction as K-factors for this valve are available . . . 56
4.17 A representation of condenser column with air flow (red arrows) and the nozzle constriction (red cilinder) . . . 56

5.1 Representation of Experimental Setup showing the flow rate through the condenser as well as labelling the 7 main components of the system . . . 59
5.2 P&ID representation of the different sensors in the condenser column as well as the heights of each temperature sensor (as also used in the model) . . . 60
5.3 Visual representation of condenser column showing the location of the sensors. TT = temperature sensor, HT = humidity sensor, PT = pressure sensor and FT = flow sensor . . . 60
5.4 Diagram showing how OTEC waste water is utilized in the OTWP cycle . . . 62
5.5 Base case Klausner et al./Onda et al. comparison temperature curves . . . 63
5.6 Base case Klausner et al./Onda et al. comparison packing temperature . . . 63
5.7 Base case Klausner et al./Onda et al. comparison air temperature . . . 63
5.8 Base case Klausner et al./Onda et al. comparison water temperature . . . 63
5.9 Base case Billet & Schultes comparison temperature curves . . . 63
5.10 Base case Billet & Schultes comparison packing temperature . . . 63
5.11 Base case Billet & Schultes comparison air temperature . . . 64
5.12 Base case Billet & Schultes comparison water temperature . . . 64
5.13 Base case Mackowiak comparison temperature curves . . . 64
5.14 Base case Mackowiak comparison packing temperature . . . 64
5.15 Base case Mackowiak comparison air temperature . . . 64
5.16 Base case Mackowiak comparison water temperature . . . 64
5.17 A psychrometric chart showing the amount of water transferred between 28 °C and 80% RH and 12 °C and 100% RH at atmospheric pressure . . . 65
5.18 Base case Billet & Schultes comparison pressure drop . . . 66
5.19 Base case Billet & Schultes comparison pressure drop (ignoring height without packing) . . . 66
5.20 Base case Mackowiak comparison pressure drop . . . 66
5.21 Base case Mackowiak comparison pressure drop (ignoring height without packing) . . . 66
5.22 70% RH Billet & Schultes comparison temperature curves . . . 70
5.23 90% RH Billet & Schultes comparison temperature curves . . . 70
5.24 Wall wipers around a Mellacarbon packing used in to redistribute water into the packing . . . 70
5.25 Rear view of inlet air flow experimental setup . . . 71
5.26 Air flow CFD simulation to model starting height of packing. Picture taken during a meeting with Sulzer Chemtech [45] . . . 71
5.27 70% RH Pressure Drop Billet & Schultes . . . 71
5.28 90% RH Pressure Drop Billet & Schultes . . . 71

5.29 Total Temperature Distribution Billet & Schultes for MP125 nozzle, $T_{L,in}$ = 8 °C and air flow rate = 0.05795 kg/s 74
5.30 Water Temperature Distribution Billet & Schultes for MP125 nozzle, $T_{L,in}$ = 8 °C and air flow rate = 0.05795 kg/s 74
5.31 Air Temperature Distribution Billet & Schultes for MP125 nozzle, $T_{L,in}$ = 8 °C and air flow rate = 0.05795 kg/s 74
5.32 Packing Temperature Distribution Billet & Schultes for MP125 nozzle, $T_{L,in}$ = 8 °C and air flow rate = 0.05795 kg/s 74
5.33 Billet & Schultes comparison pressure drop for MP125 nozzle, $T_{L,in}$ = 8 °C and air flow rate = 0.05795 kg/s 75
5.34 Mackowiak comparison pressure drop for MP125 nozzle, $T_{L,in}$ = 8 °C and air flow rate = 0.05795 kg/s 75
5.35 690 mm packing Billet & Schultes comparison temperature curves 76
5.36 200 mm packing Billet & Schultes comparison temperature curves 76
5.37 690 mm Pressure Drop Billet & Schultes 77
5.38 200 mm Pressure Drop Billet & Schultes 77
5.39 Base case 70% RH Billet & Schultes temperature comparison evaporative cooling vs no evaporative cooling 79
5.40 Base case 70% RH Billet & Schultes pressure drop comparison evaporative cooling vs no evaporative cooling 79
5.41 Base case 70% RH Billet & Schultes humidity comparison evaporative cooling vs no evaporative cooling 79
5.42 Base case 70% RH Billet & Schultes water production comparison evaporative cooling vs no evaporative cooling 79

A.1 3D model design 87
A.2 Fresh and salt water pumps in the experimental setup 88
A.3 Salt and Fresh Water Pump Characteristics. Ideal operating points calculated according to Lopez [30] values 89
A.4 Solidworks representation of heat exchanger in the experimental setup 90
A.5 Redenko Cetetherm 410 Heat Exchanger in the experimental setup 90
A.6 Representation of condenser column 91
A.7 16 mm Pall rings random packing distributed in the condenser column 91
A.8 Solidworks representation of water tray in the experimental setup 92
A.9 Representation of weightscale used to measure water production in the experimental setup 92
A.10 Solidworks representation of humidifier in the experimental setup 93
A.11 Solidworks representation of the air fan in the experimental setup 94

List of Tables

5.1 Base case settings for experiment 60
5.2 Base case evaluation water production, pressure drop and energy consumption 68
5.3 Base case error evaluation between deviations experiment and model 68
5.4 Evaluation water production, pressure drop and energy consumption as well as model error deviations at 70% RH 72
5.5 Evaluation water production, pressure drop and energy consumption as well as model error deviations at 90% RH 72
5.6 Experiment with new nozzle, higher air flow rate and lower inlet water temperature 73
5.7 Evaluation water production, pressure drop and energy consumption as well as model error deviations for MP125, 50 L/s air flow rate and 8 °C water temp. inflow 75
5.8 Evaluation water production, pressure drop and energy consumption as well as model error deviations for 690 mm packing height 78
5.9 Evaluation water production, pressure drop and energy consumption as well as model error deviations for 200 mm packing height 78

A.1 Spraybest Nozzle Comparison 90

D.1 Billet and Schultes Characteristics for Random Packings [7] [8] [9] [42] [47] . . 108
D.2 Billet and Schultes Characteristics for Structured Packings [7] [8] [9] [42] . . . 109

Nomenclature

Symbols	Units	Description
A	m^2	area
a	m^2/m^3	specific surface area
a_h	m^2/m^3	hydraulic surface area
a_w	m^2/m^3	wetted/interfacial surface area
B_0	-	constant dependent on heat exchanger cross-sectional shape
B_1	-	constant dependent on heat exchanger corrugation pattern
B_{pl}	m	heat exchanger plate width
C	mol/m^3	molar concentration
c	kg/m^3	mass concentration
C_1	-	Packing specific constant Mackowiak (appendix E)
C_2	-	Packing specific constant Mackowiak (appendix E)
C_3	-	Packing specific constant Mackowiak (appendix E)
C_4	-	Packing specific constant Mackowiak (appendix E)
C_5	-	constant dependent on heat exchanger corrugation pattern
C_D	-	empirical constant for calculating the sauter mean diameter (section 3.3.3)
C_a	-	empirical constant for determining saturation pressure (section 2.3.1)
C_b	-	empirical constant for determining saturation pressure (section 2.3.1)
C_c	-	empirical constant for determining saturation pressure (section 2.3.1)
C_d	-	empirical constant for determining saturation pressure (section 2.3.1)
$C_{fl,0}$	-	empirical constant Mackowiak for determining the gas flooding velocity 3.4.3
C_G	-	packing specific constant Billet&Schultes (appendix D)
C_h	-	packing specific constant Billet&Schultes (appendix D)
C_L	-	packing specific constant Billet&Schultes (appendix D)
$C_{pack,0}$	-	packing specific constant Billet&Schultes (appendix D)
Cp	J/kg K	isobaric specific heat capacity
C_V	-	empirical constant for the Frossling equation (section 3.3.3)
D	m	diameter
D_D	m	Sauter mean droplet diameter
D_h	m	hydraulic diameter of packed beds
D_p	m	particle diameter of a packing acc. to Mackowiak
$\mathbb{D}$	m^2/s	mass diffusion coefficient (i.e. mass diffusivity)
F_G	$Pa^{0.5}$	gas load factor, $F_G = u_G\sqrt{\rho_G}$
F_{fl}	-	flooding factor
FR	-	flow ratio $\dot{V}_L/\dot{V}_G$
FR_{fl}	-	flow ratio at flooding point $\dot{V}_L/\dot{V}_{G,fl}$
f_D	-	Darcy-Weisbach friction factor
$f(a,b)$	-	function of arbitrary variable "a" and "b"
G	kg/m^2s	air mass flux
g	m/s^2	acceleration of gravity, $g = 9.807\ m/s^2$

H	J	enthalpy
h	J/kg	specific enthalpy
h_{fg}	J/kg	specific enthalpy of evaporation
$HETP$	m	height equivalent to a theoretical plate
J	mol/m^{2}s	Diffusion flux
K	-	K-factor (Wall factor)
k	m/s	mass transfer coefficient
l_D	m	mean contact path of droplet acc. Mackowiak
L	kg/m^{2}s	liquid mass flux
L_{pl}	m	heat exchanger plate length
LH	m^3/m^3	liquid hold-up
l	m	characteristic length
M	kg/kmol	molecular weight
m	kg	mass
$\dot{m}$	kg/s	mass flow
NTU	#	the number of transfer units
n_1	-	exponent evaluated from experimental data
n_2	-	exponent evaluated from experimental data
n_{pl}	-	number of plates
p	Pa	pressure
Q	W	heat flow
R	J/mol K	universal gas constant
S_c	kg/m^{3}s	mass concentration source/sink
S_T	K/s	temperature source/sink
T	K	temperature
t	s	time
U	W/m^{2}K	overall heat transfer coefficient
u	m/s	mean velocity of the fluid
$\bar{u}_G$	m/s	effective gas velocity = $\frac{u_G}{\epsilon}$ (section 3.4.1)
$\bar{u}_L$	m/s	effective liquid velocity = $\frac{u_L}{LH}$ (section 3.3.3)
u_R	m/s	relative phase velocity = $\frac{u_G}{\epsilon - LH} + \frac{u_L}{LH}$
V	m^3	volume
$\dot{V}$	m^3/s	volume flow rate
v	m/s	velocity in the y direction
$\overrightarrow{v}$	m/s	velocity vector
$\dot{W}$	W	Energy consumption rate
X	-	arbitrary variable
x	m	x coordinate, length in x direction
y	m	y-coordinate, length in y direction
z	m	z-coordinate, height
Z	m	Column height

Greek symbols

α	W/m^{2}K	heat transfer coefficient
β	°	wave angle
δ	m	plate thickness
ϵ	m^3/m^3	void fraction
ϵ_{pipe}	m	roughness of pipe
$\frac{\epsilon}{D}$	-	roughness ratio
η	-	efficiency
κ	m^2/s	thermal diffusivity
λ	W/m K	thermal conductivity
λ_{df}	-	Darcy friction factor
μ	Pa s	dynamic viscosity
ν	m^2/s	kinematic viscosity
ξ	%	relative error
ρ	kg/m^3	density
σ	N/m	surface tension
τ	s	contact time
ϕ	%	relative humidity
ϕ_{pack}		packing form factor [32]
ϕ_{pl}		plate area enlargement factor
ϕ_v	m^3/m^3	volume fraction
ψ	[-]	the drag coefficient (i.e.resistance coefficient)
$\psi_{G,L}$	[-]	the pseudo drag coefficient, a term needed to define the real drag coefficient under two-phase flow conditions
ω	kg/kg	humidity ratio
∇	1/m	gradient
$\nabla\cdot$	1/m	divergence

Subscripts

A	arbitrary substance A
a	dry air
B	arbitrary substance B
b	bulk
c	cross section
c	cold-side
D	droplet (Mackowiak section 3.3.3)
d	dirt, fouling
dp	pressure difference
dynamic	moving
dz	height difference
e	effective
ec	evaporative cooling
evap	portion of liquid evaporated
exp	experimental
ext	external
fl	at flooding point
fw	fresh water
G	air/vapour mixture
HE	heat exchanger
h	hydraulic
h	hot-side
i	at interface (in chapter 2 denotes either salt or fresh water medium)
in	where the variable enters the condenser
L	water in liquid phase
l	at loading point
lm	logarithmic mean
m	mass
max	maximum
model	model
out	where the variable exits the condenser
p	particle of a packing
pack	packing
pipe	pipe
pl	plate
port	port of the heat exchanger
prod	production
S	Column
sat	saturated
static	not moving
st	steam
sw	seawater
T	thermal
T_G	air vapor temperature
T_L	fresh water temperature
table	reference to table in appendix
v	water in vapour phase
W	Wanted
w	wetted
z	at height z, z-coordinate
0	total

Abbreviations

AWE	Atmospheric Water Extraction
DCD	Direct Contact Dehumidifier
LMTD	Logarithmic Mean Temperature Difference
OTEC	Ocean Thermal Energy Conversion
OTWP	Ocean Thermal Water Production
P&E lab	Process and Energy laboratory at TU Delft
P&ID	Process and Instrumentation Diagram
RH	relative humidity
SDC	Seawater District Cooling
TAG	Tropical Air Generator
TU	Technical University

Dimensionless Numbers

$Fr_{La} = \frac{u_L^2 a}{g} = \frac{L^2 a}{\rho_L g}$	Froude number of liquid based on the specific area of the packing
$Le = \frac{\kappa}{\mathbb{D}}$	Lewis number
$Nu = \frac{\alpha l}{\lambda}$	Nusselt number
$Pr = \frac{Cp\mu}{\lambda}$	Prandtl number
$Re = \frac{\rho u D}{\mu} =$	Reynolds number
$Re_D = \frac{u_R D_D}{\nu_G}$	Reynolds number of the Sauter mean droplet diameter
$Re_{Ga} = \frac{\rho_G u_G}{a\mu_G}$	Reynolds number of gas based on the specific area of the packing
$Re_{Gw} = \frac{\rho_G u_G}{a_w \mu_G}$	Reynolds number of gas based on the specific wetted area of the packing
$Re_{Gp} = \frac{u_G D_p}{(1-\epsilon)\nu_G} K$	Reynolds number of gas based on the particle diameter acc. to Billet&Schultes (section 3.4.2)
$Re_{La} = \frac{\rho_L u_L}{a\mu_L}$	Reynolds number of liquid based on the specific area of the packing
$Re_{Lw} = \frac{\rho_L u_L}{a_W \mu_L}$	Reynolds number of liquid based on the specific wetted area of the packing
$Sc = \frac{\mu}{\rho \mathbb{D}}$	Schmidt number
$Sh_{Ga} = \frac{k_G a}{\mathbb{D}_G}$	Sherwood number gas based on the specific area of the packing
$Sh_{La} = \frac{k_L a}{\mathbb{D}_L}$	Sherwood number liquid based on the specific area of the packing
$We_{La} = \frac{L^2}{\rho_L \sigma_L a}$	Weber number of liquid based on the specific area of the packing

1 Introduction

Many regions in the world depend heavily on expensive desalinated water for its consumption, in particular tropical areas. Current mainstream desalination technologies (Reverse Osmosis and Multi-Stage Flash Evaporation) are quite energy intensive and thus costly. Today's challenge is to design a desalination system that could run with local available renewable energy and provide affordable fresh water, even in the most arid environments.

A potential fresh water production method that differs from mainstream technologies is Atmospheric Water Extraction (AWE). This method extracts fresh water out of air and may be explained as follows:

Imagine a cold water pitcher outside on a hot summer day (figure 1.1). Somehow the surface of the bottle becomes wet. The reason this happens is because outside air is being cooled by the cold surface of the pitcher. Due to the decrease in temperature, the air can hold less water, and thus water is extracted from the air onto the cold surface of the pitcher.

Figure 1.1: Humid air condensation on cold water pitcher

The two main problems for this method are finding an energy resource that can continuously cool the surface of the water pitcher and ensuring that the air has a high enough relative humidity to allow fresh water to be extracted.

Fortunately, an energy resource exists with such potential, namely the ocean. The oceans receive 70% of all sunlight that falls on the Earth, making them the largest solar collector. The sun's energy warms the surface water, which drives desalination through the natural water cycle (see figure 1.2). Studies have revealed that evaporation from oceans is the primary vehicle for driving moisture into our atmosphere, explaining the reason for high humidities near islands and coasts. Meanwhile, the deep ocean water remains cold. This year-round available ocean temperature gradient, which is highest in the tropics, could drive sea water desalination and enable fresh water production in an economic and ecological manner.

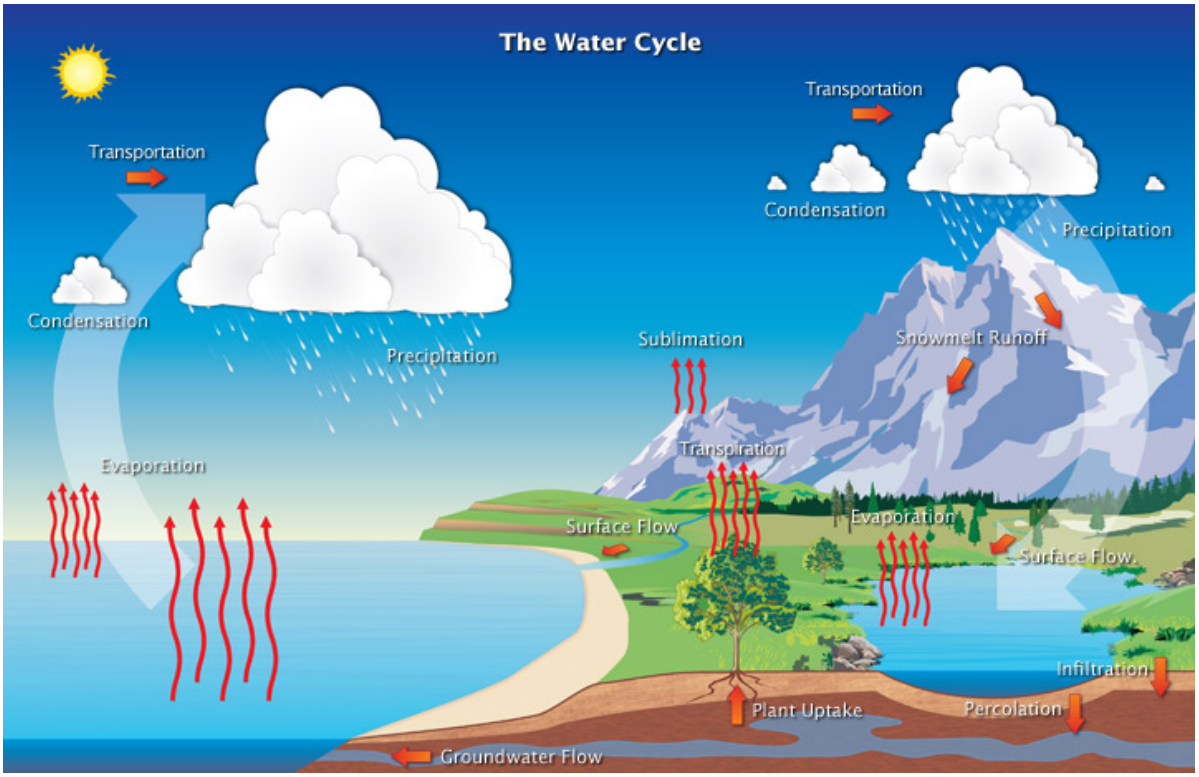

Figure 1.2: Natural Water Cycle, http://earthobservatory.nasa.gov/Features/Water/page2.php

A company currently investing in the thermal potential of the ocean is Bluerise. Bluerise was conceived in 2009 by a team of engineers at the TU Delft whom noticed the vast potential of the ocean's thermal energy storage in tropical regions. Their three main products consist of:

1. Ocean Thermal Energy Conversion (OTEC): A method of generating electricity using the temperature difference between the top and bottom layers of the ocean. Since this is the exact opposite of obtaining a temperature difference by delivering work, the process is also known as a reverse refrigeration cycle.

2. Seawater District Cooling (SDC): Cold deep seawater is pumped up and used for district cooling. This simple cooling method can easily replace energy intensive HVAC systems.

3. Ocean Thermal Water Production (OTWP): A fresh water production method using cold deep sea water as an energy source to drive AWE.

This thesis will focus on the third product, OTWP, and was made in collaboration with Bluerise and the TU Delft. The selected configuration for OTWP currently used by Bluerise is a direct contact condensation process. It makes use of high temperature and high relative humidity air in the tropics and condenses it against a cooled fresh water loop in a packed bed column. The cold seawater is used in an external heat exchanger to cool the fresh water loop. The system delivers fresh water and dehumidified air without the need of energy intensive equipment.

1.1. Scope of the Research

The main research topic is to investigate the applicability of AWE using relatively cold seawater that has already been used for OTEC. This will be done by building a python model and validating it with experiments using the experimental OTEC and OTWP setup located at the TU Delft.

After this research project, the python model can be used as a helpful tool for designing and optimizing a commercial OTWP plant in combination with an OTEC plant. The lab-scale experiments, aside from validation, can also provide useful information on the lifetime of such a system as well as the monitoring needed to keep it running.

1.2. Previous Work

Prior to this master thesis, research had already been done on OTWP for Bluerise. It is important to understand and verify previous work made on this topic to understand the decisions made up until now. Thus a short summary is given below of the different results and assumptions made in earlier studies.

1.2.1. van der Drift Master Thesis 2014

In 2014, van der Drift [49] made a techno-economic assessment of the OTWP system in combination with an OTEC plant. The dehumidification method, technical feasibility and economic feasibility of the dehumidifier were assessed. Three dehumidification methods were compared:

- Tube Condenser
- Compact Plastic Heat Exchanger
- Direct Contact Dehumidifier (DCD) consisting of a packed bed and external heat exchanger

The most cost effective (and thereby the best) method tested was the DCD with external heat exchanger, since:

1. The packed bed of a DCD method allows for a compact design and more efficient heat exchange, due to a larger specific heat transfer area

2. External heat exchange between sea water and fresh water significantly decreases cleaning and maintenance costs when compared with direct heat exchange between sea water and air.

A technical and economical feasibility study was conducted based on the DCD method. Van der Drift found that plate spacing in the external heat exchanger had a great impact on cost and energy requirements. By optimising the plate spacing a technically feasible configuration was found, with energy requirements of less than 2 kWh electricity per m^3.

1.2.2. Bauer et al. Bachelor Thesis 2014

During the thesis study of van der Drift, Bauer et al. [3] searched for the optimum air to water mass flow ratios for which the smallest surface area is needed in the DCD packed bed

column to reach saturation of water in air. This is important since the smaller the surface area needed for saturation, the smaller the final setup needs to be to condense the required amount of water in the packed bed column.

Bauer et al. found that at a constant packed bed column height and diameter, the variation of the air to water ratio had little to no influence on water production when the air mass flow was kept constant. In contrary, when keeping the water mass flow constant, and varying the gas mass flow, a decrease in water production was found. This means that there is an optimum gas mass flow for a certain column height and diameter. The main conclusions of their research can be summed up as follows:

- If the packed bed height increases, the gas mass flow should increase for optimum performance. There is 1 optimum gas mass flow for a certain packed bed height.
- Liquid mass flow is less important than gas mass flow when maximizing water production rates. The most important aspect is that the liquid mass flow is spread over the column evenly.
- a lower air to water ratio leads to lower saturation heights and thus a more efficient "water extraction" performance. However, the production of water is a direct result of condensation of vapor from air and thus requires an adequate air mass flow and an adequate gas-to-liquid contact surface area to ensure enough vapor is extracted.
- Using the flooding factor, the optimum gas to liquid ratio can be found for the highest contact surface area and therefore the highest water production rates. Yet, a flooding factor of 1 requires the most amount of energy input. An exact optimum leading to the most water production per unit of energy input still needs to be found.

Bauer et al. had also tested the significance of the evaporative cooling area on the packed bed, which was neglected by van der Drift. The conclusion was that the height needed for evaporative cooling is significant compared to the height of the packed bed. Therefore, the Matlab model designed by Bauer et al. used a laminar film evaporation model from Hirshburg and Florschuetz [23] to help simulate the heat and mass transfer method in the column described by Klausner et al.[27].

1.2.3. Kreuk et al. 2015

Kreuk et al. [28] designed the current experimental facility in Solidworks which was used as a building plan to build the facility. All the actuators in the facility are variable so that different conditions can be met. The location and placement of different sensors was also part of this bachelor thesis as well as an accuracy analysis of the sensors. Due to long delivery times and to no fault of their own, the setup was not yet finished when this group was done.

1.2.4. Lopez 2016

Following van der Drift and Bauer et al., and during the same time period as Kreuk et al., Lopez [30] was assigned to design and build an OTWP experimental facility using a DCD. Different methods of direct contact condensation were compared. Eventually the current

setup, using a random packing with stainless steel 16 mm Pall rings, was selected and built. Effects of new components used in the facility were added to the numerical model simulation, such as pressure loss due to piping as well as input requirements for the Tropical Air Generator (TAG). The numerical model was also converted from matlab to python.

Lopez explained that the flooding factor has to be around 0.7 for an optimal balance between water production and energy consumption. Thus for the experimental packed bed column, fresh water production is maximized using 0.19 kg/s air and 0.20 kg/s fresh water as inlet conditions.

A scale-up system for the Bluerise Ecopark as well as an initial economic assessment was done using results from the model. Due to the incompleteness of the model and due to the fact that results had not been validated yet with experiments, one should verify if the economic analysis as well as the scale-up report are still valid.

1.2.5. Salet 2016

At the beginning of September 2016, the start of this thesis began as well as the internship of T. Salet [41]. During this time period, research had already been done on the experimental setup as well as the python model, yet neither the setup nor the model worked appropriately. During his 3-month internship, Salet helped improve the experimental set-up, at the Process & Energy laboratory of the TU Delft, by evaluating components and sensors. If components were deemed broken or insufficient, a theoretical analysis was done to help improve that part of the system. Using knowledge obtained by working on the setup, Salet also helped improve python model simulations, in particular the heat exchanger and humidifier sub models.

1.2.6. Delver et al. 2017

Delver et al. [14] helped finalize and verify research done on components and sensors for the experimental set-up. Particularly useful was the research done on the pressure drop to obtain desired conditions when running experiments. This not only helped improve the laboratory setup, but the python model as well. The first lab experiments that obtained some favorable steady-state conditions were executed by Delver et al. These experiments also helped find possible errors in the python model, hereby improving its robustness. Obviously these experiments would not have worked out as well without the previous work of T. Salet [41].

1.3. Objectives

The main goal of this thesis project is to validate, improve and optimize a previously researched AWE method that enables fresh water production in tropical areas using cold sea water and humid air. It is to be validated if this method, a form of OTWP, will:

1. Be economically competitive with current water production methods, i.e. the cost of production per m^3 is equal to or lower than current production methods (e.g. thermal processes such as multistage flash or membrane processes such as reverse osmosis) which consume between 2-3.5 kWh/m^3.

2. Reduce the energy consumption as well as the carbon footprint of fresh water production

Taking into account the previous work done during the thesis of van der Drift [49] and Lopez [30], the following objectives have been derived from the main goal:

- Model Theory: Describe and expand the theoretical background used to develop a model for OTWP.
- Mass and Heat Transfer Correlations: Discuss different possible correlations that can be used to describe mass and heat transfer inside the condenser column.
- Improvement of Existing Model: Improve the theoretical model based on theory as well as experimental results, for instance:
  - Design and fulfill a measurement scheme under different operating conditions for the experimental setup and make sure these operating conditions are feasible (i.e. different flow rates, humidities, nozzle types, etc). Changes applied to the experimental facility, so that different experiments can be executed, have been documented in a commissioning report in Appendix A.
  - Include an analysis of the fresh water production model under different steady state conditions to test the robustness of the model (i.e. varying air humidity, temperature, etc)
  - Improve theory of the model. For instance, the pressure loss calculations as well as the humidifier calculations need to be improved. Also, the condensor model needs improvement as the calculations used do not always match the actual state of the process.
- Validation: Execute different sets of experiments to validate the available theoretical python model under different steady state conditions.
- Conclusions and Recommendations: Use the improved simulation model to propose system optimization modifications, such as:
  - Coming to conclusions on the techno economics by analyzing at which conditions the experimental OTWP setup has the highest water production and the lowest energy consumption. Use this analysis to suggest improvements needed to optimize a future pilot plant.
  - Researching the additional steps that need to be taken in order to transform the obtained atmospheric water into potable drinking water that can be supplied to consumers.

1.4. Approach

Commissioning of the lab-scale OTWP plant designed by Lopez [30] is to be finished first. The experimental setup's deficiencies, how they are solved, and how experiments are to be executed is explained in Appendix A. The numerical model developed in python by

Lopez [30] and Kreuk et al. [28] is improved in this work. Three direct contact condensation theories have been built in python and compared to each other using data obtained from experiments. The first two theories suggests that heat and mass in the DCD are transferred through a constant laminar film on the packing. The third theory is an add on to the laminar film model, and suggests that heat and mass is also transferred through growing droplets on packings. These droplets, once large enough, will split and fall through the column creating new smaller droplets, re-initiating the process. After working on the robustness of the model, testing different theories, and validating which model is best under different conditions using data obtained from the experimental facility, a brief economic analysis of the system is performed to arrive at a cost price of water for the OTWP system. High yield and low cost are key requirements, and the design of the future pilot facility needs to be optimized using these two pillars.

1.5. Report Organization

This report is organised approximately in the same manner as the objectives above have been formulated:

Chapter 2: Theoretical Background → Introduction of the theoretical background of the python model. How can the process taking place in the AWE system be modelled? How can these processes be described mathematically?

Chapter 3: Mass and Heat Transfer Correlations → Describe how mass and heat are transferred in the condenser column. Explain 3 methods for calculating mass and heat transfer coefficients inside the condenser as well the pressure drop over a packing height.

Chapter 4: Packed Bed Column Model → Explain structure of the packed bed model as well as the different sub models in it.

Chapter 5: Validation → Validate the python model using experiments from the experimental setup. How well does the python model predict experimental values?

Chapter 6: Conclusions and Recommendations → Briefly explain the main findings, summarize the ups and downs and point out recommendations to further develop the OTWP project. What factors are still missing and how can the project improve in the future?

2

Theoretical Background

The first widely used model to estimate heat and mass transfer associated with air/water systems is from Merkel in 1925 [36], which is used to analyze cooling towers (see figure 2.1). Cooling towers work in the exact opposite way as OTWP: cold air is blown into the tower or column which reduces the temperature of hot water entering from the top, leaving cold water as the end product. Due to the increase in temperature of the cold air during this process, the air is able to hold more water and thus water is evaporated into the air. In OTWP, the idea is to decrease the temperature of warm air using cold water so that fresh water is condensed from the air.

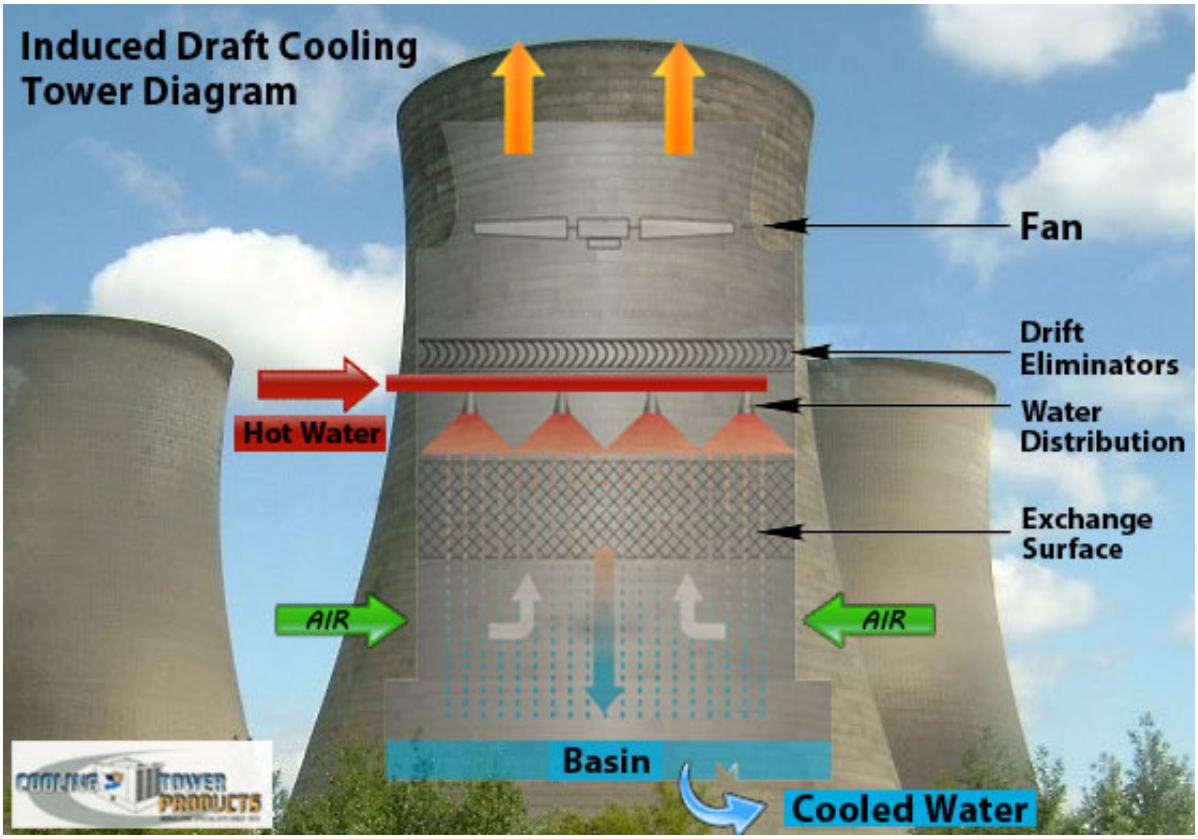

Figure 2.1: Cooling Tower Diagram, obtained from http://www.coolingtowerproducts.com

Merkel's analysis is known to underpredict the required cooling tower volume since it contains two restrictive assumptions:

1. on the water side, the mass loss by evaporation of water is negligible
2. the Lewis number is unity ($Le = \frac{\mathbb{D}_T}{\mathbb{D}_m} = \frac{Sc}{Pr}$ is a measure of the ratio between the thermal diffusivity and mass diffusivity, it is used to characterize fluid flows where there is simultaneous heat and mass transfer).

As also stated by Alnaimat et al. [1], improvements have been made throughout the years on Merkel's model:

- Baker and Shryock [2] provided a detailed analysis of Merkel's original work and clarified the error related to each specific assumption in Merkel's model
- Sutherland [46] included an analysis of water loss by evaporation yet ignored the interfacial temperature between liquid and air.
- Osterle [39] assumed saturated air throughout the whole process and that air in contact with the liquid film is saturated at the water temperature (i.e. the interfacial temperature is equal to the water temperature).
- El-Dessouky et al. [16] improved the analysis for counter flow cooling towers, yet assumed that the available interfacial area for heat transfer is the same as that of mass transfer, which is only true when the packing is thoroughly wetted and this is rare. Also, an empirical enthalpy equation is used for the air/vapor mixture which is only valid for temperatures between 10°C and 50°C.

The model presented by Klausner et al. [27] in 2006 does not require any of the assumptions used in prior works. The model includes the evaporation of water (left out by Baker and Shyrock [2]), the interfacial heat resistance between water and air (left out by Sutherland [46]), and the different interfacial areas for heat transfer and mass transfer (left out by Osterle [39] and El-Dessouky et al. [16]).

It is possible to use Klausner's cooling tower model and apply it for an OTWP model. As mentioned above, the OTWP process is exactly opposite of a cooling tower process, yet the formulations needed for the model stay the same. In fact, the steady state model has been tested already for direct contact condensation in packed beds by Li et al. [29]. This model is further improved in 2011 [1], where transient analysis of direct contact condensation in packed beds is also included.

The formulations derived by Klausner and Li et al. [27] [29] [1] are used to model the Direct Contact Humidifier-Dehumidifier (DCH-DH) process in the OTWP system. How the model works is explained in the next section.

2.1. DCH-DH Condenser Model

The DCH-DH model is based on a two-fluid model in which one-dimensional conservation equations for mass and energy are applied to a differential control volume for counter-current flow. One-dimensional treatment of the conservation equations is allowed due to the observation made by Li et al. [29] that replacing the area-averaged humidity (function of x and y at a certain height z) with the bulk humidity (constant at a certain height z), ω,

causes minimal error in predicting heat and mass transfer rates in packed beds.

For this OTWP configuration, the air/vapor mixture is blown from bottom to top (z-coordinate). Cold fresh water is sprayed in the column and falls from top to bottom due to gravity. While the air travels upwards, it is being cooled by the cold fresh water. The air becomes increasingly more saturated as it moves up the column (humidification), until eventually it is fully saturated and will start condensing water (dehumidification).

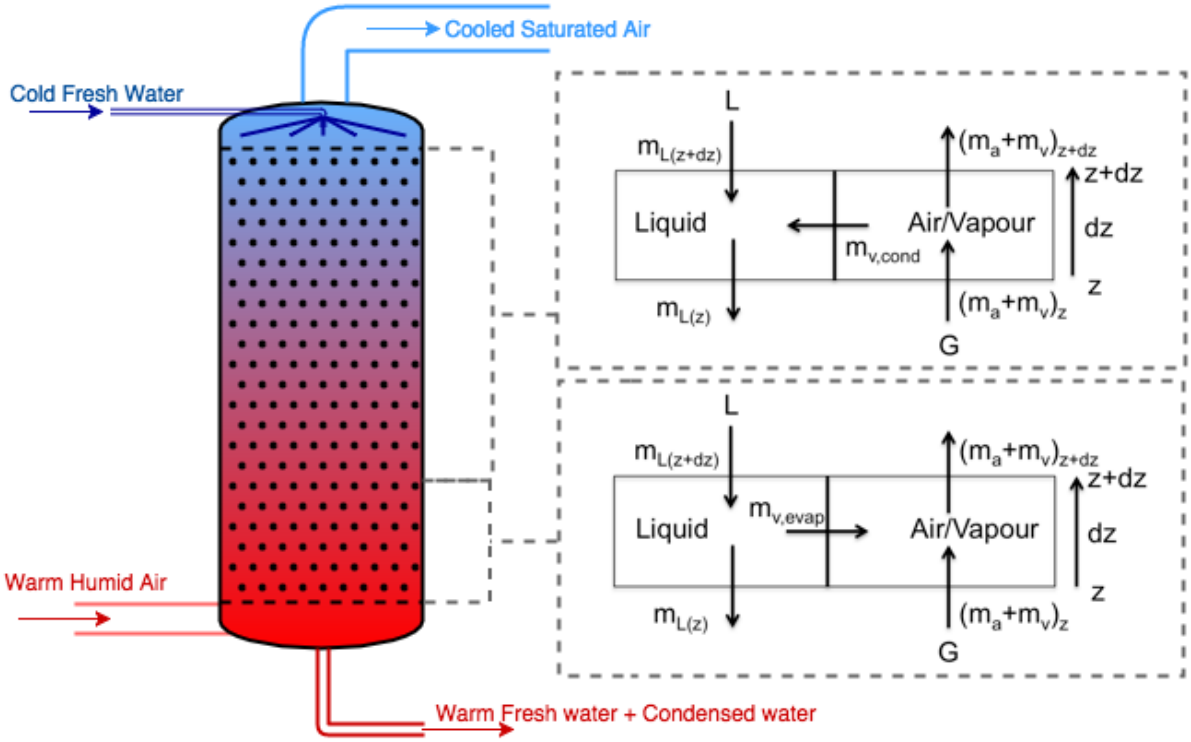

Figure 2.2: Schematic representation of the DCD with differential control volume for liquid/gas heat and mass transfer with countercurrent flow, for evaporative cooling and cooling at saturation

A step by step explanation of how the DCD model works numerically and generates its outputs is given below (also see figure 2.2):

1. The model starts its calculations at the bottom of the DCD. It works its way up the condenser using 1D mass and energy conservation equations to be used along the z-direction with step size dz.
2. The known inputs at the bottom ($z = 0$) are the inlet gas volumetric flow rate $\dot{V}_{G,in}$, the inlet gas temperature $T_{G,in}$ and the inlet gas relative humidity $\phi_{G,in}$. Since 3 state variables are known, the thermodynamic state of the system is known at this location. By using thermodynamic and transport property models such as Coolprop or Refprop, the specific enthalpy, the absolute humidity and the density of the gas can be obtained at this location. Using the volumetric flow rate, gas density and the absolute humidity, the inlet gas mass flow $\dot{m}_{G,in}$, dry air mass flow $\dot{m}_{a,in}$ and vapor mass flow $\dot{m}_{v,in}$ are obtained.
   An initial assumption is made for the outlet liquid mass flow $\dot{m}_{L,out}$ and the outlet

liquid temperature $T_{L,out}$. Since the cross sectional area of the condenser is known and constant, the gas mass flux G and liquid mass flux L are used for the iteration in the model instead of the mass flow. Also, the gas specific enthalpy h_G and liquid specific enthalpy h_L are used to iterate instead of the temperature so that there is no need to work with specific heat Cp.

3. Once the top of the DCD is reached ($z = 1$) the calculated inlet liquid mass flux $L_{z=1}$ and inlet liquid specific enthalpy $h_{L,z=1}$ are checked to see if they match the known liquid mass flux L_{in} and specific enthalpy $h_{L,in}$ at the top within the defined margin of error.
4. If one or both of the values are not within the margin of error, the process is restarted and the assumed liquid specific enthalpy and/or mass flux at the bottom is increased or decreased by a defined step size. Whether the values are increased or decreased depends on the calculated output value:
   (a) If the calculated value at $z = 1$ was too high the initial assumption at $z = 0$ is decreased by a defined step size.
   (b) If the calculated value at $z = 1$ was too low the initial assumption at $z = 0$ is increased by a defined step size.
5. The iteration process continues until both the calculated liquid mass flux and calculated liquid specific enthalpy at the top match the known mass flux and specific enthalpy inlet conditions of the liquid.

In the time period where the air is not yet saturated, either normal cooling or evaporative cooling can take place. During evaporative cooling (also known as adiabatic cooling), mass is transferred from the cold liquid water to the warm air/vapor mixture, which in turn cools the air/vapor mixture (see red line in figure 2.3). The blue line in figure 2.3 represents normal cooling until saturation. Both can be chosen in the OTWP model, yet research by Klausner et al. [27] shows air is cooled adiabatically towards saturation, and thus follows the red line. Once the air is fully saturated, dehumidification takes place. This process is shown by following the yellow line in figure 2.3, which literally represents cooling along the saturation curve, hereby condensing water. The process in the column can thus be split in two sections: the part where humidification takes place, and the part where dehumidification takes place. Both are explained separately below.

As a helpful side note when running through the model steps, remember that by convention for any arbitrary variable X and small step size dz: $\frac{\delta}{\delta z}(X)dz = X_{z+dz} - X_z$. Here $z + dz$ is a step upwards in the condenser column.

2.2. Mass and Heat Transfer analysis, Humidification

During humidification, mass transfer takes place from the cold water to the warm humid air. At the same time, mass transferred by the colder water will cool the warmer air vapor mixture through evaporative cooling (= energy transfer). In this section, the conservation of mass in the control volume is given first, and is followed by the conservation of energy (for each phase).

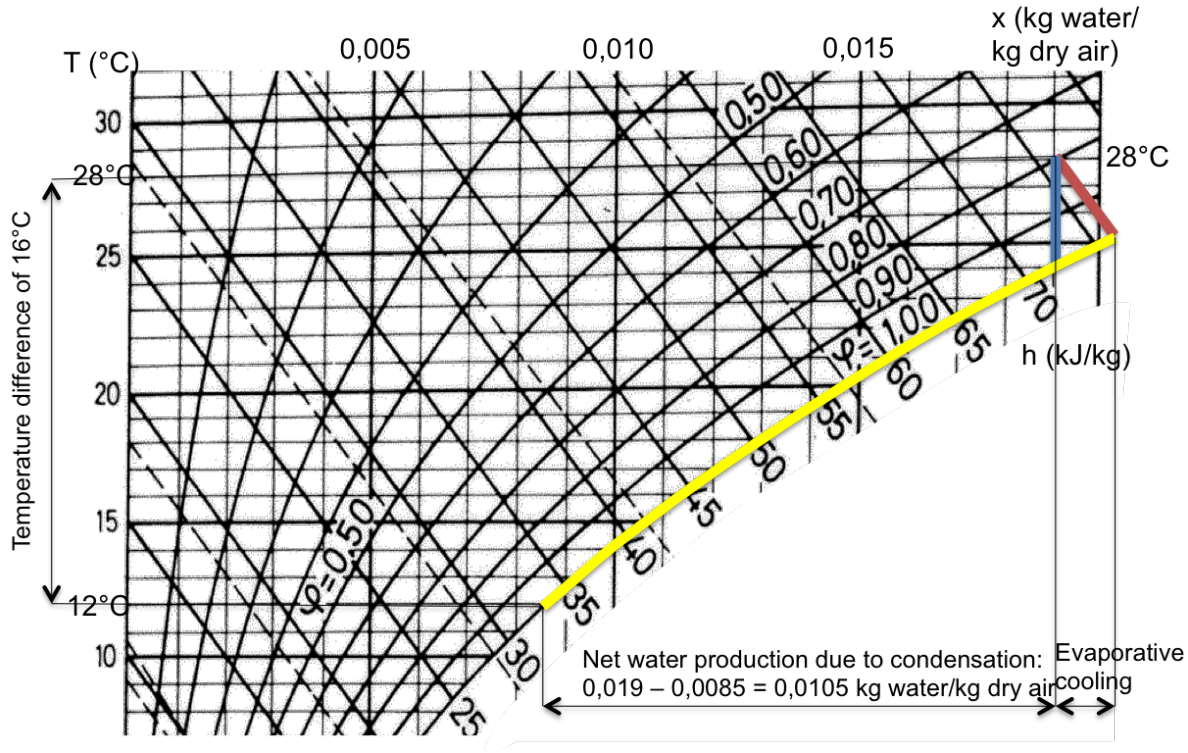

Figure 2.3: Mollier Diagram showing adiabatic cooling (red line), cooling (blue line), and condensation along the saturation curve (yellow line)

2.2.1. Mass Transfer Liquid Side

The conservation of mass applied to the liquid-phase of the control volume is

$$(\dot{m}_L)_{z+dz} - (\dot{m}_L)_z - d\dot{m}_{v,evap} = \frac{\delta}{\delta t}(m_L) = \frac{\delta}{\delta t}(\rho_L \phi_{v,L} A_c dz) \tag{2.1}$$

Here,

- $\dot{m}_L$ is the mass flow rate of the liquid
- $\dot{m}_{v,evap}$ is the mass flow rate of the portion of liquid evaporated
- m_L is the mass of the liquid
- ρ_L is the liquid density
- $\phi_{v,L}$ is the liquid volume fraction
- A_c the cross sectional area of the column
- dz the step size in height over the column

Noting that

$$(\dot{m}_L)_{z+dz} - (\dot{m}_L)_z = \frac{\delta}{\delta z}(\dot{m}_L) dz \tag{2.2}$$

then equation 2.1 can be simplified to

$$\frac{d}{dz}(\dot{m}_L) dz - d\dot{m}_{v,evap} = \frac{\delta}{\delta t}(\rho_L \phi_{v,L} A_c dz) \tag{2.3}$$

Since the liquid density, the cross sectional area, as well as the step size can be assumed constant in the model, the only variable in time that remains is the liquid volume fraction

$\phi_{v,L}$. The liquid volume fraction depends on the gas and liquid mass flow rate, gas and liquid density, and the packing configuration. It can also be assumed constant in time when assuming a constant liquid and gas flow rate. This further simplifies equation 2.3 to

$$\frac{d}{dz}(\dot{m}_L) = \frac{d}{dz}(\dot{m}_{v,evap}) \tag{2.4}$$

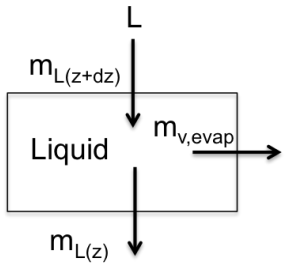

Figure 2.4: liquid mass control volume

2.2.2. Mass Transfer Gas Side

The gas side contains both air and water vapor and is thus an air/vapor mixture. The conservation of mass applied to the gas side is expressed as

$$(\dot{m}_a + \dot{m}_v)_{z+dz} - (\dot{m}_a + \dot{m}_v)_z - d\dot{m}_{v,evap} = \frac{\delta}{\delta t}(m_G) = \frac{\delta}{\delta t}(\rho_G \phi_{v,G} A_c dz) \tag{2.5}$$

Here,

- m_a is the mass flow rate of dry air
- m_v is the mass flow rate of water vapor already in the air
- $\dot{m}_{v,evap}$ is the mass flow rate of the portion of evaporated liquid
- m_G is the mass of the air/vapor mixture
- ρ_G is the air/vapor mixture density
- $\phi_{v,G}$ is the air/vapor mixture volume fraction

The volume fraction of the gas mixture can be expressed as

$$\phi_{v,G} = 1 - \phi_{v,L} - \phi_{v,pack} \tag{2.6}$$

and

$$\frac{(\dot{m}_a + \dot{m}_v)_{z+dz} - (\dot{m}_a + \dot{m}_v)_z}{dz} = \frac{d}{dz}(\dot{m}_a + \dot{m}_v) \tag{2.7}$$

Using equations 2.6 and 2.7, knowing that $\dot{m}_a$ is constant at all heights and knowing that A_c and dz are constant over time, equation 2.5 can be simplified to

$$\frac{d}{dz}(\dot{m}_v) - \frac{d}{dz}\dot{m}_{v,evap} = A_c \frac{\delta}{\delta t}(\rho_G(1 - \phi_{v,L} - \phi_{v,pack})) \tag{2.8}$$

The volume fraction of the packed bed $\phi_{v,pack}$ is constant in the packed bed. As mentioned above, the volume fraction of the liquid $\phi_{v,L}$ is nearly constant for constant liquid and gas flow rates. Therefore, under these circumstances the rate of change of $\phi_{v,G} = 1 - \phi_{v,L} - \phi_{v,pack}$ is negligible and can thus be assumed constant.

The mixture density is expressed as

$$\rho_G = \frac{\dot{m}_a}{\dot{m}_a + \dot{m}_v}\rho_a + \frac{\dot{m}_v}{\dot{m}_a + \dot{m}_v}\rho_v \tag{2.9}$$

where ρ_a and ρ_v denote the air and vapor densities. By also assuming constant air and vapor densities in time (not in height), the time dependence of the mixture density vanishes as well, so that equation 2.8 is further simplified to

$$\frac{d}{dz}(\dot{m}_v) = \frac{d}{dz}(\dot{m}_{v,evap}) \tag{2.10}$$

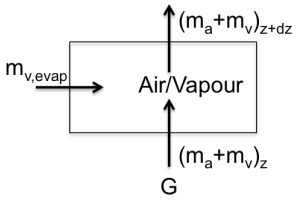

Figure 2.5: air/vapor mass control volume

2.2.3. Mass Transfer Evaporation

Using equation 2.4 and 2.10, it can be seen that during humidification the following holds:

$$\frac{d}{dz}(\dot{m}_{v,evap}) = \frac{d}{dz}(\dot{m}_v) = \frac{d}{dz}(\dot{m}_L) \tag{2.11}$$

Thus, in order to calculate the new liquid and gas mass flow rates, it is necessary to calculate the rate of evaporation at each height $\frac{d}{dz}(\dot{m}_{v,evap})$. In order to do this, a driving force for the evaporation rate needs to be found.

Fick's law of diffusion states that the driving force for diffusion is the concentration gradient. The rate of diffusion can then be calculated by multiplying the concentration gradient with the diffusivity. The diffusivity is defined as the average velocity with which the molecules of A move in a direction with less concentration. For the x-direction, Fick's law can thus be described as

$$J_A = -\mathbb{D}_{AB}\frac{dC_A}{dx} \tag{2.12}$$

The driving force for $\frac{d}{dz}(\dot{m}_{v,evap})$ is related to Fick's law of diffusion. Instead of a concentration gradient, the mass gradient $\frac{dm}{dz} = \left[\rho_{v,b}(T_G) - \rho_{v,sat}(T_i)\right] A_c$ (which is the driving force) is multiplied with the mass transfer coefficient k_G (instead of the diffusivity), i.e.:

$$\dot{m}_{v,evap} = k_G\left[\rho_{v,b}(T_G) - \rho_{v,sat}(T_i)\right] A_c \tag{2.13}$$

The difference in the evaporation rate over the height can be calculated by introducing the specific wetted area of the packed bed a_w (also known as the specific interphase area between the liquid and vapor phase):

$$\frac{d}{dz}(\dot{m}_{v,evap}) = k_G a_w\left[\rho_{v,b}(T_G) - \rho_{v,sat}(T_i)\right] A_c \tag{2.14}$$

The mass transfer coefficient k_G as well as the specific wetted area a_w will be discussed further in chapter 3 on mass and heat transfer correlations.

In equation 2.14, T_i is known as the interfacial temperature. Convective heat is transferred from the gas phase to the liquid phase through the interphase area. It is assumed that the bulk convection from the air/vapor mixture equals that into the water, thus

$$\alpha_L(T_i - T_L) = \alpha_G(T_G - T_i) \tag{2.15}$$

Here α_L and α_G are the respective liquid and gas heat transfer coefficients in W/m^{2}K. Using equation 2.15, one can express the interfacial temperature as

$$T_i = \frac{\alpha_G T_G + \alpha_L T_L}{\alpha_L + \alpha_G} \tag{2.16}$$

Using the perfect gas law

$$\rho = \frac{M}{R}\frac{P}{T} \tag{2.17}$$

where

- ρ is the density in kg/m^3
- M is the molecular weight in kg/kmol
- R is the gas constant in J/kmolK
- P is the pressure in Pa
- T is the temperature in K

and applying it in equation 2.14, the gradient of evaporation is expressed as,

$$\frac{d}{dz}(\dot{m}_{v,evap}) = k_G a_w \frac{M_v}{R}\left[\frac{\phi P_{sat}(T_G)}{T_G} - \frac{P_{sat}(T_i)}{T_i}\right] A_c \tag{2.18}$$

where M_v is the vapor molecular weight and ϕ is the relative humidity, i.e. the ratio of the partial water vapor pressure to the equillibrium vapor pressure at a given temperature:

$$\phi = \frac{P_v(T_G)}{P_{sat}(T_G)} \tag{2.19}$$

Since it is the change in humidity that drives mass transfer, equation 2.18 is rewritten to a form that shows the change in humidity ratio instead of the change in mass flow over the column. The gradient of the humidity ratio of the air/vapor mixture due to evaporative cooling, $\left(\frac{d\omega}{dz}\right)_{ec}$, is related to the mass flow gradient of evaporation as

$$\frac{d}{dz}(\dot{m}_{v,evap}) = G_a A_c \left(\frac{d\omega}{dz}\right)_{ec} \tag{2.20}$$

where $G_a = \dot{m}_a / A_c$ is the dry air mass flux. The humidity ratio ω is defined as the mass of water vapor divided by the mass of dry air holding the water vapor. Based on the ideal gas law, it can also be expressed as a ratio of partial vapor pressures when at a constant volume and temperature:

$$\omega = \frac{m_v}{m_a} = \frac{\frac{M_v V_v P_v(T_G)}{RT_G}}{\frac{M_a V_a P_a(T_G)}{RT_G}} = \frac{M_v}{M_a}\frac{P_v(T_G)}{P_a(T_G)} = 0.622\frac{\phi P_{sat}(T_a)}{P - \phi P_{sat}(T_a)} \tag{2.21}$$

where $M_v/M_a = 18.02/29.97 = 0.622$, ϕ is the relative humidity, and P_{sat} is the saturation pressure at the bulk air temperature T_G. By rewriting equation 2.21 for $P_{sat}(T_G)$ and combining it with equation 2.18 and 2.20, the gradient of the humidity ratio in the evaporative cooling section is expressed as

$$\left(\frac{d\omega}{dz}\right)_{ec} = \frac{k_G a_w}{G_a}\frac{M_v}{R}\left(\frac{\omega}{0.622+\omega}\frac{P}{T_G} - \frac{P_{sat}(T_i)}{T_i}\right) \tag{2.22}$$

Using equation 2.22 and combining it with equations 2.20, 2.4 and 2.10, it is now possible to calculate a new liquid and gas mass flow when humidification takes place. By dividing these mass flows by the crossectional area A_c, the new liquid and gas mass flux (L and G) can be calculated.

Remember that humidification will occur until the relative humidity in the air is unity since afterwards no room for water will be available in the air since it is saturated. The speed of humidification depends on the difference in the density of vapor at the interface area at temperature T_i and the density of the vapor in the air at temperature T_g as shown in equation 2.13.

2.2.4. Heat Transfer Liquid Side

Heat transfer is assumed to take place between the packing, the liquid and the air/vapor mixture. Heat transfer from the condenser column to the surroundings is assumed negligible due to good insulation. The transfer of heat is best described in figure 2.6 below.

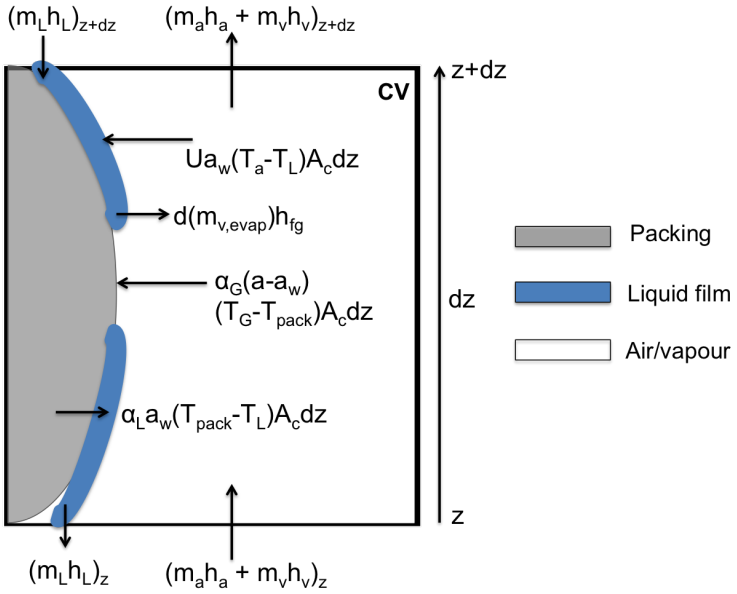

Figure 2.6: Heat transfer between the packing, the liquid and the air/vapor mixture

Applying the conservation of energy to the water side of the control volume first, will yield the following equation:

$$\begin{aligned}(\dot{m}_L h_L)_{z+dz} - (\dot{m}_L h_L)_z - d(\dot{m}_{v,evap}) h_{fg} + U a_w (T_G - T_L) A_c dz \\ + \alpha_L a_w (T_{pack} - T_L) dz = \frac{\delta}{\delta t} (\rho_L \phi_{v,L} h_L A_c dz)\end{aligned} \tag{2.23}$$

where T_{pack} is the temperature of the packed bed, h_L is the specific enthalpy of water and h_{fg} the latent heat of evaporation. Since the liquid density, liquid volume fraction, specific heat capacity, cross sectional column area and step size all remain constant over time, equation 2.23 can be further simplified to:

$$\frac{d}{dz}(\dot{m}_L h_L) - \frac{d}{dz}(\dot{m}_{v,evap}) h_{fg} + U a_w (T_G - T_L) A_c + \alpha_L a_w (T_{pack} - T_L) A_c = \rho_L \phi_{v,L} A_c \frac{\delta}{\delta t}(h_L) \tag{2.24}$$

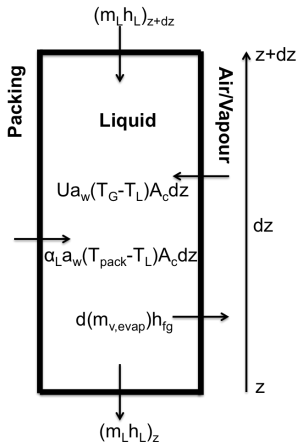

Figure 2.7: liquid enthalpy control volume

Here,

- $\frac{d}{dz}(\dot{m}_L h_L)$ reflects the change in the liquid enthalpy along the z-direction
- $\frac{d}{dz}(\dot{m}_{v,evap}) h_{fg}$ accounts for the heat transport through evaporation
- $U a_w (T_G - T_L) A_c$ accounts for the convective heat transport from the air/vapor mixture to the colder liquid
- $\alpha_L a_w (T_{pack} - T_L) A_c$ accounts for the convective heat transport from the packing to the colder liquid
- $\rho_L \phi_{v,L} A_c \frac{\delta}{\delta t}(h_L)$ accounts for the transient variation of the liquid heat capacity due to temperature changes

Noting that

$$\frac{(\dot{m}_L h_L)_{z+dz} - (\dot{m}_L h_L)_z}{dz} = \frac{d}{dz}(\dot{m}_L h_L) = \dot{m}_L \frac{d}{dz}(h_L) + h_L \frac{d}{dz}(\dot{m}_L) = \dot{m}_L \frac{d}{dz}(h_L) + h_L \frac{d}{dz}(\dot{m}_{v,evap}) \tag{2.25}$$

then equation 2.24 can be written as,

$$\dot{m}_L \frac{d}{dz}(h_L) + (h_L - h_{fg}) \frac{d}{dz}(\dot{m}_{v,evap}) + U a_w A_c (T_G - T_L) + \alpha_L a_w (T_{pack} - T_L) = \rho_L A_c \phi_{v,L} \frac{\delta}{\delta t}(h_L) \tag{2.26}$$

Remembering that

- $\dot{m}_L = L A_c$ where L is the water mass flux
- $\frac{d}{dz} \dot{m}_{v,evap} = G_a A_c \frac{dw}{dz}$

Equation 2.26 can be rewritten as

$$\frac{\delta h_L}{\delta t} = \frac{L}{\rho_L \phi_{v,L}} \frac{dh_L}{dz} + \frac{G_a (h_L - h_{fg})}{\rho_L \phi_{v,L}} \frac{d\omega}{dz} + \frac{U a_w (T_G - T_L)}{\rho_L \phi_{v,L}} + \frac{\alpha_L a_w (T_{pack} - T_L)}{\rho_L \phi_{v,L}} \tag{2.27}$$

Equation 2.27 is a partial differential equation, first order in time and space with h_L being the dependent variable. When solved, 2.27 yields the evolving liquid enthalpy distribution along the height of the evaporator as time proceeds. Since steady state is assumed, equation 2.27 is simplified to

$$\frac{dh_L}{dz} = \frac{G_a}{L}\frac{d\omega}{dz}(h_{fg} - h_L) - \frac{Ua_w}{L}(T_G - T_L) - \frac{\alpha_L a_w}{L}(T_{pack} - T_L) \tag{2.28}$$

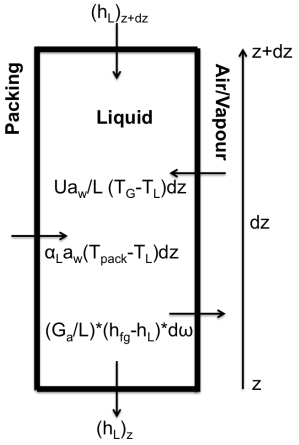

Figure 2.8: liquid specific enthalpy control volume

The liquid enthalpy derivative above is used to calculate the liquid temperature derivative dT_L/dz. This is done by using the new enthalpy value and the atmospheric pressure in the column as inputs in the "Coolprop" database for humid air. From this the new local temperature T_L at height $z+dz$ is obtained which can be used to calculate the liquid temperature derivative dT_L/dz. Assuming the pressure to be constant is justified due to the fact that the temperature is hardly effected by a pressure difference of max 700 Pa in the column.

2.2.5. Heat Transfer Gas Side

The application of the conservation of energy on the air/vapor mixture side yields,

$$(\dot{m}_a h_a + \dot{m}_v h_v)_z - (\dot{m}_a h_a + \dot{m}_v h_v)_{z+dz} + d(\dot{m}_{v,evap})h_{fg} - Ua_w(T_G - T_L)A_c dz - \alpha_G(a - a_w)(T_G - T_{pack})A_c dz = \frac{\delta}{\delta t}(m_a h_a + m_v h_v) \tag{2.29}$$

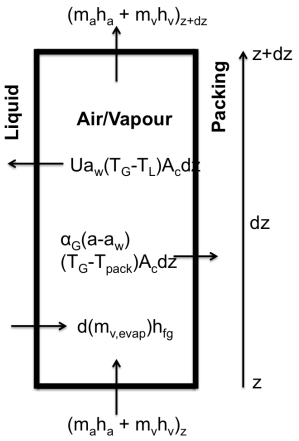

Figure 2.9: air enthalpy control volume

Noting that

$$(\dot{m}_a h_a + \dot{m}_v h_v)_z - (\dot{m}_a h_a + \dot{m}_v h_v)_{z+dz} = -(\dot{m}_a \frac{dh_a}{dz} + h_a \frac{d\dot{m}_a}{dz} + \dot{m}_v \frac{dh_v}{dz} + h_v \frac{d\dot{m}_v}{dz})dz \tag{2.30}$$

where,

- $h_a \frac{d\dot{m}_a}{dz}$ is considered to be 0 as there is no mass transfer of dry air into the water (dry air is considered a non-condensable gas).

- $\frac{d\dot{m}_v}{dz} = \frac{d(\dot{m}_{v,evap})}{dz}$ as shown in equation 2.10

then Equation 2.29 can be written as

$$\begin{aligned} -\dot{m}_a\frac{dh_a}{dz}dz - \dot{m}_v\frac{dh_v}{dz}dz - \frac{d}{dz}(\dot{m}_{v,evap})dz(h_v - h_{fg}) - Ua_w(T_G - T_L)A_c dz \\ -\alpha_G(a-a_w)(T_G - T_{pack})A_c dz = \frac{\delta}{\delta t}(m_a h_a + m_v h_v) \end{aligned} \tag{2.31}$$

The first two terms in equation 2.31 can be rewritten as

$$-\dot{m}_a\frac{dh_a}{dz}dz - \dot{m}_v\frac{dh_v}{dz}dz = -\dot{m}_G\frac{dh_G}{dz}dz = -\dot{m}_a(1+\omega)\frac{dh_G}{dz}dz \tag{2.32}$$

where $\dot{m}_G$ and h_G represent the gas (= air + vapor) mass flow and gas specific enthalpy respectively. Similarly, the last term in equation 2.31 can be rewritten as

$$\frac{\delta}{\delta t}(m_a h_a + m_v h_v) = \frac{\delta}{\delta t}(m_G * h_G) = m_a(1+\omega)\frac{\delta h_G}{\delta t} \tag{2.33}$$

Knowing that at the air/vapor temperature T_G, the latent heat of vaporisation can be expressed as

$$h_{fg}(T_G) = h_v(T_G) - h_L(T_G) \tag{2.34}$$

and using the substitutions from 2.32 and 2.33, equation 2.31 may be rearranged as

$$\begin{aligned} m_a(1+\omega)\frac{\delta h_G}{\delta t} = -\dot{m}_a(1+\omega)\frac{dh_G}{dz}dz - \frac{d}{dz}(\dot{m}_{v,evap})dz(h_L(T_G)) \\ -Ua_w(T_G - T_L)A_c dz - \alpha_G(a-a_w)(T_G - T_{pack})A_c dz \end{aligned} \tag{2.35}$$

The assumption of steady state gives $\frac{\delta h_G}{\delta t} = 0$, and equation 2.35 can be expressed as

$$\begin{aligned} \frac{dh_G}{dz} = \frac{h_L(T_G)}{(1+\omega)}\frac{d\omega}{dz} - \frac{Ua_w(T_G - T_L)}{G_a(1+\omega)} \\ -\frac{\alpha_G(a-a_w)(T_G - T_{pack})}{G_a(1+\omega)} \end{aligned} \tag{2.36}$$

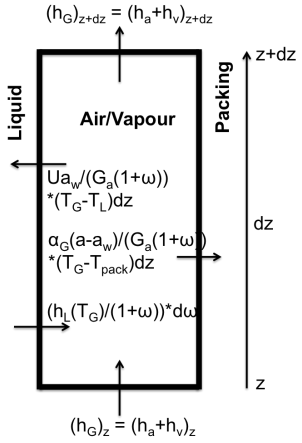

Figure 2.10: air specific enthalpy control volume

The gas enthalpy derivative above is used to calculate the gas temperature derivative dT_G/dz. This is done by using the new enthalpy values, the previously calculated humidity ratio ω, as well as the atmospheric pressure in the column as inputs in the "Coolprop" database for humid air. From this the new local temperature T_G at height $z+dz$ is obtained which can be used to calculate the temperature derivative dT_G/dz. Assuming the pressure to be constant is justified due to the fact that the temperature is hardly effected by a pressure difference of max 700 Pa in the column.

2.2.6. Heat Transfer Packing

Halfway through this thesis it became clear that heat transfer to the packed bed is important. The packing material acts as a medium where mass and heat transfer can occur, and although no mass is transferred to the packing, heat is certainly absorbed in the packing. In fact, the temperature sensors do not display the air temperature as previously thought, but instead display the packing temperature. This can be justified from the fact that the sensors are made up of the same material as the Pall Ring packing (stainless steel) and are also in contact with (and thus transfer heat to/from) both air and water.

The conservation of energy on the packed bed side gives:

$$\frac{\delta}{\delta t}(\rho_{pack}\phi_{v,pack}h_{pack}A_c dz) = \alpha_G(a-a_w)(T_G-T_{pack})A_c dz - \alpha_L a_w(T_{pack}-T_L)A_c dz \quad (2.37)$$

Considering that ρ_{pack}, ϕ_{pack}, A_c and dz are all assumed constant, equation 2.37 simplifies to

$$\rho_{pack}\phi_{v,pack}\frac{\delta h_{pack}}{\delta t} = \alpha_G(a-a_w)(T_G-T_{pack}) - \alpha_L a_w(T_{pack}-T_L) \quad (2.38)$$

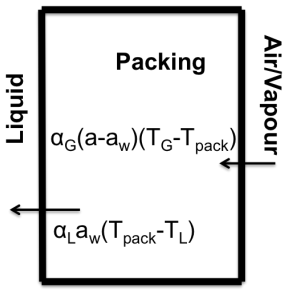

Figure 2.11: packing heat control volume

Since steady state is assumed, T_{pack} can be calculated at any location using equation 2.39 and knowing T_G and T_L at that location.

$$T_{pack} = \frac{\frac{\alpha_G(a-a_w)}{\alpha_L a_w}T_G + T_L}{1+\frac{\alpha_G(a-a_w)}{\alpha_L a_w}} \quad (2.39)$$

Note: It seems unusual to use the definition of enthalpy for a solid (in equations 2.37 and 2.38) since usually internal energy is used to describe heat within a solid. Yet, enthalpy was used to show the relation with previous calculations, and it is also justifiable. Enthalpy is defined as $dH = dE + d(PV) = dE + PdV + VdP$. For a solid, $dV = 0$ for a fixed amount of matter and $dE \gg VdP$, thus $H = E$. Therefore, the specific packing enthalpy h_{pack} is of course equal to the specific internal energy, allowing the use of h_{pack} for a solid.

2.3. Mass and Heat transfer Analysis, Dehumidification

The dehumidification process for OTWP is quite similar to that of the humidification process in cooling towers, with the main difference being that mass flows from the air/vapor mixture to the liquid film [1]. When looking at figure 2.2, the first important observation is that the flow path of water during dehumidification is exactly opposite to the flow path during humidification. This can also be seen in figure 2.12 below:

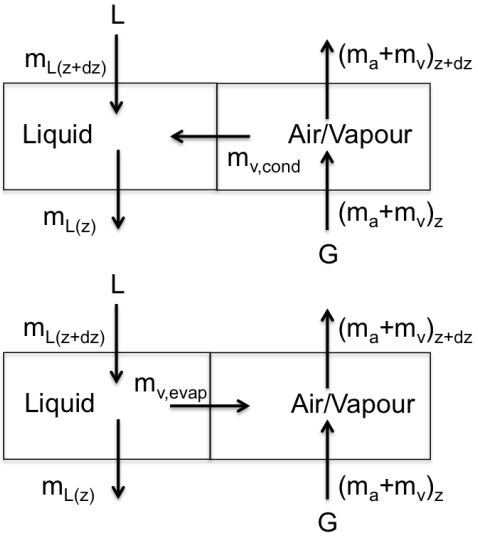

Figure 2.12: difference between control volumes during evaporation (humidification) and condensation (dehumidification)

Thus, initially the same procedure, used for the humidification cycle to obtain equations 2.4 and 2.10, is also used for the dehumidification cycle. The only difference is that the mass transfer reverses during dehumidification and thus the vapor and liquid mass transfer equations become:

$$\frac{d}{dz}(\dot{m}_L) = -\frac{d}{dz}(\dot{m}_{v,cond}) \tag{2.40}$$

$$\frac{d}{dz}(\dot{m}_v) = -\frac{d}{dz}(\dot{m}_{v,cond}) \tag{2.41}$$

2.3.1. Mass Transfer Condensation

A main difference in the dehumidification process is calculating the absolute humidity. The process starts the same though. As explained in equation 2.21, the local humidity ratio, ω, is related to the local air/vapor temperature T_G and relative humidity ϕ as follows:

$$\omega = \frac{m_v}{m_a} = \frac{\frac{M_v V_v P_v(T_G)}{RT_G}}{\frac{M_a V_a P_a(T_G)}{RT_G}} = \frac{M_v}{M_a}\frac{P_v(T_G)}{P_a(T_G)} = 0.622\frac{\phi P_{sat}(T_a)}{P - \phi P_{sat}(T_a)} \tag{2.42}$$

The difference is that the water vapor saturation pressure now corresponds to the local air/vapor temperature, T_G and not a separate equilibrium interface temperature T_i. This is because in order for condensation to occur, the relative humidity in the air has to be unity and obviously the relative humidity in the air is measured using the local air temperature. The following empirical representation of the saturation line from Klausner et al. [26] can be used:

$$P_{sat}(T) = C_a * e^{(C_b T - C_c T^2 + C_d T^3)} \tag{2.43}$$

where the empirical constants are $C_a = 0.611379, C_b = 0.0723669, C_c = 2.78793 \times 10^{-4}, C_d = 6.76138 \times 10^{-7}$, P_{sat} is the saturation pressure in kPa and T is the temperature in °C.

During the condensation process, the humidity ratio as a function of height can be represented as

$$\left(\frac{d\omega}{dz}\right)_{cond} = \frac{d\omega}{dP_{sat}(T_G)} * \frac{dP_{sat}(T_G)}{dT_G} * \frac{dT_G}{dz} \tag{2.44}$$

The first term in equation 2.44 can be obtained using the quotient rule in equation 2.42:

$$\frac{d\omega}{dP_{sat}(T_G)} = \frac{0.622\phi P}{(P-\phi P_{sat})^2} \tag{2.45}$$

The second term can be obtained by differentiating equation 2.43 with T_G:

$$\frac{dP_{sat}(T_G)}{dT_G} = C_a * e^{(C_b T_G - C_c T_G^2 + C_d T_G^3)} * \left(C_b - 2C_c T_G + 3C_d T_G^2\right) = P_{sat}(T_G) * \left(C_b - 2C_c T_G + 3C_d T_G^2\right) \tag{2.46}$$

Equation 2.44 can now be rewritten as

$$\left(\frac{d\omega}{dz}\right)_{cond} = \frac{0.622\phi P}{(P-\phi P_{sat})^2} * P_{sat}(T_G) * \left(C_b - 2C_c T_G + 3C_d T_G^2\right) * \frac{dT_G}{dz} \tag{2.47}$$

Recalling equation 2.42 and assuming the relative humidity ϕ to be unity (100%) throughout the condensation process, then equation 2.47 can be rewritten as

$$\left(\frac{d\omega}{dz}\right)_{cond} = \frac{dT_G}{dz}\left(\frac{P}{P-P_{sat}(T_G)}\right)\omega\left(C_b - 2C_c T_G + 3C_d T_G^2\right) \tag{2.48}$$

It can be seen that the humidity ratio in equation 2.48 is now only a function of air temperature during the condensation process assuming a constant total pressure throughout the system. $\frac{dT_G}{dz}$ is calculated using Coolprop and $\frac{dh_G}{dz}$. $\frac{dh_G}{dz}$ is calculated in equation 2.52 (see next section on heat transfer).

2.3.2. Heat Transfer Liquid and Gas Side

Looking at the heat flow diagram in figure 2.6, the same procedure can be used for the condenser to calculate the heat transfer equations, except that now condensation takes place instead of evaporation (see figure 2.13).

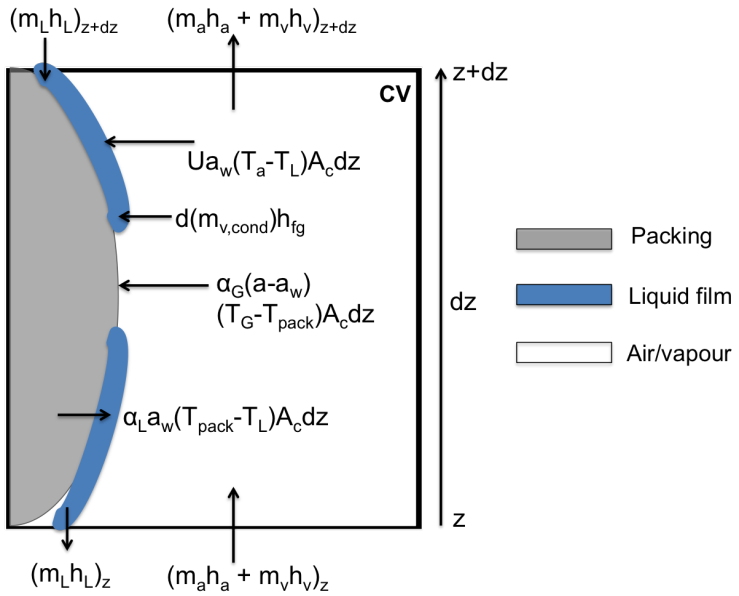

Figure 2.13: Heat transfer between the packing, the liquid and the air/vapor mixture

Applying the conservation of energy to the water side and to the gas side yields:

$$(\dot{m}_L h_L)_{z+dz} - (\dot{m}_L h_L)_z + d(\dot{m}_{v,cond}) h_{fg} + U a_w (T_G - T_L) A_c dz + \alpha_L a_w (T_{pack} - T_L) dz = \frac{\delta}{\delta t} (\rho_L \phi_{v,L} h_L A_c dz) \tag{2.49}$$

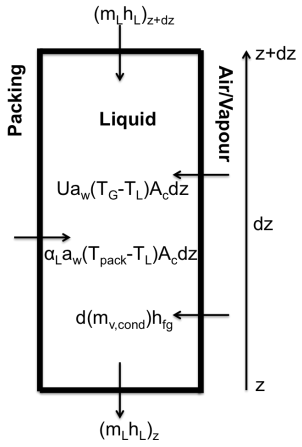

Figure 2.14: total liquid enthalpy control volume

$$(\dot{m}_a h_a + \dot{m}_v h_v)_z - (\dot{m}_a h_a + \dot{m}_v h_v)_{z+dz} - d(\dot{m}_{v,cond}) h_{fg} - U a_w (T_G - T_L) A_c dz - \alpha_G (a - a_w)(T_G - T_{pack}) A_c dz = \frac{\delta}{\delta t} (m_a h_a + m_v h_v) \tag{2.50}$$

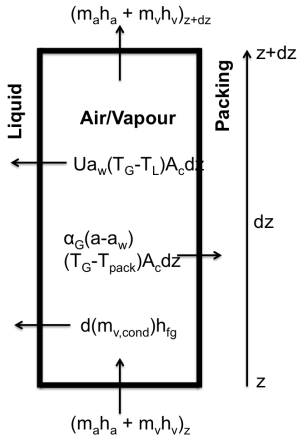

Figure 2.15: total air enthalpy control volume

Applying the same procedures as in subsections 2.2.4 and 2.2.5, the energy equations during condensation at steady state reduce to:

$$\frac{dh_L}{dz} = -\frac{G_a}{L}\frac{d\omega}{dz}(h_{fg} - h_L) - \frac{Ua_w}{L}(T_G - T_L) - \frac{\alpha_L a_w}{L}(T_{pack} - T_L) \tag{2.51}$$

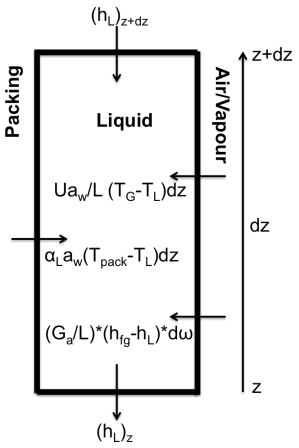

Figure 2.16: total liquid specific enthalpy control volume

$$\frac{dh_G}{dz} = -\frac{h_L(T_G)}{(1+\omega)}\frac{d\omega}{dz} - \frac{Ua_w(T_G - T_L)}{G_a(1+\omega)} - \frac{\alpha_G(a - a_w)(T_G - T_{pack})}{G_a(1+\omega)} \tag{2.52}$$

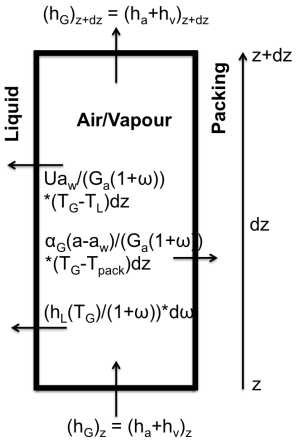

Figure 2.17: total air specific enthalpy control volume

From equation 2.51 and 2.52, the respective liquid and gas enthalpy derivatives are used to obtain the liquid and gas temperature derivatives (dT_G/dz and dT_L/dz). This is done by using the new enthalpy values, the previously calculated humidity ratio ω, as well as the atmospheric pressure in the column as inputs in the "Coolprop" database for humid air. From this the new local temperature T_G and T_L at height $z+dz$ are obtained which can be used to calculate the temperature derivatives. Once again, the pressure can be assumed constant since the temperature is hardly effected by a pressure difference of max 700 Pa in the column.

3

Mass and Heat Transfer Correlations

Identifying correct heat and mass transfer coefficients is often difficult and equations for both cannot always be solved. Depending on the process, it is sometimes easier to find heat transfer coefficients and harder to find mass transfer coefficients, and sometimes it is the other way around. In the case for a condensation column on atmospheric water extraction, the mass transfer process is studied more easily and accurately than the heat transfer process, since mass transfer can be measured in the column.

It would thus be best if mass and heat transfer were linked, such that if one is known, the other is known as well. Fortunately, as described by Eckert & Goldstein in their book on analogies to heat transfer processes [15], this is the case. The heat and mass transfer analogy states that, for any fixed geometry and for similar boundary conditions, an equation describing heat transfer can be found when the Sherwood number Sh is replaced by the Nusselt number Nu, and the Schmidt number Sc is replaced by the Prandtl number Pr [15]. For instance, if a mass transfer correlation is known in the form

$$Sh = f(Re, Sc) \tag{3.1}$$

then the same correlation for heat transfer is found in the form

$$Nu = f(Re, Pr) \tag{3.2}$$

3.1. Proof of heat and mass transfer analogy

Heat and mass transfer processes are governed by partial differential equations for mass and energy (or temperature). For laminar boundary layer flow, the non dimensional heat and mass transfer relationship is given as:

$$\frac{Nu}{Sh} = (\frac{Pr}{Sc})^{1/3} \tag{3.3}$$

This equation can be derived from the conventional governing equations for heat and mass transfer, which both derive from the general convective-diffusion equation:

$$\frac{\partial c}{\partial t} = \nabla \cdot (\mathbb{D} \nabla c) - \nabla \cdot (\vec{v}\, c) + S_c \tag{3.4}$$

$$\frac{\partial T}{\partial t} = \nabla \cdot (\kappa \nabla T) - \nabla \cdot (\vec{v}\, T) + S_T \tag{3.5}$$

Here,

- c is defined as the mass concentration and is the variable of interest for the mass transfer equation. The term $\frac{\partial c}{\partial t}$ describes the change in c over time at a certain position. The temperature T is the variable of interest for the heat transfer equation.
- $\mathbb{D}$ is the mass diffusivity needed for mass transfer. $\nabla \cdot (\mathbb{D}\nabla c)$ is known as the diffusive term. For heat transfer the thermal diffusivity is needed, which is given as κ.
- $\overrightarrow{v}$ is the velocity field that variable c is moving with. $\nabla \cdot (\overrightarrow{v}\, c)$ is known as the advective (or convective) term.
- S_c describes the sources or sinks of the variable c, i.e. if any c is created or destroyed. For heat transfer S_T is used to describe heat sources or sinks.

For a steady-state, two-dimensional, laminar, incompressible boundary layer flow, the expressions above reduce to:

$$u\frac{\partial c}{\partial x} + v\frac{\partial c}{\partial y} = \mathbb{D}\frac{\partial^2 c}{\partial y^2} \tag{3.6}$$

$$u\frac{\partial T}{\partial x} + v\frac{\partial T}{\partial y} = \kappa\frac{\partial^2 T}{\partial y^2} \tag{3.7}$$

These 2 equations provide four unknowns, namely u, v, c and T. The boundary layer conditions for the continuity equation and the momentum equation are thus introduced to provide a solution:

$$\frac{\partial u}{\partial x} + \frac{\partial v}{\partial y} = 0 \tag{3.8}$$

$$u\frac{\partial u}{\partial x} + v\frac{\partial u}{\partial y} = \nu\frac{\partial^2 u}{\partial y^2} \tag{3.9}$$

There are now 4 equations and 4 unknowns. When non-dimensionalizing equations 3.7 and 3.6, the thermal diffusivity κ and the mass diffusion coefficient $\mathbb{D}$ are replaced by their respective dimensionless transport properties: the Prandtl number, $Pr = \frac{\nu}{\kappa}$, and the Schmidt number, $Sc = \frac{\nu}{\mathbb{D}}$.

Solution methods for these non dimensional equations are discussed in Eckert & Goldstein [15] and Kays et al. [25]. From the solution, one finds that the Nusselt number distribution for a laminar boundary layer as a function of streamwise position is well approximated as:

$$Nu_x = 0.332 Re_x^{1/2} Pr^{1/3} \tag{3.10}$$

Similarly, for the mass transfer equation, the Sherwood number distribution yields:

$$Sh_x = 0.332 Re_x^{1/2} Sc^{1/3} \tag{3.11}$$

Equation 3.3 can now be obtained by dividing equation 3.10 by equation 3.11, assuming the same Reynolds number at location x.

The conventional analogy factor for turbulent boundary layers is different than for laminar boundary layers (equation 3.3). Turbulent boundary layers are given by the conventional heat/mass transfer analogy [15]:

$$\frac{Nu}{Sh} = \frac{Pr}{Sc} \cdot \frac{1 + 1.48 Re_x^{-1/10} Sc^{-1/6} \cdot (Sc - 1)}{1 + 1.48 Re_x^{-1/10} Pr^{-1/6} \cdot (Pr - 1)} \tag{3.12}$$

Any flow region in between fully laminar and fully turbulent is known as the transition region. This region is known to be quite complicated but by using experimental data, analogy factors can be found. For instance, by comparing two identical experiments, one measuring heat transfer and the other measuring mass transfer, it is possible to determine new analogies in the transition region. Below, the analogy factor used to calculate the heat transfer in the OTWP column using the measured mass transfer is explained.

3.2. Heat Transfer Correlations

Different analogies have been found using the similarity condition between equation 3.1 and 3.2 such as Reynolds analogy and Prandtl–Taylor analogy. In this report, the Chilton and Colburn analogy between heat and mass transfer is used for the gas side because it has proved to be the most accurate among other analogies [42] [19]. The analogy is based on correlations of experimental data rather than on assumptions about transport mechanisms. Using Chilton and Colburn, the heat transfer coefficient on the gas side is related to the gas side mass transfer coefficient as follows,

$$\frac{Nu_G}{Pr_G^{1/3}} = \frac{Sh_G}{Sc_G^{1/3}} \tag{3.13}$$

Here,

- Nusselt number = $Nu = \frac{\alpha l}{\lambda} = \frac{\text{convective heat transfer}}{\text{conductive heat transfer}}$
- Prandtl number = $Pr = \frac{Cp\mu}{\lambda} = \frac{\text{momentum diffusivity}}{\text{thermal diffusivity}}$
- Sherwood number = $Sh = \frac{kl}{\mathbb{D}} = \frac{\text{convective mass transfer}}{\text{molecular diffusion}}$
- Schmidt number = $Sc = \frac{\mu}{\rho\mathbb{D}} = \frac{\text{momentum diffusivity}}{\text{mass diffusivity}}$

Rewriting equation 3.13 using the definitions of the non-dimensional numbers gives:

$$\frac{\alpha_G L}{\lambda_G} * \left(\frac{\lambda_G}{Cp_G \mu_G}\right)^{1/3} = \frac{k_G L}{\mathbb{D}_G} * \left(\frac{\rho_G \mathbb{D}_G}{\mu_G}\right)^{1/3} \tag{3.14}$$

Rearranging for the heat transfer coefficient α_G gives

$$\alpha_G = k_G \left(\rho_G Cp_G\right)^{1/3} \left(\frac{\lambda_G}{\mathbb{D}_G}\right)^{2/3} \tag{3.15}$$

For the liquid side, Klausner et al. [27] decided to use the same analogy above but with a different exponent. The heat transfer coefficient on the liquid side has been related to the mass transfer coefficient on the liquid side as follows,

$$\frac{Nu_L}{Pr_L^{1/2}} = \frac{Sh_L}{Sc_L^{1/2}} \tag{3.16}$$

and thus the equation for α_L becomes

$$\alpha_L = k_L \left(\rho_L Cp_L\right)^{1/2} \left(\frac{\lambda_L}{\mathbb{D}_L}\right)^{1/2} \tag{3.17}$$

Here,

- λ_L and λ_G denote the thermal conductivity of the liquid and gas
- $\mathbb{D}_L$ and $\mathbb{D}_G$ denote the molecular diffusion coefficients of the liquid and gas
- k_L and k_G denote the mass transfer coefficients of the liquid and gas side.

The reason for the different exponent above is described by Holman in chapter 6 of his book on heat transfer [24]. Holman uses the Dittus and Boelter equation to show that when cooling a fluid, a lower exponent is needed for the Prandtl number than when heating a fluid. In this case, since the liquid is heated and the gas is cooled, Klausner et al. likewise use a lower exponent (1/3) for the gas Prandtl number than for the liquid Prandtl number (1/2) in the Chilton and Colburn analogy. Different data show that experimental values for the exponents vary between 0.3 and 0.5 [27] [24] [42]. The value of the exponent for the gas side is not as important, since the Prandtl number for air is approximately 1. For water the Prandtl number is approximately 7, and from the OTWP experimental data shown in the next section, a value of 1/2 for the exponent indeed has the best fit for the OTWP system.

Using the equations above, the total heat transfer coefficient U is calculated as:

$$\frac{1}{U} = \frac{1}{\alpha_L} + \frac{1}{\alpha_G} \tag{3.18}$$

3.3. Mass Transfer Correlations

The heat and mass transfer analogy in equation 3.16 is only useful if the mass transfer correlations are known. As described earlier in section 2.2.3, mass transfer correlations are needed to be able to calculate the mass transfer rate. The calculation of the mass transfer rate is similar to Fick's law of diffusion and is described as (also see equations 2.12-2.14):

$$\dot{m}_{V,evap} = k_G a_w \left[\rho_{V,b}(T_G) - \rho_{V,sat}(T_i)\right] A_c dz \tag{3.19}$$

The mass transfer correlations all consist of an equation for the mass transfer coefficient k_G and for the specific wetted area a_w. These correlations will depend on [20]:

- the type of packing selected, random or structured
- Packing generation, first, second, third or fourth generation packing
- which phase controls mass transfer, gas or liquid side

Three different correlations for the mass transfer coefficients k_L and k_G will be described below. The first is the Onda et al. correlation [38] which is the correlation originally used by Klausner et al. [27]. The second and third, respectively the Billet & Schultes correlation [8] and the Mackowiak correlation [33], are improvements of the original correlation by Onda et al. . Which correlation is most suitable for the present application has yet to be validated for the OTWP system using the experimental setup.

3.3.1. Klausner/Onda correlations

The mass transfer coefficients associated with film flow in packed beds have been widely investigated. The most widely used correlation is that proposed by Onda et al. [38]. Onda et al.'s correlation [38] is used to calculate the mass transfer coefficients in the packed bed tower described by Klausner et al. [27].

Onda et al.'s correlation for the wetted surface area is:

$$a_w = a\left(1 - \exp\left[-1.45\left(\frac{\sigma_{pack}}{\sigma_L}\right)^{3/4} Re_{La}^{0.1} Fr_{La}^{-0.05} We_{La}^{1/5}\right]\right) \tag{3.20}$$

Experimental results show that when using Raschig Rings, the wetted area is correct within a margin of error of +/- 20% [38]. Klausner et al. found that Onda et al.'s correlation underpredicted the wetted specific area of the packing material. Therefore, a correction was made by Klausner et. al [27] as follows,

$$a_w = a\left(1 - \exp\left[-2.2\left(\frac{\sigma_{pack}}{\sigma_L}\right)^{3/4} Re_{La}^{1/2} Fr_{La}^{-0.05} We_{La}^{1/5}\right]\right) \tag{3.21}$$

The following, widely tested empirical correlation for mass transfer coefficients k_G and k_L (in m/s) have been derived by Onda et al.:

$$k_G = 5.23 Re_{Ga}^{0.7} Sc_G^{1/3} (aD_{pack})^{-2} a\mathbb{D}_G \tag{3.22}$$

$$k_L = 0.0051 Re_{Lw}^{2/3} Sc_L^{-0.5} (aD_{pack})^{0.4} \left(\frac{\mu_L g}{\rho_L}\right)^{1/3} \tag{3.23}$$

In the above equations, the non-dimensional numbers are defined as:

- $Re_{La} = \frac{\rho_L u_L}{a\mu_L}$, the Reynolds number for the liquid side based on the specific area of the packing (ratio of inertial forces to viscous forces, useful to predict the transition from laminar flow to turbulent flow)
- $Re_{Lw} = \frac{\rho_L u_L}{a_W \mu_L}$, the Reynolds number for the liquid side based on the specific wetted area of the packing (ratio of inertial forces to viscous forces, useful to predict the transition from laminar flow to turbulent flow)
- $Re_{Ga} = \frac{\rho_G u_G}{a\mu_G}$, the Reynolds number for the gas side based on the specific area of the packing (ratio of inertial forces to viscous forces, useful to predict the transition from laminar flow to turbulent flow)
- $Sc_L = \frac{\mu_L}{\rho_L D_L}$, the Schmidt number for the liquid side (ratio of momentum diffusivity over mass diffusivity)
- $Sc_G = \frac{\mu_G}{\rho_G D_G}$, the Schmidt number for the gas side (ratio of momentum diffusivity over mass diffusivity)
- $Fr_{La} = \frac{L^2 a}{\rho_L^2 g}$, the Froude number for the liquid side (ratio of the flow inertia to gravity)
- $We_L = \frac{L^2}{\rho_L \sigma_L a}$, the Weber number for the liquid side (measures the relative importance of the fluid's inertia compared to its surface tension, which is useful for analyzing thin film flows and the formation of droplets)

The liquid side has a margin of error of 20% while the gas side has a margin of error of 30%. If Pall Rings smaller than 15 mm are used, the constant 5.23 in equation 3.22 is to be replaced with 2. For the OTWP facility, Pall Rings of 16 mm are used. This is quite near the minimum value of 15 mm, thus the model will be tested with values between 2 and 5.23 to obtain the best result.

3.3.2. Billet & Schultes Correlation

About 20 years after Onda et al., following many experiments, Billet & Schultes identified characteristic data and constants for an extensive list of packings. Tables with these characteristics and constants are presented in appendix D. Like Onda et al., the correlations proposed by Billet & Schultes are only useful for packing types which have been analyzed, the relations may not be used for a packing type that has not been analyzed.

The specific wetted packing area is given by the empirical formula:

$$a_w = 1.5 * (a * D_h)^{-0.5} * \left(\frac{u_l * D_h}{\nu_l}\right)^{-0.2} * \left(\frac{u_l^2 * \rho_l * D_h}{\sigma_l}\right)^{0.75} * \left(\frac{u_l^2}{g * D_h}\right)^{-0.45} * a \tag{3.24}$$

Using equation 3.24, the experimentally determined formulas for the volumetric mass transfer coefficients $k_L \cdot a_w$, and $k_G \cdot a_w$ are described as [9]:

$$k_L \cdot a_w = C_L 12^{1/6} \bar{u}_L^{1/2} \left(\frac{\mathbb{D}_L}{D_h}\right)^{1/2} a\left(\frac{a_w}{a}\right) \tag{3.25}$$

$$k_G \cdot a_w = C_G \left(\frac{1}{(\epsilon - LH)^{1/2}}\right)\left(\frac{a^{3/2}}{D_h^{1/2}}\right)\mathbb{D}_G \left(\frac{u_G}{a \cdot \nu_G}\right)^{3/4} \left(\frac{\nu_G}{\mathbb{D}_G}\right)^{1/3} \left(\frac{a_w}{a}\right) \tag{3.26}$$

The unknown variables in equations 3.25 and 3.26 are examined more closely below.

1. C_L and C_G are packing specific constants that can be found in appendix D

2. $\mathbb{D}_L$ is the diffusion coefficient in the liquid phase (diffusion of water into water) while $\mathbb{D}_G$ is the diffusion coefficient in the gas phase (diffusion of water into air). The self-diffusion coefficient for water in water is 2.3*10^{-9} m^2/s [44] [13] at 25 °C and the diffusion coefficient of water into air is equal to 2.82*10^{-5} at 25 °C [13]. The temperature dependence of the diffusion coefficient in liquids can be found using the Stoke's Einstein equation, which predicts that:

$$\frac{\mathbb{D}_{L,T_1}}{\mathbb{D}_{L,T_2}} = \frac{T_1 * \mu_{L,T_2}}{T_2 * \mu_{L,T_1}} \tag{3.27}$$

where T is in K and μ is the dynamic viscosity of the liquid. The temperature dependence of the diffusion coefficient in the gas phase can be expressed using Chapman-Enskog theory. Evaluating at temperatures within working range of the OTWP setup, i.e. between 12 °C and 28 °C, it was found that the diffusion coefficients vary very little. Both are thus assumed constant in this work.

3. D_h is the hydraulic diameter of packed beds. It is defined as 4 times de void fraction ϵ divided by the specific packing surface area a, i.e.

$$D_h = \frac{4\epsilon}{a} \tag{3.28}$$

5. According to Billet & Schultes [4], in order to be able to calculate the liquid hold-up LH, the hydraulic packing area a_h is needed. It is given by

$$a_h = C_h Re_{La}^{0.15} Fr_{La}^{0.1} a, \quad Re_{La} < 5 \tag{3.29}$$

and,

$$a_h = C_h 0.85 Re_{La}^{0.25} Fr_{La}^{0.1} a, \quad Re_{La} \geq 5 \tag{3.30}$$

Values of a and C_h are characteristics of the particular type and size of packing, as listed in appendix D together with the packing void fraction ϵ and other packing constants, derived by Billet & Schultes [7] [8] [9].

Using equation 3.29/3.30 (depending on the liquid Reynolds number), the liquid holdup can be calculated. The specific liquid holdup LH in a packed column is obtained experimentally and expressed as

$$LH = \left(12 \frac{Fr_{La}}{Re_{La}}\right)^{1/3} \left(\frac{a_w}{a}\right)^{2/3} \tag{3.31}$$

3.3.3. Mackowiak's correlation

Onda et al.'s correlations, as well as Billet & Schultes correlations, are based on the assumption of liquid film formation in packed beds, and thus only describe mass transfer between air and the liquid film flow. Mackowiak's correlations also take into account the effect on mass transfer due to droplets formed between packing elements. In short, the Mackowiak method [33] assumes that

1. Like Onda et al. and Billet & Schultes, mass transfer area is provided due to liquid rivulets flowing down along the surface of individual packing elements
2. Mass transfer area is also provided between individual packing elements mainly in the form of liquid droplets.

According to the model, mass transfer is interrupted during the formation of rivulets and only recommences when new droplets are formed. This is best described using Higbie's model [22]. Higbie claims that the liquid mass transfer coefficient can be described using the following equation:

$$k_L = \frac{2}{\sqrt{\pi}} \sqrt{\frac{\mathbb{D}_L}{\tau}} \tag{3.32}$$

Furthermore, for disperse (i.e. well-spread) liquid systems, the wetted specific packing area can be calculated using the fundamental equation [32]:

$$a_w = 6 \frac{LH}{D_D} \tag{3.33}$$

Thus the volumetric liquid mass transfer coefficient can be described as:

$$k_L a_w = \frac{2}{\sqrt{\pi}} \sqrt{\frac{\mathbb{D}_L}{\tau}} * 6 \frac{LH}{D_D} \tag{3.34}$$

If the variables in equation 3.34 are known, then $k_L a_w$ can be calculated. How to calculate τ, LH and D_D will be described below.

1. τ is the contact time, i.e. the time a droplet takes to fall between packing elements, and is described as

$$\tau = \frac{l_D}{\bar{u}_L} \tag{3.35}$$

Here, $\bar{u}_L$ is equal to $\frac{u_L}{LH}$ which is the superficial liquid velocity divided by the liquid hold-up (described in 3.38 and 3.39). The mean contact path l_D in equation 3.35 can be calculated using the empirical formula

$$l_D = 0.115(1-\phi_{pack})^{2/3} D_h^{1/2} \tag{3.36}$$

The form factor ϕ_{pack} is a geometrical parameter of the individual packing. The numerical value of the form factor represents the proportion of the perforated surface area of a packing element, and has a value of 0.28 for a 16 mm Pall Ring packing.

2. The liquid hold-up in equation 3.34 is defined as the total volume of liquid in the packing V_L divided by the total packing volume V_{pack}. The total volume of liquid is further subdivided into V_{static} which accounts for the liquid retained in pores and void spaces as well as $V_{dynamic}$ which accounts for the liquid flow in the column, thus:

$$V_L = V_{static} + V_{dynamic} \rightarrow LH = \frac{V_L}{V_{pack}} = LH_{static} + LH_{dynamic} \tag{3.37}$$

By evaluating large amounts of experimental data for different packings, empirical formulas for the liquid hold-up LH have been found throughout the entire operating range, combining both the static and dynamic liquid volume behavior. Mackowiak [32] concluded that turbulent liquid flow can be expected in packed columns at $Re_{La} \geq 2$, whilst laminar liquid flow is expected at $Re_{La} \leq 2$. According to Mackowiak [32], the liquid hold-up in random packings for

- turbulent liquid flow $Re_{La} \geq 2$ below the loading point $F_G \leq 0.65 F_{G,fl}$ is described by

$$LH = 0.57 \cdot Fr_{La}^{1/3} = 0.57 \left(\frac{a \cdot u_L^2}{g} \right)^{1/3} \tag{3.38}$$

- laminar liquid flow $Re_{La} < 2$ below the loading point $F_G \leq 0.65 F_{G,fl}$ is described by

$$LH = \frac{3}{4} \cdot \left(\frac{3}{g} \right)^{1/3} a^{2/3} (u_L \cdot \nu_L)^{1/3} \tag{3.39}$$

Of 1000 experimental data items in the database for randomly filled packing elements with $d = 0.015 - 0.090$ m and different type Y structured packings with a = 100-500 m^2/m^3, the relative error of the above equations stays within ±20% [32].

One may have noticed that no LH is given for flows above the loading point $F_G > 0.65 F_{G,fl}$. Even though these equations do exist, they are not needed for this model since operating above the loading point would be economically inefficient. The definition of the loading point is when the gas velocity is high enough to restrict the flow of a liquid, it thus marks the start of the entrainment regime in columns. After this point, the pressure drops at a much faster rate until the flooding point. Thus operating at conditions above the loading point results in an increase in energy needed per m^3 water produced, which is economically unfavorable.

3. The final variable in equation 3.34 is the droplet diameter according to Sauter D_D. When liquid flows through the packing, deformed droplets with a Sauter diameter are formed below the loading line in accordance with the correlation

$$D_D = C_D \sqrt{\frac{\sigma_L}{(\rho_L - \rho_G) \cdot g}} \tag{3.40}$$

where constant $C_D = 1$ for mass transfer from water to air according to Mackowiak [32], and $C_D = 1.25$ for mass transfer from air to water since this last case leads to an increase in droplet size. The validity of this equation for falling droplets has been confirmed by numerous experimental results for liquid-liquid systems [5] [6] [35] and gas-liquid systems [11] [12].

Substitution of equations 3.35, 3.38/3.39 (depending on the Reynolds number) and 3.40 into equation 3.34 leads to the prediction of the volumetric mass transfer coefficient $k_L * a_w$ in columns with random packings.
For turbulent liquid flow ($Re_{La} \geq 2$):

$$k_L \cdot a_w = \frac{15.1}{(1-\phi_{pack})^{1/3} D_h^{1/4}} \cdot \left(\frac{\mathbb{D}_L \cdot (\rho_L - \rho_G) \cdot g}{\sigma_L} \right)^{1/2} \cdot \left(\frac{a}{g} \right)^{1/6} \cdot u_L^{5/6} \tag{3.41}$$

For laminar liquid flow ($Re_{La} < 2$):

$$k_L \cdot a_w = \frac{17.3 \cdot a^{1/3}}{(1-\phi_{pack})^{1/3} D_h^{1/4}} \cdot \left(\frac{\mathbb{D}_L \cdot (\rho_L - \rho_G) \cdot g}{\sigma_L} \right)^{1/2} \cdot \left(\frac{3 \cdot \nu_L}{g} \right)^{1/6} \cdot u_L^{2/3} \tag{3.42}$$

The equations for the liquid side volumetric mass transfer coefficient have been tested using modern and classical packing types with diameter sizes between $D_{pack} = 0.012 - 0.090$m. The mean error of ± 12.5% [33] [34] means that the Mackowiak method should provide the highest accuracy when testing the OTWP system. Also, the formula above shows that it is possible to calculate the volumetric mass transfer coefficient $k_L \cdot a_w$ for packings of any type and size without the evaluation of specific empirical packing constants derived from experiments [33].

Gas side mass transfer is based on the assumption, that mass transfer is taking place from the continuous gas or vapor phase into the individual droplets falling down in the packed bed. The Frossling equation [18] describes mass transfer between a gas and a moving droplet within the gas. The formula is quite consistent with experiments and takes the form

$$Sh_{G,D_{LH\to 0}} = 2 + C_V Re_D^{n_1} Sc_G^{1/3} \tag{3.43}$$

The definition of the dimensionless numbers on the right side of the equation can be found in the nomenclature. The left side of the equation can also be described by

$$Sh_{G,D_{LH\to 0}} = \frac{k_{G,D_{LH\to 0}} D_D}{\mathbb{D}_G} \tag{3.44}$$

Rewriting equations 3.43 and 3.44 for $k_{G,D_{LH\to 0}}$, the mass transfer coefficient for a single droplet becomes:

$$k_{G,D_{LH\to 0}} = (2 + C_V Re_D^{n_1} Sc_G^{1/3}) \frac{\mathbb{D}_G}{D_D} \tag{3.45}$$

For a falling swarm of droplets in random packings, the liquid hold-up LH will be larger than 0, and the mass transfer intensity will decrease compared to a single droplet flow. This gives a new mass transfer coefficient described as:

$$k_{G_{LH>0}} = k_{G,D_{LH\to 0}} \left(1 - \frac{LH}{\varepsilon}\right)^{n_2} \tag{3.46}$$

Solving for $k_{G_{LH>0}}$ by rewriting 3.45 into equation 3.46 and multiplying with equation 3.33, the volumetric mass transfer coefficient in the vapor phase $k_G \cdot a_w$ is then estimated by

$$k_G \cdot a_w = k_{G_{LH>0}} \cdot a_w = \frac{\mathbb{D}_G}{D_D} \left(2 + C_V Re_D^{n_1} Sc_G^{1/3}\right) \left(1 - \frac{LH}{\varepsilon}\right)^{n_2} 6\frac{LH}{D_D} \tag{3.47}$$

Remember that specific wetted packing area a_w is still described using equation 3.33. The constants C_V and exponents n_1 and n_2 in equation 3.47 are evaluated from experimental data. Using the constants provided from experiments by Mackowiak [34], equation 3.47 is rewritten as

$$k_G \cdot a_w = k_{G_{LH>0}} \cdot a_w = \frac{\mathbb{D}_G}{D_D} \left(2 + 0.0285 \frac{u_R D_D}{\nu_G} \left(\frac{\nu_G}{\mathbb{D}_G}\right)^{1/3}\right) \left(1 - \frac{LH}{\varepsilon}\right)^{6} 6\frac{LH}{D_D} \tag{3.48}$$

According to Mackiowiak's model, the number of available correlations describing the gas-side controlled mass transfer is fewer compared to the liquid-side controlled mass transfer. Yet, the accuracy of different correlations for gas-side controlled mass transfer is larger than for liquid-side controlled mass transfer [20]. The correlation with the best fit for the OTWP system will be discussed in chapter 5 on validation.

3.4. Pressure Drop

The mass and heat transfer correlations above are important for predicting the water production rate of the OTWP process, as will be further discussed in chapter 5. Another important variable needed for predicting economic feasibility of OTWP is the energy rate needed to obtain this water production rate. By dividing the energy rate by the water production rate, the total energy consumption per m^3 of water produced [kWh/m^3] can be calculated. The energy rate is directly related to the pressure drop, as can be seen in equation 3.49.

$$\dot{W} = \frac{\dot{V} dp}{\eta} \tag{3.49}$$

The pressure drop calculations are given below. Klausner et al., whom used Onda et al.'s correlations to predict mass transfer, do not provide a pressure drop model and the pressure drop was measured experimentally instead [1]. Therefore, only the Mackowiak and Billet & Schultes pressure drop models will be discussed below.

3.4.1. Mackowiak Pressure Drop

For most models, determining the pressure drop of irrigated random and structured packings can only be calculated if the law of resistance for single-phase flow through the packing is known. Mackowiak however developed a method based on the law of resistance $\psi_{G,L} = f(Re_{La})$ for gas/liquid two-phase flow [31]. This model is built up from the fundamental Darcy Weisbach equation (used in the well-known channel model) and is valid

for the whole loading range up to the flooding point.

The Darcy-Weisbach equation states that when a gas flows through a packed column of height Z, it undergoes a pressure drop Δp_0:

$$\frac{\Delta p_0}{Z} = \lambda_{df} \frac{\bar{u}_G^2 \rho_G}{2 D_{h,p}} \tag{3.50}$$

Here,

- the effective gas velocity = $\bar{u}_G = u_G/\epsilon$, represents the gas velocity divided by the fraction of the channel volume that is occupied by the gas phase, i.e. the void fraction
- the hydraulic diameter is defined a bit differently, namely as a function of the effective particle diameter of a packing D_p: $D_{h,p} = \frac{2}{3}\frac{\epsilon}{1-\epsilon} D_p K$. It also takes into account the influence of the column wall by multiplying with a wall factor K (see below for definitions D_p and K). The hydraulic diameter in general is a term which allows us to represent a flow in non-circular tubes. In this case a non-circular channel flow of water around the packing.
- the gas loading factor = $F_G = \bar{u}_G \rho_G^{1/2}$, a factor representing the amount of gas in the column.
- the drag coefficient = $\psi = \frac{3}{4}\lambda_{df}$, defined as 3/4 of the Darcy friction factor λ_{df} which depends on the flow regime.

Using the definitions above, equation 3.50 can be rewritten as:

$$\frac{\Delta p_0}{Z} = \psi \frac{1-\epsilon}{\epsilon^3} \frac{F_G^2}{D_p K} \tag{3.51}$$

where

- $D_p = 6(1-\epsilon)/a$ is the particle diameter of the different packing elements, and depends on the specific surface area a and the void fraction ϵ.
- $K = (1 + \frac{2}{3}\frac{1}{1-\epsilon}\frac{D_p}{D_S})^{-1}$ is the wall factor, here D_S is the column diameter

If liquid is sprayed onto the packing then films and droplets form on the packing which reduce the free-space cavities in the packed bed. The effective void fraction for two-phase flow of the packed bed ϵ_e will equal $\epsilon - LH$ instead of just ϵ, where LH is the liquid hold-up.

D_p, a, and $\frac{\Delta p_0}{Z}$ are all functions of the effective void fraction ϵ_e and will thus change accordingly. The effective specific area a_e can be described as:

$$a_e = a \cdot f(\epsilon, LH) \tag{3.52}$$

where the function $f(\epsilon, LH) = 1$ if the liquid hold-up $LH = 0$. The new particle diameter as a function of the effective specific area is given by:

$$D_{p,e} = 6(1 - (\epsilon - LH)/a_e \tag{3.53}$$

The pressure drop over the height is given by:

$$\frac{\Delta p_0}{Z} = \psi_G \frac{1-(\epsilon - LH)}{(\epsilon - LH)^3} \frac{F_G^2}{D_{p,e} K} \tag{3.54}$$

Substituting the equations 3.52 and 3.53 into equation 3.54 gives:

$$\frac{\Delta p_0}{Z} = \frac{1}{6} \psi_G f(\epsilon, LH) \frac{a}{(\epsilon - LH)^3} \frac{F_G^2}{K} \tag{3.55}$$

Using the definition of the particle diameter D_p to substitute for a gives:

$$\frac{\Delta p_0}{Z} = \psi_G f(\epsilon, LH) \frac{1-\epsilon}{(\epsilon - LH)^3} \frac{F_G^2}{D_p K} \tag{3.56}$$

The drag coefficient for the gas phase under two-phase flow conditions ψ_G is a function of the pseudo-drag coefficient defined as:

$$\psi_{G,L} = \frac{1}{1 + LH/(1-\epsilon)} \psi_G f(\epsilon, LH) \tag{3.57}$$

Substituting for the pseudo-drag coefficient gives the final representation of the pressure drop over the height:

$$\frac{\Delta p_0}{Z} = \psi_{G,L} (1 + \frac{LH}{1-\epsilon}) \frac{1-\epsilon}{(\epsilon - LH)^3} \frac{F_G^2}{D_p K} \tag{3.58}$$

The pseudo-drag coefficient can also be defined differently than equation 3.57, namely as a function of the Reynolds number and the shape of a packing element:

$$\psi_{G,L} = A \mu Re_{La}^B \tag{3.59}$$

Here, μ represents the shape factor of the packing and A and B are constants. According to Mackowiak [31], for $Re_{La} \leq 12.3$: $\psi_{G,L} = 5.4 \mu Re_{La}^{-0.14}$ and that for $Re_{La} > 12.3$: $\psi_{G,L} = 3.8\mu$.

Thus for $Re_{La} \leq 12.3$:

$$\frac{\Delta p_0}{Z} = 5.4 \mu Re_{La}^{-0.14} (1 + \frac{LH}{1-\epsilon}) \frac{1-\epsilon}{(\epsilon - LH)^3} \frac{F_G^2}{D_p K} \tag{3.60}$$

and for $Re_{La} > 12.3$:

$$\frac{\Delta p_0}{Z} = 3.8 \mu (1 + \frac{LH}{1-\epsilon}) \frac{1-\epsilon}{(\epsilon - LH)^3} \frac{F_G^2}{D_p K} \tag{3.61}$$

3.4.2. Billet & Schultes Pressure Drop

Like Mackowiak, Billet & Schultes start their pressure drop equations using the Darcy-Weisbach equation. Using the same theory explained in section 3.4.1, the pressure drop over the height for the two phase flow region can be described as:

$$\frac{\Delta p_0}{Z} = 3\psi_{G,L}\frac{1-\epsilon}{(\epsilon - LH)^3}\frac{F_G^2}{D_p K} \tag{3.62}$$

where $3\psi_{G,L} = \psi_G f(\epsilon, LH)$ if compared to equation 3.56. The drag coefficient $\psi_{G,L}$ according to Billet & Schultes [4] is defined as:

$$\psi_{G,L} = C_{pack,0}\left(\frac{64}{Re_{Gp}} + \frac{1.8}{Re_{Gp}^{0.08}}\right)\left(\frac{\epsilon - LH^{1.5}}{\epsilon}\right)\left(\frac{LH}{LH_S}\right)\exp\left(\frac{13300}{a^{3/2}}\sqrt{Fr_{La}}\right) \tag{3.63}$$

where Re_{Gp} is the Reynold's number of the gas stream dependent on the particle diameter and $C_{pack,0}$ is the packing specific constant which has been determined experimentally for different packings by Billet & Schultes [4]. The Froude number in equation 3.63 replaced the Reynolds number in previous publications of Billet & Schultes due to experiments with high pressure drops. Since the pressure drop is relatively low in the OTWP column, it could be interesting to switch back to the Reynolds number when validating the model.

3.4.3. Flooding Factor

The flooding factor is an important techno-economic parameter and is defined as the gas load factor divided by the gas load factor at flooding point.

$$F_{fl} = \frac{F_G}{F_{G,fl}} \tag{3.64}$$

The gas load factor can be calculated using:

$$F_G = \frac{u_G}{\epsilon}\rho_G^{1/2} \tag{3.65}$$

The gas load factor at flooding point is calculated by:

$$F_G = \frac{u_{G,fl}}{\epsilon}\rho_G^{1/2} \tag{3.66}$$

From the above, one can see that the flooding factor may also be defined as

$$F_{fl} = \frac{u_G}{u_{G,fl}} \tag{3.67}$$

As explained earlier in section 3.3.3, a flooding factor value above the loading point ($F_g \geq 0.65$) marks the start of entrainment regimes which are known to be economically inefficient due to an exponential increase in pressure drop. From an economical standpoint, it is thus important to know when an experiment operates above the loading point and this requires the formula for the gas flooding velocity $u_{G,fl}$. The calculation for the flooding velocity is explained below for both Billet & Schultes and Mackowiak.

Mackowiak calculation of $u_{G,fl}$

According to Mackowiak, the gas flooding velocity is defined as

$$u_{G,fl} = C_{fl,0}\cos(\alpha)\epsilon^{6/5}\psi_{fl}^{-1/6}\sqrt{D_D(\rho_L-\rho_G)\frac{g}{\rho_G}}\frac{D_h}{D_D}(1-LH_{fl})^{7/2}(\frac{\rho_G}{1.165})^{0.18} \tag{3.68}$$

where $C_{fl,0}$ is a constant dependent on the flow channels in the column and is equal to 0.566 for the experiment. ψ_{fl} and LH_{fl} both depend on the Reynolds number.

For $Re_{Gw} < 2100$:

$$\psi_{fl} = C_1 Re_{Gw}^{C_2} \tag{3.69}$$

For $Re_{Gw} > 2100$:

$$\psi_{fl} = C_3 Re_{Gw}^{C_4} \tag{3.70}$$

here the packing constant C_1 = 10, C_2 = -0.18, C_3 = 3.23 and C_4 = -0.0343 (see appendix E).

For $Re_{La} < 2$:

$$LH_{fl} = \frac{\sqrt{1.254FR_{fl}^2 + 0.48FR_{fl}(1-FR_{fl})} - 1.12FR_{fl}}{0.24(1-FR_{fl})} \tag{3.71}$$

For $Re_{La} > 2$:

$$LH_{fl} = \frac{\sqrt{1.44FR_{fl}^2 + 0.8FR_{fl}(1-FR_{fl})} - 1.2FR_{fl}}{0.4(1-FR_{fl})} \tag{3.72}$$

Here, FR_{fl} is equal to the flow ratio at the flooding point, defined as $\frac{\dot{V}_L}{\dot{V}_{G,fl}}$, which is equal to $\frac{u_L}{u_{G,fl}}$ if the cross sectional area in the column is constant.

The two unknowns $u_{G,fl}$ and LH_{fl} can be solved using the two equations 3.68 and 3.71/3.72 above in a solver. For this model, pythons solver "fsolve" was used.

Billet & Schultes calculation of $u_{G,fl}$

According to Billet & Schultes, $u_{G,fl}$ is defined as

$$u_{G,fl} = LH_{fl}^3(3LH_{fl}-\epsilon)\frac{g}{6}\frac{1}{a^2\epsilon}\frac{\rho_L}{\mu_L} * \frac{G}{L}\frac{\rho_L}{\rho_G} \tag{3.73}$$

However, $u_{G,fl}$ can also be defined as

$$u_{G,fl} = \sqrt{2}\sqrt{\frac{g}{\psi_{fl}}}\frac{(\epsilon-LH_{fl})^{3/2}}{\epsilon^{1/2}} * \sqrt{\frac{LH_{fl}}{a}}\sqrt{\frac{\rho_L}{\rho_G}} \tag{3.74}$$

Here,

$$\psi_{fl} = \frac{g}{C_{fl}^2}\left(\frac{L}{G}\sqrt{\frac{\rho_G}{\rho_L}}\frac{\mu_L}{\mu_G}^{0.2}\right)^{-2n_{fl}} \tag{3.75}$$

where,
for $\frac{L}{G}\sqrt{\frac{\rho_G}{\rho_L}} \leq 0.4$: n_{fl} = -0.194 and $C_{fl} = C_{fl,table}$ in appendix D

for $\frac{L}{G}\sqrt{\frac{\rho_G}{\rho_L}} \geq 0.4$: n_{fl} = -0.708 and $C_{fl} = 0.6244 C_{fl,table}\left(\frac{\mu_L}{\mu_G}\right)^{0.1028}$

The two unknowns $u_{G,fl}$ and LH_{fl} can be solved using the two equations 3.73 and 3.74 above in a solver. For this model, pythons solver "fsolve" was used.

Relationship flooding factor and efficiency

Lopez [30] and Kreuk et al. [28] argued that maximum efficiency is obtained at the loading point, i.e. at a flooding capacity value of 0.65-0.7. Yet, this study arrives at a different conclusion. It is important to note that literature does not provide any information on what the flooding capacity should be for an optimum energy consumption to water production ratio.

The gas loading point is a defined point at which the pressure drop will start to deviate from a linear line and increase exponentially if the gas flow is increased. Figure 3.1 shows seperation efficiency graphs for different Mellapak packings. It can be seen that the HETP value stays the same at gas flow rates below the loading point, meaning that the gas flow rate/pressure drop ratio stays the same, and that the highest gas flow rate at the lowest pressure drop can be obtained just below the loading point.

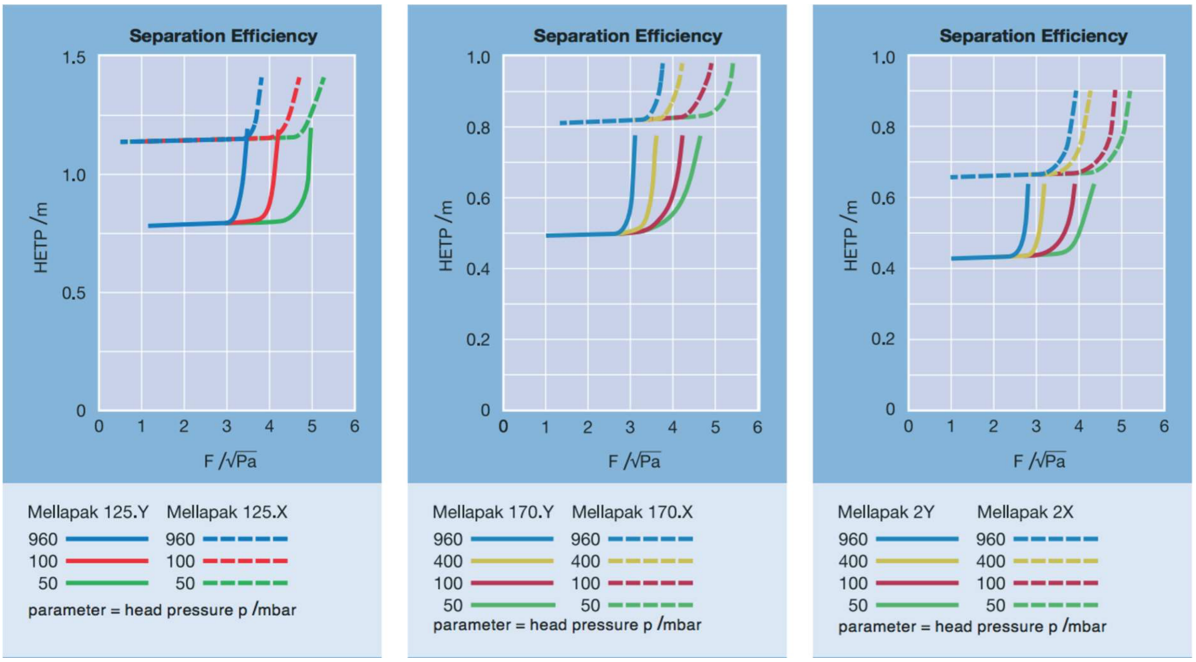

Figure 3.1: Seperation efficiency for 3 different Mellapak packings

Thus, if the measure of efficiency is defined as “where the gas flow rate is highest and where the pressure drop is lowest”, then the optimum point lies just below the loading point. Yet for OTWP, the efficiency is defined as “where the water production is highest and where the pressure drop is lowest”. Even though one might assume the highest water production when the gas flow rate is highest, this is not always the case since heat + mass transfer can worsen at high gas flow rates when other defined variables stay the same (such as water flow, packing height, packing diameter, etc). It is thus possible that the optimum operat-

ing point is far below the loading point value, which is important to keep in mind when optimizing for a pilot plant design.

4

Packed Bed Column Model

4.1. Introduction

This chapter explains how the 6 different submodules in the packed bed column model, shown in figure 4.2, work. Each section starts with an introduction explaining what the importance of that particular module is, how it can be used, as well as the theory used to build it. The flow chart in figure 4.2 already shows the interaction between the different submodules and a basic overview of the experimental setup is also given in figure 4.1 to provide a clearer picture of how the model is built and which part of the model represents which component in the setup. An explanation on how the experimental setup works is provided thoroughly in appendix A.

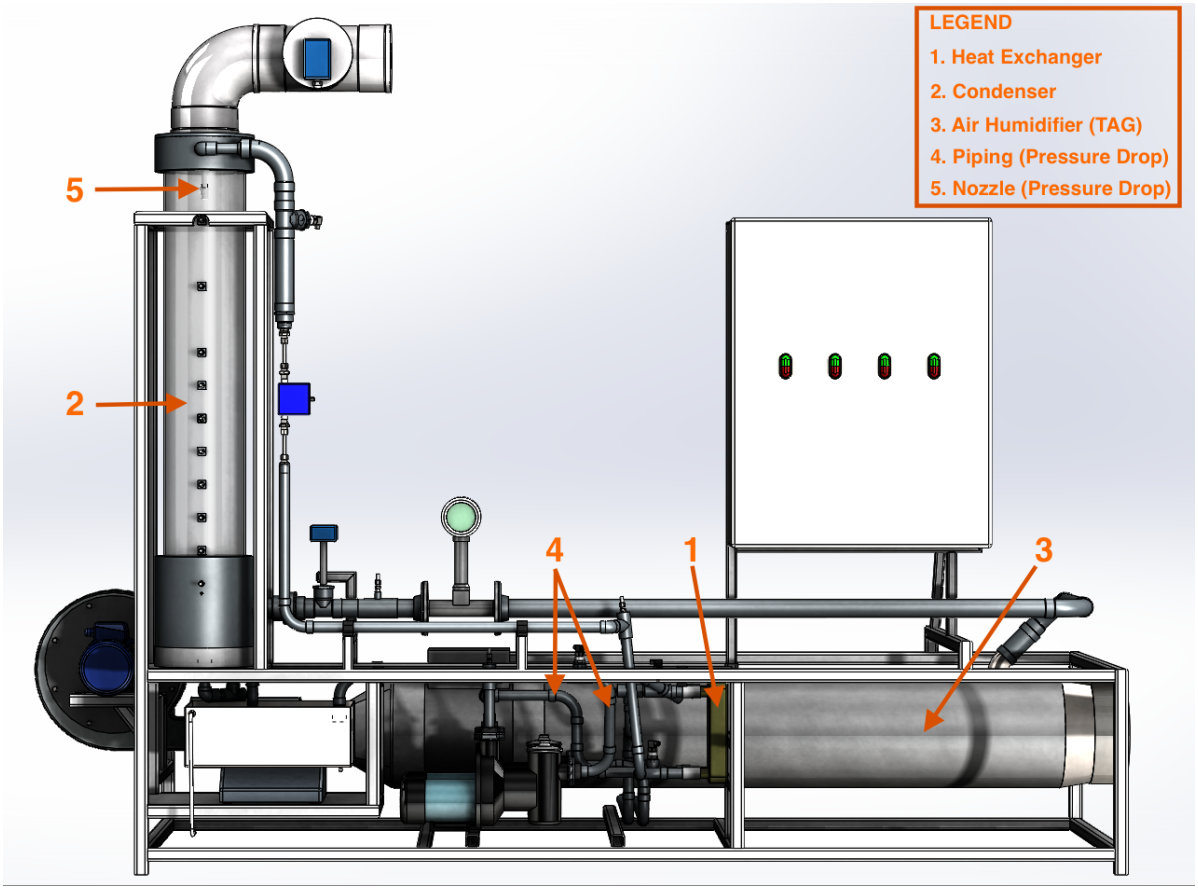

Figure 4.1: Solidworks representation of the OTWP experimental setup

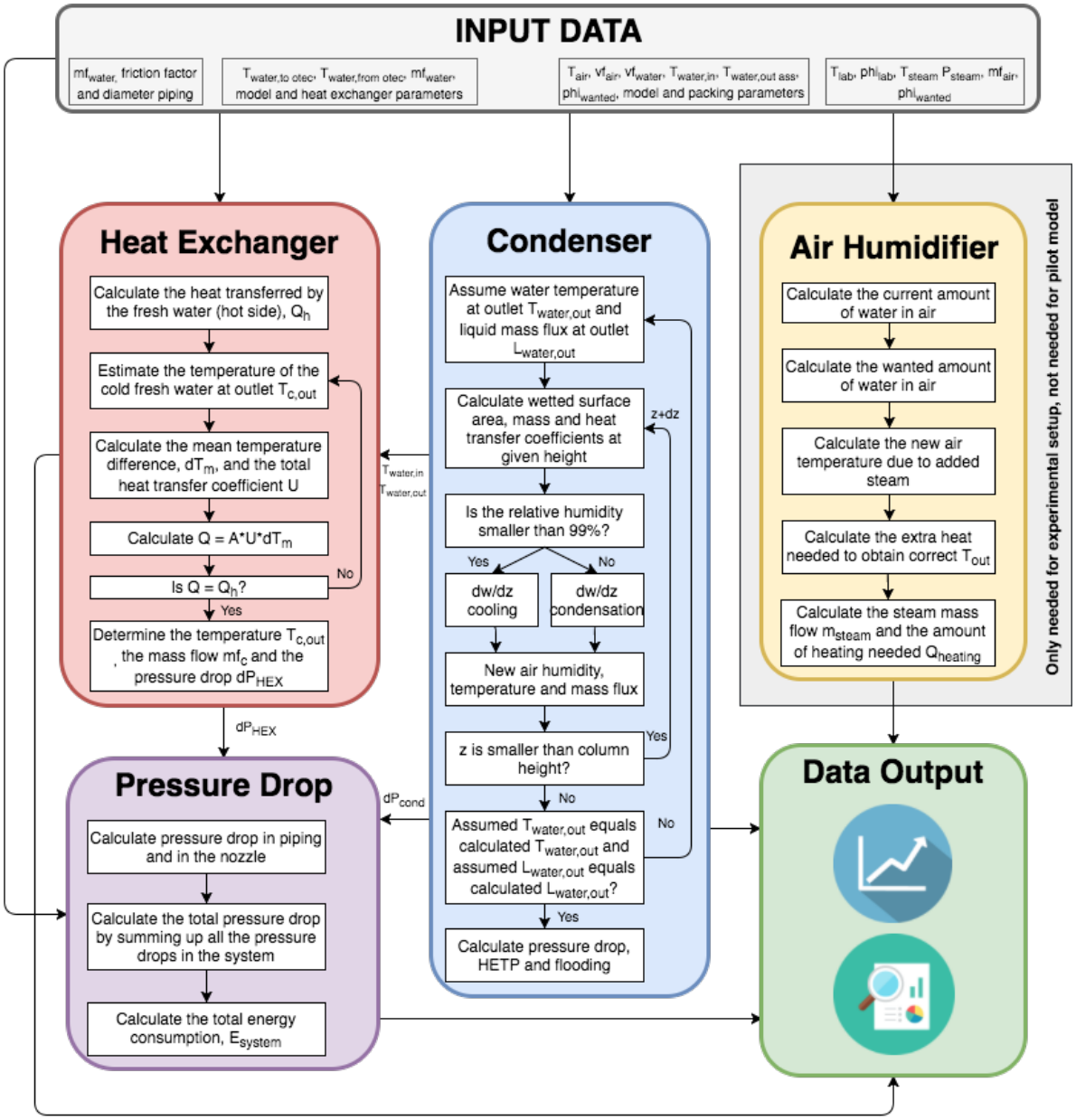

Figure 4.2: Schematic representation of the packed bed column model

4.2. Condenser

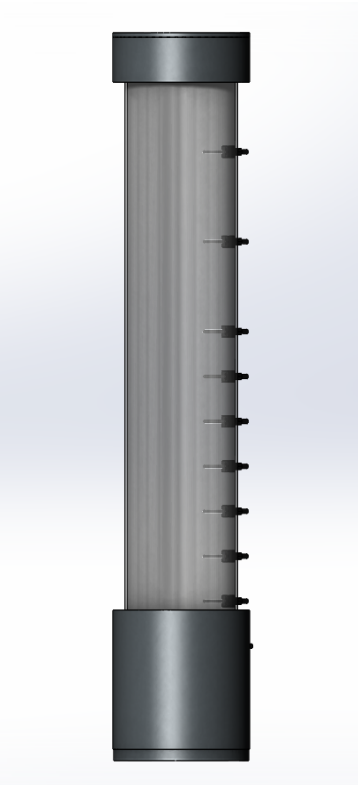

Figure 4.3: Representation of condenser column

Figure 4.4: 16 mm Pall rings random packing distributed in the condenser column

The condenser model is the most important part of the system. It calculates the temperature distribution in the column, the pressure drop within the column as well as the fresh water production rate. From these variables the condensation effectiveness can be calculated as well as the power consumption needed to keep the system running.

The theory behind the condenser model has been thoroughly explained in chapters 2 and 3. Chapter 2 explains the basic theory needed to calculate mass and heat transfer through the condenser column while chapter 3 explains 3 different correlations that can be used to solve for mass and heat transfer.

As mentioned in the beginning of section 2.1, the condenser model uses a loop to calculate the correct mass flux and temperature values through the column. This section explains how the loop works using the temperature and mass flux gradients calculated in chapter 2.

4.2.1. Mass Flux Loop

The fresh water production flux, i.e. the amount of kg water/m^{2}s extracted from the air to the fresh water, is defined in the model as

$$L_{fw,prod} = G_a * \int_z^{z+dz} \frac{d\omega}{dz} dz \tag{4.1}$$

where $\frac{d\omega}{dz}$ is the change in humidity ratio over the height of the column. Using equation 4.1, the new gas and liquid mass flux are defined as

$$G_{(z+dz)} = G_{(z)} + L_{fw,prod} \tag{4.2}$$

$$L_{(z+dz)} = L_{(z)} + L_{fw,prod} \tag{4.3}$$

Note: remember that G in the two equations above differ from G_a (equation 4.1). G_a is the mass flux of dry air and G is the mass flux of humid air.

$G_{(z+dz)}$ and $L_{(z+dz)}$ represent a step dz higher in the column with regard to $G_{(z)}$ and $L_{(z)}$. The gas enters the column at $z = 0$ and leaves the column at $z = 1$. If fresh water is extracted from the gas, then there should be less vapor water in the gas at the top than at the bottom. Thus, the fresh water production flux $L_{fw,prod}$ is a negative number in the model when producing water, since $G_{(z)}$ holds more water than $G_{(z+dz)}$ in equation 4.2.

The liquid enters the column at $z = 1$ and leaves the column at $z = 0$. If there is water production in the column, then there should be more fresh water at the bottom then fresh water entering at the top. Thus the fresh water production flux $L_{fw,prod}$ is also a negative number since $L_{(z)}$ holds more water than $L_{(z+dz)}$ in equation 4.3.

As mentioned in the beginning of section 2.1, if the calculated liquid inlet mass flux $L_{(z=1)}$ does not match the known inlet mass flux L_{in}, then the initial assumption for $L_{(z=0)}$ is increased or decreased by a defined step size. The loop continues until the calculated mass flux matches the known mass flux within a previously defined margin of error.

4.2.2. Temperature Loop

The new gas and liquid temperature are defined as:

$$T_{G(z+dz)} = T_{G(z)} + (\frac{dT_G}{dz}) * dz \tag{4.4}$$

$$T_{L(z+dz)} = T_{L(z)} + (\frac{dT_L}{dz}) * dz \tag{4.5}$$

where, just like the mass flux loop, $T_{G(z+dz)}$ and $T_{L(z+dz)}$ represent a step dz higher in the column with regard to $T_{G(z)}$ and $T_{L(z)}$.

The gas enters the column at $z = 0$ and leaves the column at $z = 1$. The gas is warmer than the liquid and should therefore be cooler once the top of the column is reached. Thus, $(\frac{dT_G}{dz}) * dz$ is a negative number since $T_{G(z)}$ in equation 4.4 is higher than $T_{G(z+dz)}$.

The liquid enters the column at $z = 1$ and leaves the column at $z = 0$. The liquid is cooler than the gas and is therefore coolest at the top and warmest at the bottom. Thus, the temperature gradient $(\frac{dT_L}{dz}) * dz$ is negative, since $T_{L(z)}$ is warmer than $T_{L(z+dz)}$ in equation 4.5.

As mentioned in the beginning of section 2.1, if the calculated liquid inlet temperature $T_{(z=1)}$ does not match the known inlet temperature T_{in}, then the initial assumption for $T_{(z=0)}$ is increased or decreased by a defined step size. The loop continues until the calculated temperature matches the known temperature within a previously defined margin of error.

4.3. Humidifier

One of the problems in the OTWP experimental system is providing the experiment with tropical air at 28°C and at different humidity levels of 65%, 80% and 90%.

The humidifier model solves this problem by calculating the correct steam mass flow to obtain the wanted humidity ratio at a given air mass flow and a given wanted tropical air temperature. It also calculates the amount of extra heating needed to obtain the wanted tropical air temperature (usually 28°C). This is needed because using steam as the only input to heat the inlet air of 20°C in the lab will lead to a too high relative humidity (saturation).

As mentioned in the flow chart above, the humidifier model is not needed for a pilot plant facility, since tropical air conditions would already be met. It is therefore not connected to the other submodules and it can be seen as a separate submodule (see figure 4.2).

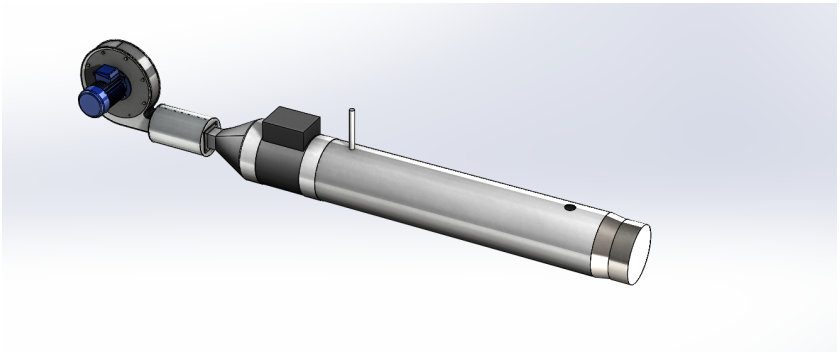

Figure 4.5: Solidworks representation of humidifier in the experimental setup

4.3.1. Explanation of Humidifier Model

In the model, the known/wanted specific enthalpy and humidity ratio values are found first using Coolprop:

- Using the measured air temperature $T_{G,in}$, pressure $P_{G,in}$ and relative humidity value $\phi_{G,in}$ of ambient air inside the lab, Coolprop can find the specific enthalpy $h_{G,in}$ and humidity ratio $\omega_{G,in}$ of the inlet air at this state.

- Using the known pressure $P_{steam,in}$ and the temperature $T_{steam,in}$ of the superheated steam provided in the lab, Coolprop can find the specific enthalpy $h_{steam,in}$ of the inlet steam at this state.

- Using the wanted temperature $T_{G,W}$, pressure $p_{G,W}$ and relative humidity $\phi_{G,W}$ values inside the TAG, Coolprop can find the wanted specific enthalpy $h_{G,W}$ and humidity ratio $\omega_{G,W}$ of air at this state.

The humidity mass balance is used to calculate the amount of steam wanted ($\dot{m}_{steam,W}$) to arrive at the correct humidity ratio inside the TAG:

$$\dot{m}_{steam,W} = \dot{m}_a * (\omega_{G,W} - \omega_{G,in}) \tag{4.6}$$

The energy balance is used to calculate the total heating energy input needed to arrive at 28°C:

$$Q_{heat,W} = Q_{G,steam} + Q_{heat,ext} \tag{4.7}$$

The left hand side of the equation above can be calculated using the wanted enthalpy value $h_{G,W}$:

$$Q_{heat,W} = (\dot{m}_G + \dot{m}_{steam,W}) * h_{G,W} \tag{4.8}$$

The amount of heat in the TAG after adding steam, $Q_{G,steam}$, is calculated in a similar way using the previously found values h_{steam} and $h_{G,in}$:

$$Q_{G,steam} = \dot{m}_{steam,W} * h_{steam,in} + \dot{m}_G * h_{G,in} \tag{4.9}$$

The extra heating energy input needed by an external heater is now easily calculated by rearranging equation 4.7 to:

$$Q_{heat,ext} = Q_{heat,W} - Q_{G,steam} \tag{4.10}$$

The model works in such a way that after the external heat is added (see equation 4.10) and the required steam is added (see equation 4.6), the air temperature in the TAG will be 28°C at the correct relative humidity value.

4.4. Heat Exchanger

The heat exchanger model is a logarithmic mean temperature difference (LMTD) model for an existing plate heat exchanger. The experimental setup uses a brazed type heat exchanger shown in figures 4.6 and 4.7 below. It is important to note that the model is not used to design a heat exchanger (the dimensions of the heat exchanger are used as inputs for the model). Instead, the model is used to calculate the outgoing temperature and mass flow for the cold fluid (i.e. the OTEC sea water). This allows the model to calculate how much OTEC sea water is needed to cool the fresh water outflow to 12 °C. The model also calculates the pressure drop on both the hot and the cold side. It further assumes that both the cold sea water and the hot fresh water are single phase.

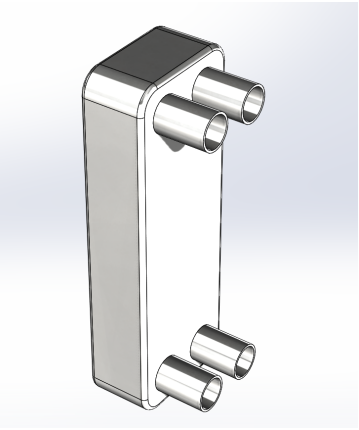

Figure 4.6: Solidworks representation of heat exchanger in the experimental setup

Figure 4.7: Redenko Cetetherm 410 Heat Exchanger in the experimental setup

4.4.1. LMTD Working Principle

Heat transfer across a surface can generally be described as:

$$Q = UA_{HE}\Delta T_{lm} \tag{4.11}$$

where

- Q is the heat transferred per unit time [W]
- U is the overall heat-transfer coefficient [W/m^{2}K]
- A_{HE} is the area for heat exchange [m^2]
- ΔT_{lm} is the logarithmic mean temperature difference [K], which is the driving force for single phase heat transfer

However, the total heat transfer Q can also be identified by calculating the heat transferred away from the hot side:

$$Q = \dot{m}_h * Cp_h * (T_{h,in} - T_{h,out}) \tag{4.12}$$

Or by calculating the heat transferred to the cold side:

$$Q = \dot{m}_c * Cp_c * (T_{c,out} - T_{c,in}) \tag{4.13}$$

Here, $\dot{m}$ and Cp are the mass flow rate and specific heat respectively. The subscripts c and h stand for cold-side and hot-side liquid streams.

In the model, $\dot{m}_c$ and $T_{c,out}$ in equation 4.13 are unknowns. An initial value for $T_{c,out}$, i.e. the salt water stream going back to OTEC, is therefore estimated. Using equation 4.13, $\dot{m}_c$ can be calculated and using equation 4.11, Q can be calculated (since ΔT_{lm} depends on $T_{c,out}$, see below). If Q in equation 4.11 does not match the Q in equation 4.12, then a new estimate is given for $T_{c,out}$. The model will iterate until the heat transfer equals the Q calculated in equation 4.12.

The calculation of each variable in equation 4.11 above is further explained below.

The Overall Heat Transfer Coefficient U

The overall heat transfer coefficient is the reciprocal of the overall resistance to heat transfer, which is the sum of several individual resistances. For heat exchange across a typical plate heat exchanger the relationship between the overall coefficient and the individual coefficients is given by

$$\frac{1}{U} = \frac{1}{\alpha_{fw}} + \frac{1}{\alpha_{fw,d}} + \frac{\delta}{\lambda_{pl}} + \frac{1}{\alpha_{sw}} + \frac{1}{\alpha_{sw,d}} \tag{4.14}$$

where

- α_{fw} = fresh water fluid film heat-transfer coefficient, W / m^{2}K
- $\alpha_{fw,d}$ = fresh water dirt coefficient (fouling factor), W / m^{2}K
- δ = plate thickness, m
- λ_{pl} = thermal conductivity of the plate material, W / mK
- α_{sw} = seawater fluid film heat-transfer coefficient, W / m^{2}K
- $\alpha_{sw,d}$ = seawater dirt coefficient (fouling factor), W / m^{2}K

The convective heat transfer coefficients in equation 4.14 can be described as:

$$\alpha_i = \frac{Nu_i \lambda_i}{D_h} \tag{4.15}$$

where D_h is the hydraulic diameter of the plate (estimated as two times the plate distance), λ_i is the thermal conductivity of the fluid (calculated using Coolprop) and Nu_i is the Nusselt number which is described as,

$$Nu_i = zRe_i^w Pr_i^{0.33} \tag{4.16}$$

equation 4.16 is a general equation that can be used for heat transfer design [43]. The constants z and w are found using a linear regression analysis, a method previously used by Goudriaan [21]. Using experimental data, one can try to fit the curve between the convective heat transfer coefficient α_i (Nu_i is a variable of α_i) and the mass flow $\dot{m}_i$. Different mass flows are taken for the fresh water cycle and the corresponding experimental temperature data (see figure 4.8) is used to fit the curve and find values for z and w in equation 4.16.

Description	Sensor	Units	1	2	3	4	5
Flow OTEC side	FT-21	[kg/s]	**0.105**	**0.104**	**0.104**	**0.103**	**0.102**
Flow OWTP Condensor in	FT-22	[kg/s]	**0.05**	**0.075**	**0.1**	**0.125**	**0.15**
OTEC before HE	TT-12	[C]	**11.298**	**11.305**	**11.302**	**11.307**	**11.279**
Condensor water in	TT-13	[C]	**11.674**	**11.944**	**12.233**	**12.455**	**12.651**
Tank water out	TT-15	[C]	**14.776**	**14.243**	**14.244**	**14.173**	**14.181**
OTEC after HE	TT-16	[C]	**12.824**	**13.025**	**13.289**	**13.456**	**13.601**

Figure 4.8: Experimental data used for linear regression analysis to find constants z and w

The best fit is made when the constant z is equal to 0.125 and w is defined as 0.712. Rewriting for equation 4.16 gives:

$$Nu_i = 0.125 Re_i^{0.712} Pr_i^{0.33} \tag{4.17}$$

The Reynold's number and Prandtl number are described as,

$$Re_i = \frac{u_i D_h \rho_i}{\mu_i} \tag{4.18}$$

$$Pr_i = \frac{\mu_i Cp_i}{\lambda_i} \tag{4.19}$$

The velocity u_i in equation 4.18 is calculated as

$$u_i = \frac{\dot{m}_i}{\rho_i A_{c,i}} \tag{4.20}$$

here, $A_{c,i}$ is the liquid flow cross section through the heat exchanger, which can be different for the cold side and the hot side in heat exchangers. In the equations above, i denotes the medium, either fresh water or seawater for this system.

Note that for the experimental facility fresh water is used for both streams. In that case the fresh water heat transfer coefficient and the fresh water fouling factor are used for both sides of the plate. In the case of a real pilot plant, the salt water side would have a different heat transfer coefficient and fouling factor, as shown in equation 4.14.

The Total Area for Heat Exchange A_{HE}

The total heat exchange area can be calculated by the following equation,

$$A_{HE} = n_{pl} * \phi_{pl} * A_{pl} = n * \phi_{pl} * L_{pl} * B_{pl} \tag{4.21}$$

where n_{pl} is the number of plates, A_{pl} is the area of one plate ($= L_{pl} * B_{pl}$) and ϕ_{pl} is the corrugation enhancement factor. This factor is applied because the plates have a corrugated surface and are not flat (figure 4.9). ϕ_{pl} is thus a factor that takes the corrugated surface into account to arrive at the correct total heat exchange area.

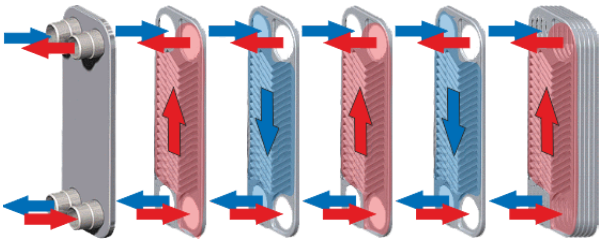

Figure 4.9: Schematic representation of a counter current flow plate heat exchanger

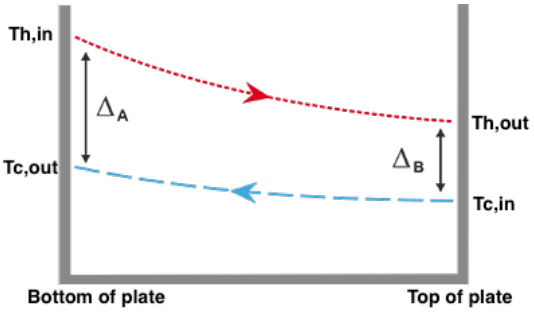

Figure 4.10: example of a countercurrent plate heat exchanger temperature diagram

The Logarithmic Mean Temperature Difference ΔT_{lm}

For a heat exchanger with counter current flow, the ideal mean temperature difference is known as the log mean temperature difference (also see figure 4.10):

$$\Delta T_{lm} = \frac{(T_{h,in} - T_{c,out}) - (T_{h,out} - T_{c,in})}{ln\left(\frac{T_{h,in} - T_{c,out}}{T_{h,out} - T_{c,in}}\right)} \tag{4.22}$$

The log mean temperature difference is the maximum mean temperature difference that can be achieved in any geometry of a heat exchanger for any given set of inlet and outlet temperatures. For a non-ideal (i.e. real) heat exchanger, the mean temperature difference can be expressed as

$$\Delta T_m = F_t * \Delta T_{lm} \tag{4.23}$$

where F_t is the log mean temperature difference correction factor for a non-ideal heat exchanger and is always less than or equal to 1. For plate heat exchangers, the value of F_t can be determined using figure 4.11, where F_t is a function of the number of transfer units (NTU) and the number of passes (flow arrangement). The NTU can be calculated using the following equation:

$$NTU = \frac{\Delta T_{max}}{\Delta T_{lm}} = \frac{T_{h,in} - T_{c,in}}{\Delta T_{lm}} \tag{4.24}$$

Typically, the NTU will range from 0.5 to 4.0, and for most applications will lie between 2.0 to 3.0 [43].

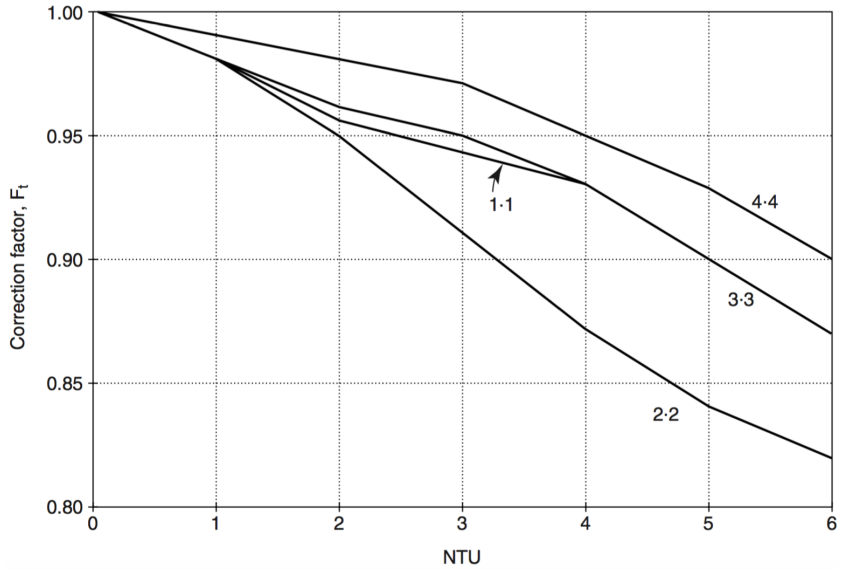

Figure 4.11: Correction factor F_t as a function of the NTU and number of passes [43]

The definition of the number of passes in figure 4.11 above (i.e. 1-1, 2-2, 3-3, etc) is shown in the figures 4.12 and 4.13.

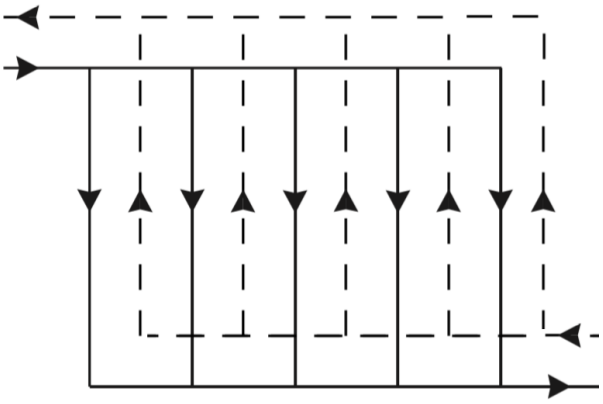

Figure 4.12: Counter-current flow, 1 pass, 5 channels per pass, 8 thermal plates, 10 plates total [43]

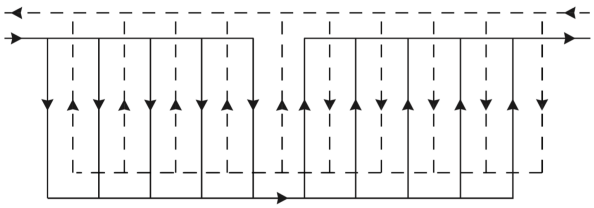

Figure 4.13: Counter-current flow, 2 passes, 5 channels per pass, 18 thermal plates, 20 plates total [43]

The number of passes for the heat exchanger in the experimental setup is one pass for both sides, thus the 1-1 curve in figure 4.11 should be followed.

4.4.2. Pressure Drop Heat Exchanger

The pressure drop in plate heat exchangers is calculated according to the VDI Heat Atlas [50] as:

$$\Delta P_{HE,i} = f_{D,i} \frac{L_{pl}}{D_h} \frac{\rho_i u_i^2}{2} \tag{4.25}$$

Here, $f_{D,i}$ is the Darcy-Weisbach friction factor. For a flat plate and laminar flow, the friction factor is described as:

$$f_{D_0,i} = \frac{B_0}{Re_i}, \quad Re_i < 2000 \tag{4.26}$$

where B_0 depends on the cross-sectional shape of the channel and often has an average value of $B_0 = 64$ [50]. Unfortunately, the heat exchanger used does not have a flat plate, and the friction factor for plates with a wave pattern must be found.

The limiting case is when the wave angle β is equal to 90°. The friction factor for the limiting case can be described as

$$f_{D_1,i} = \frac{B_1}{Re_i} + C_5, \quad Re_i < 2000 \tag{4.27}$$

where C_z, B_1 and C_5 all depend on the corrugation pattern. For the most standard heat exchangers (including the one used in the experimental setup), C_z, B_1 and C_5 are equal to 3.8, 597 and 3.85 respectively for equation 4.27 above. When the wave angle is between 0° and 90°, an equation was made dependent on both limiting friction factors above. The effects of longer flow paths, flow reversal at the edges and the crossing of rivulets have all led to the development of the following equation for the friction factor for angles between 0° and 90° [50]:

$$\frac{1}{\sqrt{f_{D,i}}} = \frac{\cos\beta}{\sqrt{0.18\tan\beta + 0.36\sin\beta + f_{D_0,i}/\cos\beta}} + \frac{1-\cos\beta}{\sqrt{3.8 f_{D_1,i}}} \tag{4.28}$$

Combining equations 4.25 and 4.28 gives the pressure drop within the heat exchanger. However, both sides also experience a pressure drop at the inlet and outlet ports of the heat exchanger. This can be described as:

$$\Delta P_{HE_{port},i} = 1.3\frac{\rho_i u_{port,i}^2}{2} = 1.3\left(\frac{\rho_i}{2}\frac{4\dot{m}_i}{\rho_i \pi D_{port}^2}\right)^2 \tag{4.29}$$

Here, $u_{port,i}$ is the liquid velocity at the port, and D_{port} is the port diameter.

4.5. Pressure Loss Total System

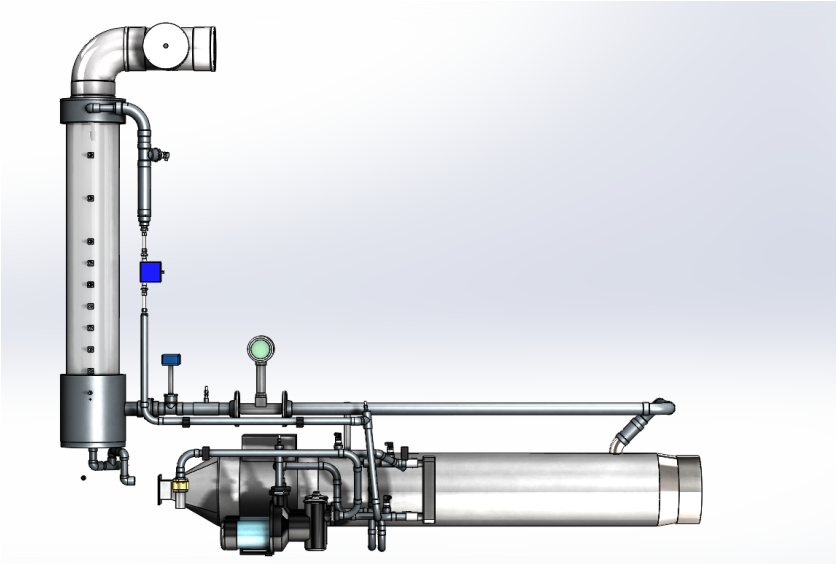

Figure 4.14: Representation of piping in the experimental setup

Aside from pressure loss inside different components such as the heat exchanger and the condenser, pressure is also lost by the transport of fluids in pipelines to and from these components. This part of the model describes the pressure lost inside pipes, on both the air and the water side, that are connected to the main components.

4.5.1. Calculation Pressure Drop Piping

The procedure used to calculate the pressure drop is described by White in his book on Fluid Mechanics [51]. Here, the Darcy-Weisbach equation is used for straight sections while bends and tees are expressed in K-factors that are added to the original equation, giving:

$$\Delta P = \frac{\rho v^2}{2}\left(f_D \frac{L_{pipe,straight}}{d_{pipe}} + \sum K\right) \tag{4.30}$$

Here

- $L_{pipe,straight}$ is the cumulative length of the straight sections
- $\sum K$ is the cumulative K-factor of the bends and tee

For laminar flow, f_D depends only on the Reynolds number. For pipe flow with a Reynolds number smaller than 2000, the Poiseuille law is used:

$$f_D = \frac{64}{Re} \tag{4.31}$$

There are no reliable friction factors in the range $2000 \leq Re_D \leq 4000$, a region known as the critical zone (see figure 4.15). According to White [51], Reynolds numbers higher than 4000 depend strongly on the roughness of the pipe. For smooth pipes, the Blasius equation can be used in the region $4000 \leq Re \leq 10^5$:

$$f_D = \frac{0.3164}{Re^{1/4}} \tag{4.32}$$

Haaland came up with an equation to combine smooth wall and fully rough relations into a single interpolation formula:

$$f_D = \left(\frac{1}{-1.8\log\left(\left(\frac{\frac{\epsilon}{D}}{3.7}\right)^{1.11} + \frac{6.9}{Re}\right)}\right)^2 \tag{4.33}$$

This equation is valid throughout the transition zone (see figure 4.15). Here, $\frac{\epsilon}{D}$ is known as the roughness ratio which is a factor that increases monotonically with turbulent friction. It depends on the diameter of the piping as well as the roughness of the walls inside the piping.

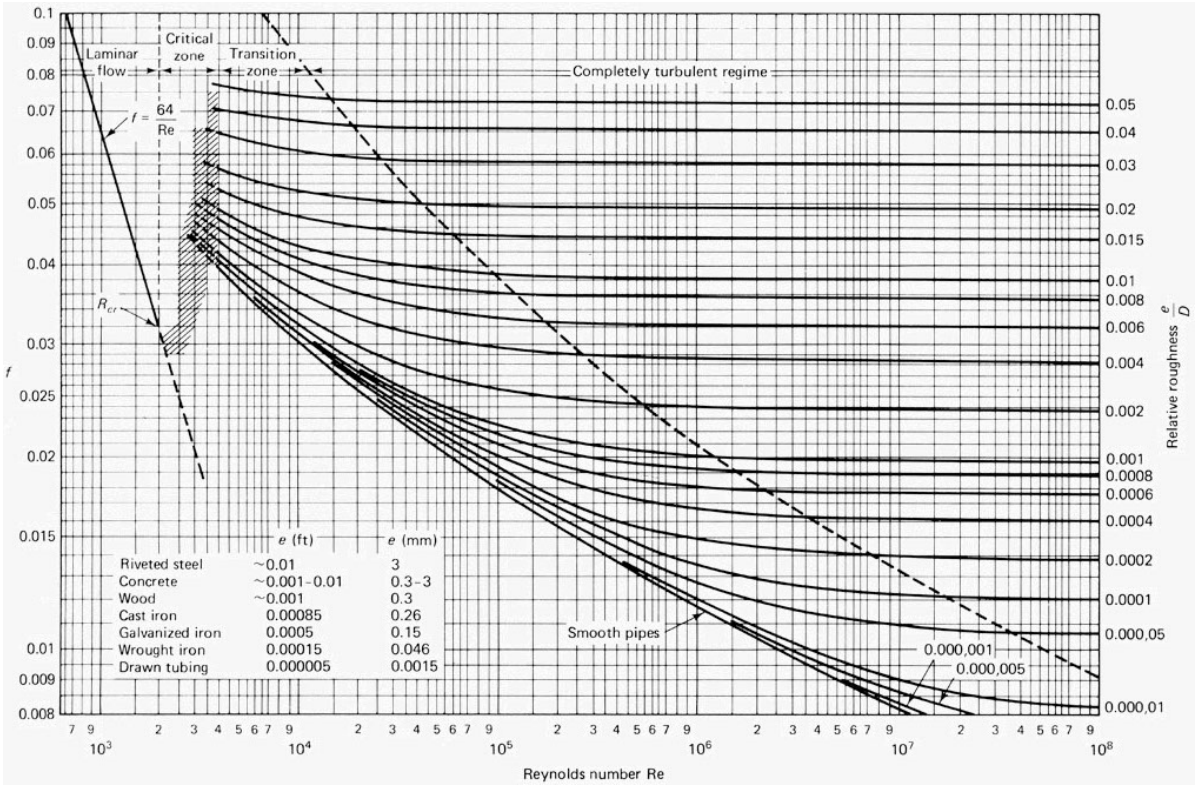

Figure 4.15: Moody Diagram from L.F. Moody [37]

The roughness ϵ_{pipe} of the PVC tubes used in the demo is 1.5*10^{-6} m. The piping diameters within the experimental setup are not smaller than 0.05 m. Therefore, the relative roughness ϵ_{pipe}/D_{pipe} does not get larger than 3*10^5, meaning that all pipes can be seen as "smooth pipes" (see figure 4.15). Thus when calculating the friction factor in the model, the Blasius equation in 4.32 will be used for turbulent flows ($2000 \leq Re_D \leq 4000$) and the Poiseuille equation in 4.31 will be used for laminar flows ($Re_D \leq 2000$). Equation 4.33 is not needed and was used in this case to help clarify the complexity of friction factor calculations.

The length of the straight sections, the K values, and the Reynolds number differ within the experimental setup. These values, together with the friction factor, are determined for each section to calculate the pressure drop in that section. Finally all pressure drops in different parts of the demo are summed to give the total pressure drop for the tubing in the experimental setup, at least for the water side.

The air side pressure drop has been calculated yet not modelled. The calculations proved important because these led to the conclusion that the diameter of the air side tubes would have to increase in order to be able to increase the air flow of the air blower (see appendix A on commissioning). Yet, these calculations were left out of the model since air piping coming from the TAG would not be needed for the design of an OTWP pilot plant.

4.5.2. Calculation other pressure drops

Nozzle water side

The pressure drop generated by the nozzle on the water side is hard to compute using the above pressure drop equations. K-factors for the nozzle are usually given by companies selling the nozzle as well as an empirical equation linking the pressure drop to the flow rate and the K factor. During this thesis, a MaxiPass nozzle (MPF-218) was ordered to increase the fresh water flow rate. Using this nozzle as an example, the pressure drop can be calculated using formula 4.34 (also see appendix F):

$$\Delta P_{L,nozzle} = \left(60000 \frac{\dot{V}_{fw}}{K}\right)^{2.12766} \tag{4.34}$$

where $\dot{V}_{fw}$ is the fresh water flow rate in m/s and K is the K-factor given for MPF-218 in appendix F (i.e. K = 20.2). An option is given in the main file of the model to choose if a water side pressure drop is to be modelled or not. If yes, a K-factor has to be given and the pressure drop is calculated in the pressure drop model. If no, this part of the waterside pressure drop is neglected.

Nozzle air side

The pressure drop on the air side that arises due to the fact that the nozzle is inside the condenser column can be modelled as a constriction in the condenser column (see figures 4.16 and 4.17). Using the Darcy Weisbach equation (4.30), F. White ([51],p. 390) gives possible K-factors for a disk type gate valve (see figure 4.16). This valve can be used to represent the brief narrowing of the condenser column by a nozzle.

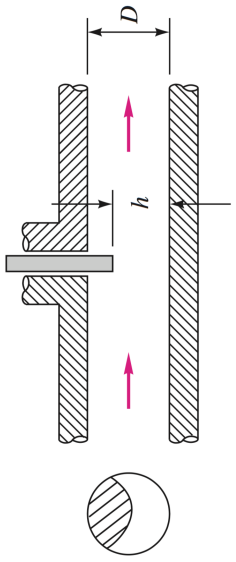

Figure 4.16: A representation of a disk gate valve, this is used to model the nozzle constriction as K-factors for this valve are available

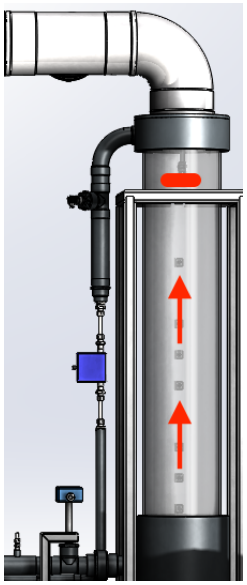

Figure 4.17: A representation of condenser column with air flow (red arrows) and the nozzle constriction (red cilinder)

When tests were done using a shower head instead of a nozzle, this pressure drop played a major factor in the condenser column. This is because the shower head took in a large

part of the cross sectional area in the condenser, thus making it harder for air to flow past it. When using flow nozzles, the pressure drop proved to be much lower (see appendix A on commissioning).

The K-values provided in White [51] unfortunately have an uncertainty of up to 50%. For this reason, there is no equation given for this part of the pressure drop and validation tests were done purely with nozzle types that proved to have little to no pressure drop when experimenting.

Height water side

Obviously water also needs to be pumped up to at least the condenser height in order for it to be sprayed inside the condenser column. The pressure difference needed to pump water from a certain height z to a certain height $z + dz$ is equal to:

$$\Delta P_{L,dz} = \rho_L g dz \tag{4.35}$$

The height difference dz of both the salt water and fresh water cycle is given as an input in the main model. This input is then used in the pressure drop model.

5

Validation

In the previous chapter, a thorough explanation was given on how the OTWP model was created. The purpose of building this model was to validate it so that the model can be used to help design a future pilot plant facility. Validation is done by comparing values obtained from the experimental setup, and seeing how well they match against values obtained by the model under the same conditions.

A brief explanation of the experimental setup will be given here. A more thorough explanation on how the experiment works and its potential difficulties are given in Appendix A. The experiment consists of 7 main components: The condenser, the air blower, the heat exchanger, the TAG (=heater+humidifier), the fresh water + OTEC pumps and the watertank. Figure 5.1 shows the experimental setup while the process and instrumentation diagram (P&ID) in appendix B shows where different variables are measured in the experiment.

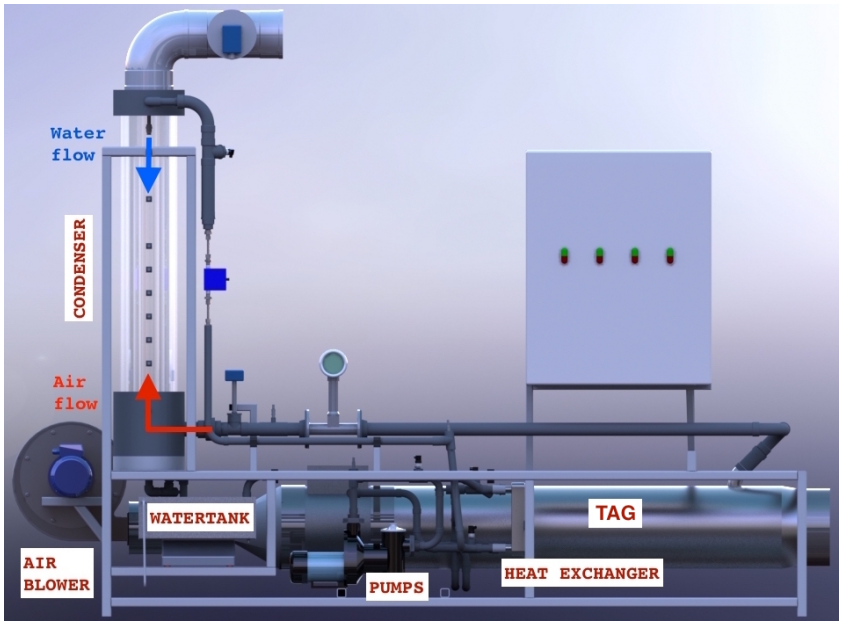

Figure 5.1: Representation of Experimental Setup showing the flow rate through the condenser as well as labelling the 7 main components of the system

The experiment measures the temperatures, pressures, humidities, and the flow rates at different parts in the system. The most important outputs are the temperature curve in the condenser, the water production rate in the condenser, and the pressure drop over the

condenser. These three outputs will be compared with the calculated values of the model. The location of the sensors used in the experiment to calculate these outputs are shown in figures 5.2 and 5.3.

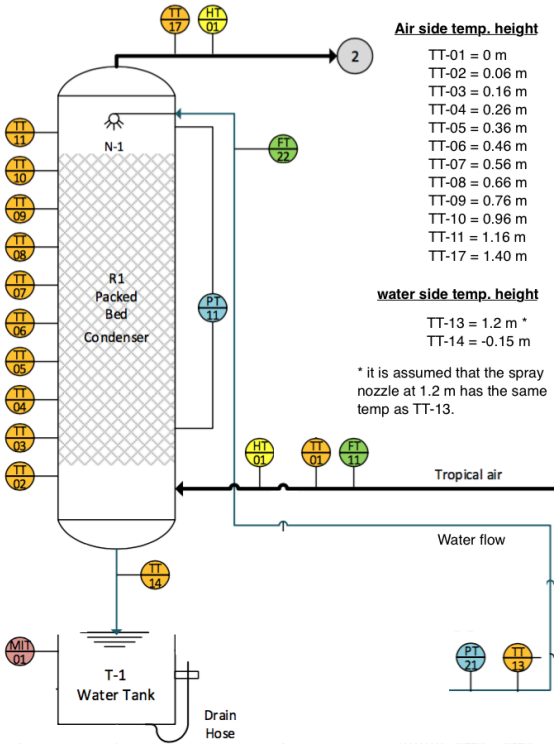

Figure 5.2: P&ID representation of the different sensors in the condenser column as well as the heights of each temperature sensor (as also used in the model)

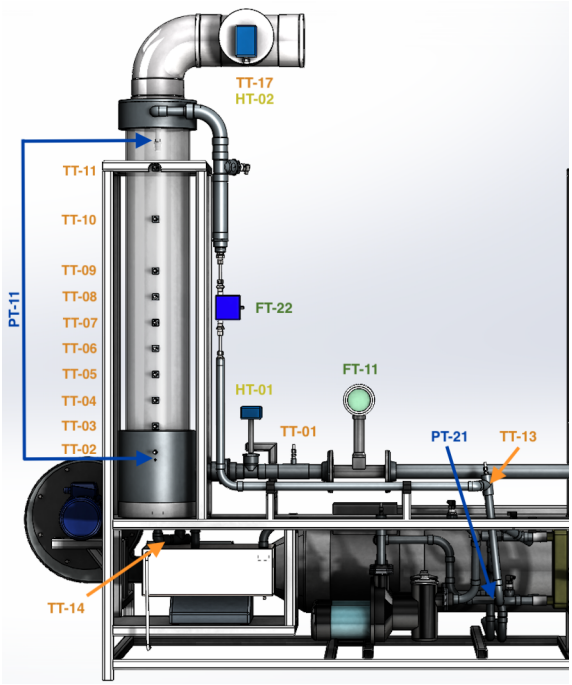

Figure 5.3: Visual representation of condenser column showing the location of the sensors. TT = temperature sensor, HT = humidity sensor, PT = pressure sensor and FT = flow sensor

An experimental 'base case' is set as a starting point for this validation study, its initial conditions are based on educated guesses as well as known tropical air and sea water conditions. The base case conditions taken to validate the model are given in table 5.1.

Table 5.1: Base case settings for experiment

Air flow in	30 L/s (= 0.03477 kg/s)
Fresh water flow in	0.075 L/s (= 0.075 kg/s)
Temperature air in	28 °C
Temperature fresh water in	12 °C
Relative humidity	79.78 %
Packing Height	1130 mm
Packing type	16 mm Metallic Pall Rings
Nozzle type	MP218

Under these conditions it is theoretically possible to extract 1.286 kg water/hr out of the air according to psychrometrics. Below, an explanation is given why each value was chosen as the base case scenario:

- The air flow rate of 0.03477 kg/s is quite low considering that Lopez suggested an air flow rate of 0.19 kg/s for this setup [30]. Unfortunately, 0.19 kg/s cannot be reached due to a relatively high air side pressure drop (see appendix A). The current maximum air flow rate is 0.058 kg/s (= 50 L/s). The lower value of 0.03477 kg/s was chosen to have the possibility of testing air flows higher than the base case.

- The fresh water flow rate of 0.0748 kg/s was initially chosen because values tested at lower flow rates resulted in insufficient wetting of the packing area by the MP218 nozzle. As can be seen in appendix F, this flow rate is already well under the workflow of the nozzle. Also, the water pumps operate near the bare minimum at this value. This flow rate corresponds to a mass flow ratio of 0.46 kg air/kg water which is a lot lower than the value of 1 kg air/kg water suggested for the pilot plant by Lopez [30]. Lopez's calculations however, used a flooding factor of 0.7, and as explained in chapter 3.4.3, it is now known that this does not necessarily result in the best efficiency. The study on optimum mass flow ratios by Bauer et al. [3] showed that very small air to water flow ratios gave better results than larger ones. The base case value of 0.0748 kg/s with a flow ratio of 0.46 may therefore not be such a bad start.

- The chosen air temperature of 28 °C and relative humidity of 80% are normal tropical air conditions and therefore taken as base case conditions. These conditions can be obtained by varying the steam mass flow and heater settings in the TAG.

- The fresh water inlet temperature is set at 12°C as this is the best temperature that can be obtained from heat exchange with salt water coming from the OTEC plant. Bluerise wants to use deep ocean seawater of 4°C-5°C for OTEC and SDC. Waste water from OTEC is expected to be around 10°C-12°C and this water is to be used for the OTWP setup. The process is shown in figure 5.4.

- The initial packing height of 1130 mm came from an optimization study by Lopez [30] for this column diameter and packing type. The height can easily be altered by adding or removing packings, as is the nature of random packings.

- The random packing type chosen for the condenser is the 16 mm metallic Pall ring. This packing type had been previously ordered by Lopez [30], and will not be altered during this study.

- The Spraybest MP218 nozzle was originally chosen as the base case nozzle as it allows a high water flow rate against a minimal water and air pressure drop, especially at low operating conditions. The initial nozzle MP125 sprayed better yet had a larger pressure drop on the water side. A showerhead was also considered to lower the pressure drop on the water side, yet due to its size in the condenser column, it significantly increased the pressure drop on the air side.

In order to validate the model with the experiment, the model base case outputs will be compared with the experimental base case outputs. Comparisons will also be made under different experimental operating conditions to verify the robustness of the model. The base case deviations investigated in this thesis are:

- changes in the relative humidity (section 5.2)

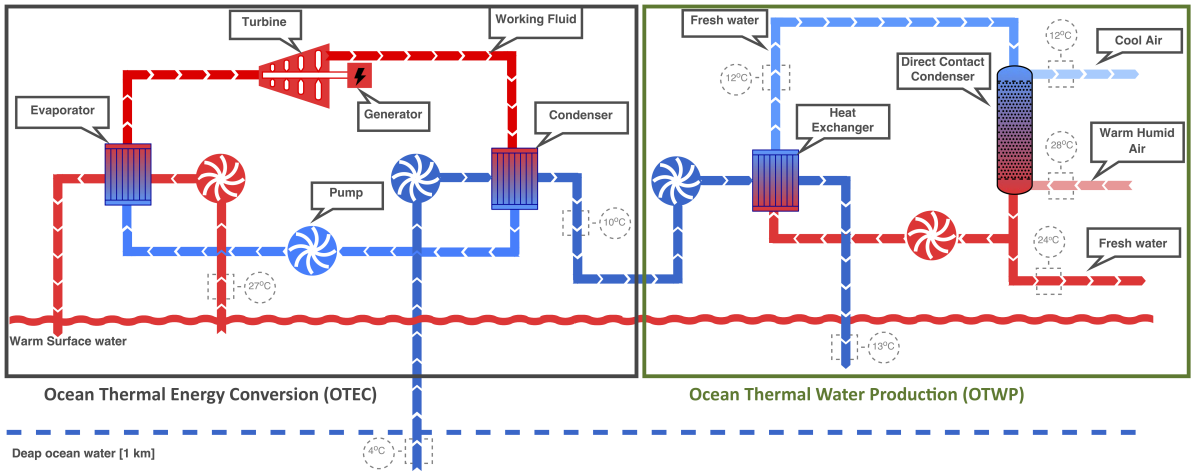

Figure 5.4: Diagram showing how OTEC waste water is utilized in the OTWP cycle

- changes in the inlet fresh water temperature, flow ratio and nozzle type (section 5.3)
- changes in the packing height (section 5.4)

The importance of using evaporative cooling or no evaporative cooling in the model is discussed in section 5.5.

5.1. Base Case Evaluation and Validation

5.1.1. Heat Transfer Evaluation

The base case conditions are tested for the three mass and heat transfer theories explained in the previous chapters: Klausner et al./Onda et al., Billet & Schultes and Mackowiak. The results are shown in figures 5.5-5.16.

The thin lines in the figures represent values obtained from the model. The thick dots with error bars represent the value and the location of the temperature sensors. The error bars show the range of the maximum and minimum values measured during the experiment, while the dot in the middle represents the mean value of the temperature sensor data at that location during the experiment. The temperature values are connected by dotted lines to show which sensors show the air, water and packing temperature distribution. At first it was thought that the temperature sensors in the packings measured air temperature and should thus follow the air temperature curve. During this thesis however, the packing temperature was added to the model, and it can be seen in the figures below that the temperature sensors within the packing tend to follow this curve.

Outside of the packing column, the air outlet and water outlet temperatures are measured. The model lines do not extend to these values since the model only measures mass and heat transfer within the packing. For large packing heights however, mass and heat transferred in the part of the column without packing is expected to be negligible, and the experimental air temperature value out should match the model's temperature out. The same counts for the fresh water temperature out. Remember that the model's fresh water temperature out is defined at the bottom of the condenser column, i.e. at $Z = 0$, while the air temperature out is defined at the top, i.e. Z = packing height.

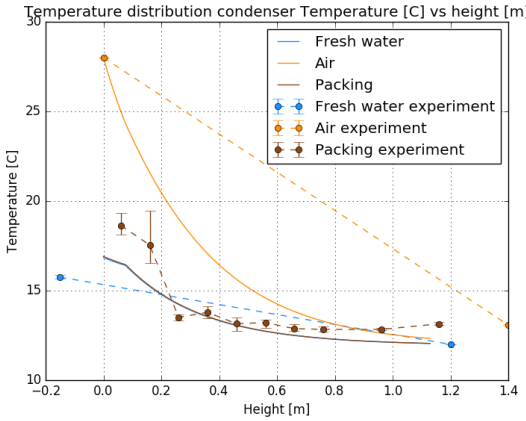

Figure 5.5: Base case Klausner et al./Onda et al. comparison temperature curves

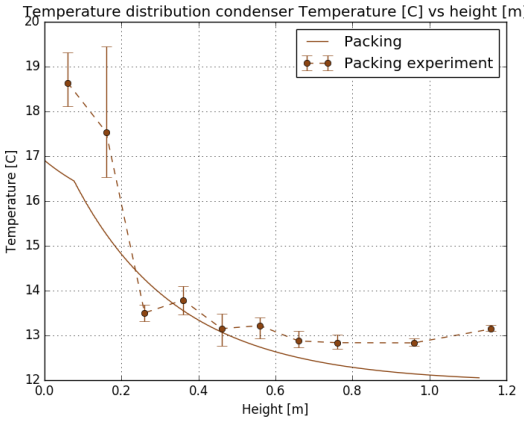

Figure 5.6: Base case Klausner et al./Onda et al. comparison packing temperature

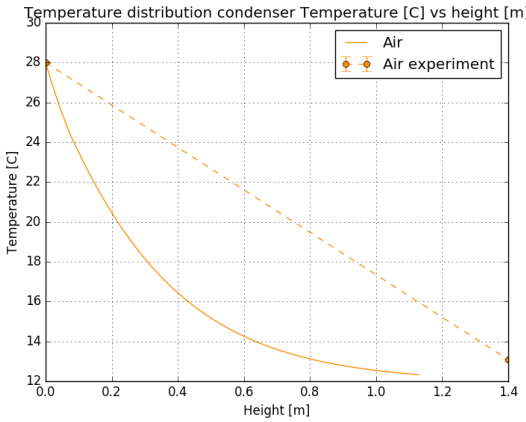

Figure 5.7: Base case Klausner et al./Onda et al. comparison air temperature

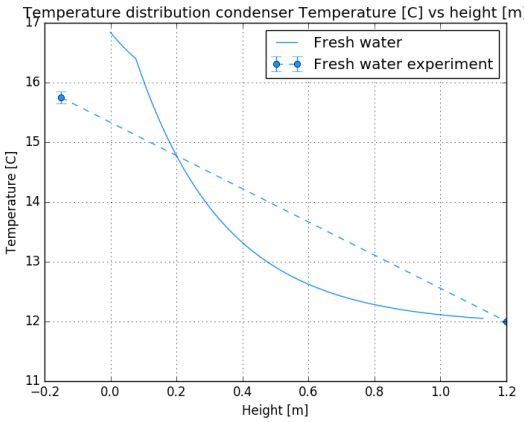

Figure 5.8: Base case Klausner et al./Onda et al. comparison water temperature

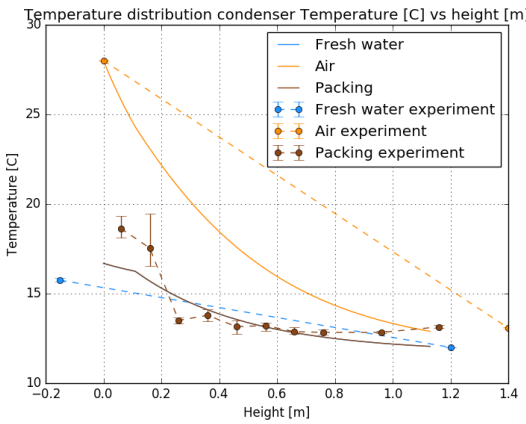

Figure 5.9: Base case Billet & Schultes comparison temperature curves

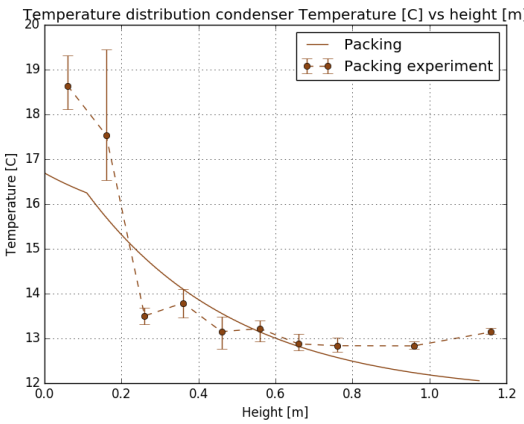

Figure 5.10: Base case Billet & Schultes comparison packing temperature

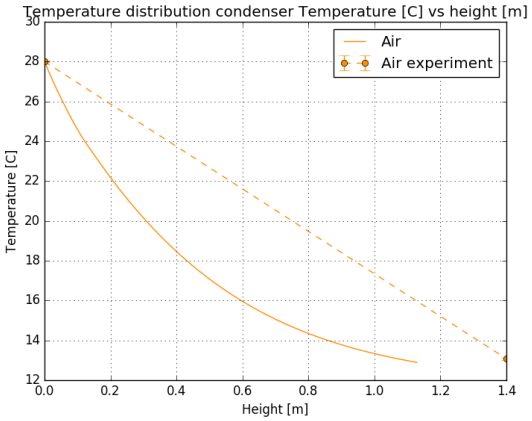

Figure 5.11: Base case Billet & Schultes comparison air temperature

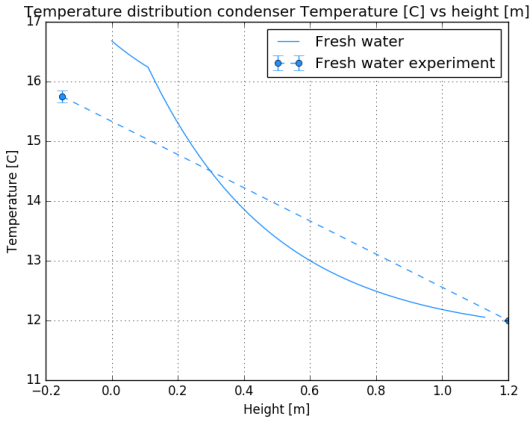

Figure 5.12: Base case Billet & Schultes comparison water temperature

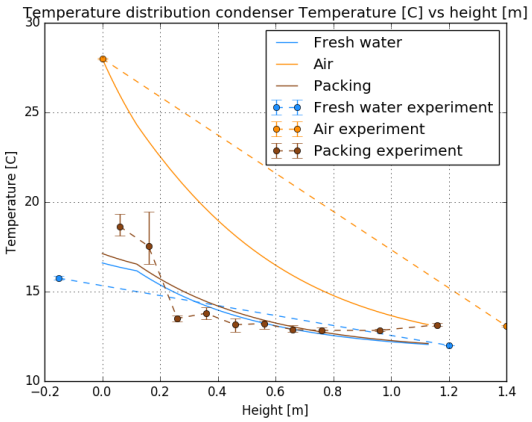

Figure 5.13: Base case Mackowiak comparison temperature curves

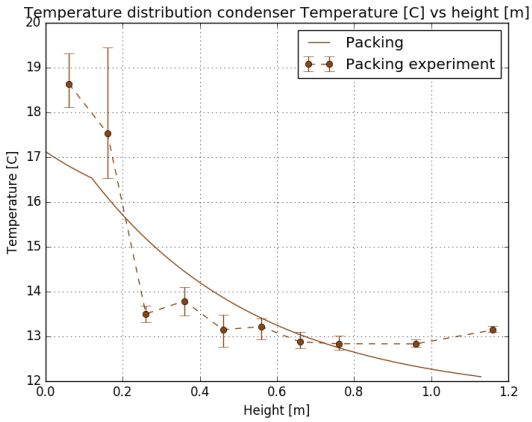

Figure 5.14: Base case Mackowiak comparison packing temperature

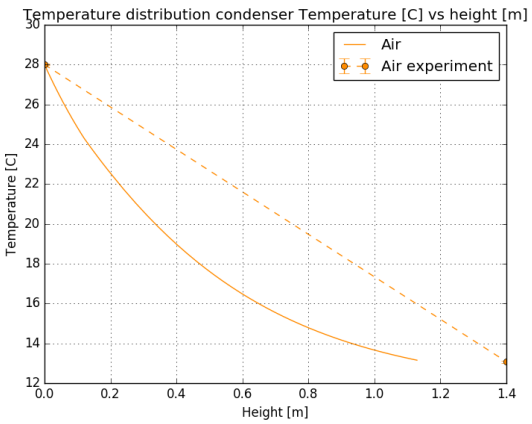

Figure 5.15: Base case Mackowiak comparison air temperature

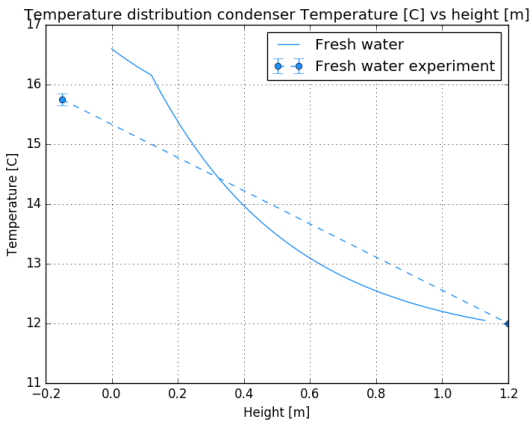

Figure 5.16: Base case Mackowiak comparison water temperature

Conclusions heat transfer:
A great sign for model validation is the fact that the air temperature value at the top of the condenser of all 3 models is approximately equal to the experimental air temperature value at the top of the condenser. Modelling the output air temperature ensures a correct prediction of the amount of water extracted from the air, at least according to psychrometrics. Air conditions according to psychrometrics can be calculated if the pressure, temperature and relative humidity are known. This visualized using a psychrometric chart shown in figure 5.17.

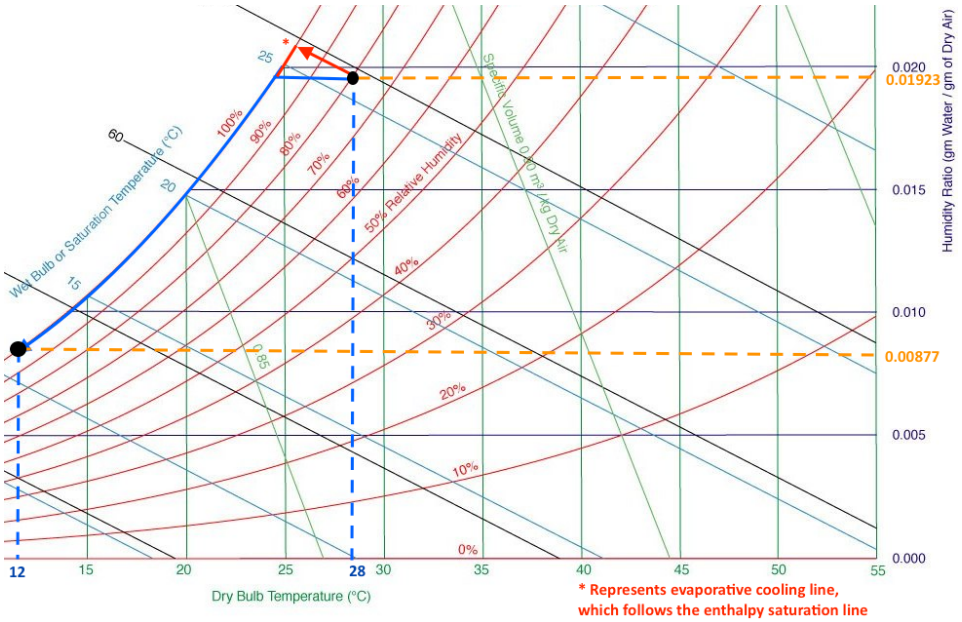

Figure 5.17: A psychrometric chart showing the amount of water transferred between 28 °C and 80% RH and 12 °C and 100% RH at atmospheric pressure

The modelled water and packing temperatures fall in between the expected experimental values for all 3 models. Apparently the packing absorbs more heat from the air than the water does, which explains why the experimental packing temperature falls above the expected value and the experimental water temperature falls below the expected value. For the model this would mean that the wetted packing area a_w is a lot lower, i.e. that there is more interaction with air and packing than with water and air.

A possible explanation why a_w should be modelled with a lower value could be the small column diameter. A column with a small diameter has a relatively large wall area. The wall area does not provide the same specific surface area of the packing a, and if a is a lot lower, then so is the wetted specific surface area a_w. In addition, wall losses also minimalize heat transfer between water and air. Wall losses have previously been investigated by Delver et al. [14] at the experimental setup. By using a heat balance it was shown that the walls needed to be isolated and a thick slab of isolation material, sold as Armaflex, has been wrapped around the column since. Still, the Armaflex slab could not be wrapped around the whole column due to space needed for the temperature sensors. Heat lost to the wall can therefore still have some impact.

It can be concluded that Mackowiak has a slightly better indication of the difference in packing temperature and water temperature. Both Billet & Schultes and Mackowiak have a good prediction of the air temperature. Onda et al.'s model follows the profiles quite well, yet it does not predict temperatures as well as the other two models. This becomes apparent when comparing other experiments as well.

5.1.2. Pressure Drop Evaluation

The Billet & Schultes and Mackowiak air side pressure drop models over the condenser height are compared in figures 5.18-5.21. The water side pressure drop model is significant yet explained in section 5.1.3 below. As mentioned earlier in chapter 3, Klausner et al. used experimental data to model the pressure drop and is therefore not compared below.

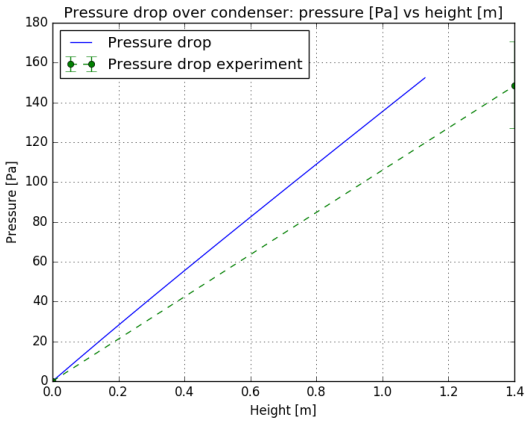

Figure 5.18: Base case Billet & Schultes comparison pressure drop

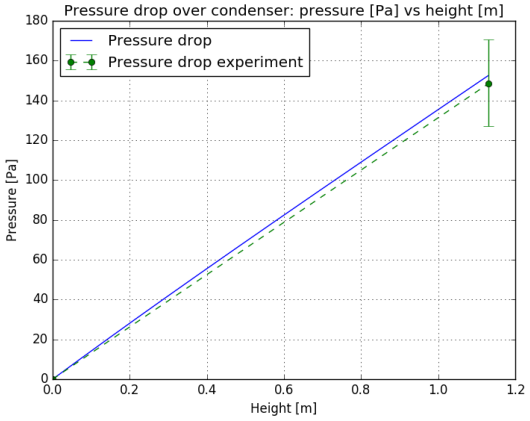

Figure 5.19: Base case Billet & Schultes comparison pressure drop (ignoring height without packing)

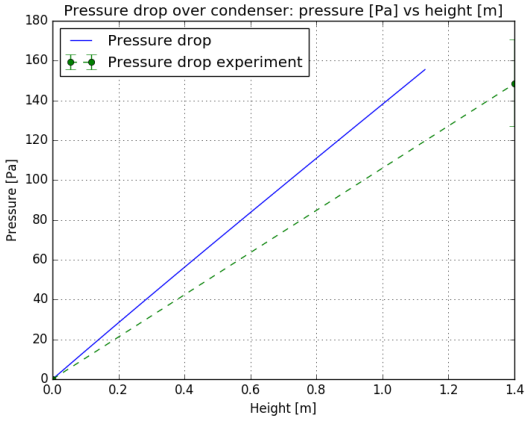

Figure 5.20: Base case Mackowiak comparison pressure drop

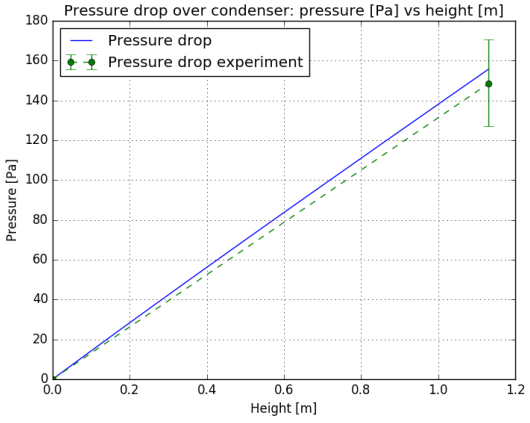

Figure 5.21: Base case Mackowiak comparison pressure drop (ignoring height without packing)

Conclusions pressure drop Mackowiak and Billet & Schultes:
As can be seen in figures 5.18 and 5.20, the pressure drop is calculated quite well for both Billet & Schultes's model and Mackowiak's model. The difference between figure 5.18 and

5.19 is that figure 5.18 shows the actual height where the pressure drop is measured, while figure 5.19 ignores the part of the height where there is no packing and the measured pressure drop is assumed to be at the same height as the packing. The same counts for figure 5.20 and 5.21. This assumption is considered valid since the part of the column that has no packing also has approximately 0 Pa pressure drop when calculated using equations from Sinnott & Towler [43]. Billet & Schultes's model seems to perform slightly better than Mackowiak's model when evaluating the pressure drop above, while both are in range of the actual value.

5.1.3. Explanation of mass transfer and techno economic analysis

The base case fresh water production rate, pressure drop and total energy consumption are given in table 5.2 for both the model and the experiments. The deviations between the experiment and each model are shown in table 5.3.

The calculation for the water production and for the air and water side pressure drops have been thoroughly explained in chapters 2, 3 and 4. The calculation for the energy consumption is briefly explained here.

The air fan and the water pumps are the only parts that require external energy for the OTWP system. The energy rate required for both the fan and the pumps can be calculated according to:

$$\dot{W} = \frac{\dot{V} dp}{\eta} \tag{5.1}$$

Typical efficiency values for water pumps are η_{pump} = 70% [17]. Fan efficiencies are split in three parts: 87% for the motor efficiency, 88% for the belt efficiency and 40% for the air fan efficiency [48], giving a total efficiency of η_{fan} = 30.6%. The energy requirement for the salt water pump is part of the techno economics of the OTEC cycle (see figure 5.4) because its waste water is utilized for the OTWP system instead of pumped back to sea. The salt water pump may thus be neglected in the energy equation and thus only the fresh water pump + air fan will be considered for the OTWP experiment.

The percentage errors for the pressure drop, water production and OTWP energy consumption in table 5.3 are calculated by dividing the deviation between the model and experiment by the absolute pressure, water production and energy values of the experiment. For instance, the pressure drop deviation model vs experiment would be:

$$\xi_{dp} = \frac{dp_{model} - dp_{exp}}{dp_{exp}} * 100\% \tag{5.2}$$

The error in the energy consumption for the OTWP system in kWh/m^3 water produced is the most significant, since this takes into account the water production relative to the pressure drop.

Taking the experimental absolute temperature value in Kelvin would lead to the mis interpretation that the model is very accurate, because the relative scale of the process is not taken into account. The temperature deviations in table 5.3 are therefore measured relative

to the maximum temperature difference of that substance in the experiment, as this is the range in which measured temperature values may lie. For instance for the air temperatures:

$$\xi_{T_G} = \frac{T_{G,modelout} - T_{G,expout}}{T_{G,in} - T_{G,expout}} * 100\% \tag{5.3}$$

and for water temperatures:

$$\xi_{T_L} = \frac{T_{L,modelout} - T_{L,expout}}{T_{L,expout} - T_{L,in}} * 100\% \tag{5.4}$$

Table 5.2: Base case evaluation water production, pressure drop and energy consumption

Variable	Value Experiment	Value Experiment	Value Experiment
Water production acc. to experiment [kg/hr]	0.850	0.850	0.850
Water production acc. to exp. psychrometrics [kg/hr]	1.205	1.205	1.205
Air side pressure drop acc. to experiment [Pa]	148.39	148.39	148.39
Water side pressure drop acc. to experiment [Pa]	19730.5	19730.5	19730.5
Energy consumption acc. to experiment [kWh/m^3]	20.13	20.13	20.13
Energy consumption acc. to exp. psychrometrics [kWh/m^3]	14.19	14.19	14.19
Variable	**Value Billet et al.**	**Value Mackowiak**	**Value Onda et al.**
Water production acc. to model [kg/hr]	1.228	1.213	1.266
Water production acc. To psychrometrics model [kg/hr]	1.227	1.212	1.265
Air side pressure drop acc. to model [Pa]	139.1	141.05	-
Water side pressure drop acc. to model [Pa]	19739	19739	-
Energy consumption acc. to model [kWh/m^3]	12.1	12.4	-

Table 5.3: Base case error evaluation between deviations experiment and model

Deviations	Percentage Billet et al.	Percentage Mackowiak	Percentage Onda et al.
fresh water side pressure drop model vs experiment	0.04%	0.04%	-
column air side pressure drop model vs experiment	-6.26%	-4.95%	-
Temp air out model vs experiment	-1.87%	-0.53%	-5.35%
Temp fw out model vs experiment	15.71%	14.14%	20.42%
Water production model vs experiment	44.47%	42.71%	48.94%
Water production model vs exp. psychrometrics	1.88%	0.63%	5.03%
Water production experiment vs exp. psychrometrics	-29.48%	-29.48%	-29.48%
Water production model vs model psychrometrics	0.08%	0.08%	0.08%
Energy consumption model vs experiment	-39.88%	-38.39%	-
Energy consumption model vs exp. psychrometrics	-14.75%	-12.64%	-

Tables 5.2 and 5.3 provide mass transfer results as well as techno economic results. The tables provide model values and experimental values, but also psychrometric data values for both the model and the experiment. This is done because the model and experiment tend to vary quite a lot in mass transfer values. Psychrometric data at the same temperature, pressure and humidity is thus used to evaluate whether the experiment or the model gives unexpected results.

5.1.4. Validation mass transfer and techno economics

One of the most interesting results in table 5.2 is the fact that the experimental water production rate was a lot lower than the the water production rate according to both experimental psychrometric values as well as the model values. This trend is also shown in other validations below.

Assuming that there is nothing wrong with the weight scale measuring water production and the humidity sensors in the experiment (both have been tested and verified prior to experiments), then the difference in production value must come from errors in temperature measurement. In order to arrive at a water production rate of 0.85 kg/hr, the air temperature out must be equal to 17.2 °C according to psychrometrics. The current measured temperature value is 13.079 °C, which suggests a temperature error of more than 4 °C. Judging from the fact that the temperature sensors have been calibrated earlier this year by Delver et al. [14] and that the maximum deviation of a PT-100 Class 'B' temperature sensor is ±0.3 °C, the temperature measured by the sensors is taken as correct and thus another explanation should be found.

Other possible options are that either condensated vapor is blown up by air in the condenser column, the spray nozzle does not distribute water well over the column, or water is lost somewhere else in the system. The flooding factor value of 0.11 given in appendix G for the base case suggests that no water droplets are swept up the column due to high air flow rates. The use of a better nozzle at the current water flow rate in section 5.3 suggests that the nozzle is not the issue. The only logical explanation left would be that there is a water leakage of around 0.35 kg/hr or that there is another resistance to mass transfer that cannot be explained by psychrometrics.

Energy consumption rates deviate a lot between experimental values and modelled values. Yet according to psychrometrics of the experiment in table 5.3, the modelled water production does not deviate more than 15% for both Billet & Schultes and Mackowiak. Unfortunately though, all the OTWP energy consumption values in table 5.2 are well above the economically feasible rates of 2-3.5 kWh/m^3.

One quick look at all the numbers and one might think that only the air side pressure drop has to be improved for economic feasibility, yet this is not the case. The water side pressure drop is shown in table 5.2 for the two pressure drop models and for the experiment. As previously explained in chapter 4, the model currently calculates the pressure drop in the piping as well as the pressure drop due to height. Pressure drop over the nozzle can be given as a constant value in the model, yet due to the low liquid flow to the nozzle, it is currently set to 0. It can be seen that the modelled water side pressure drop value of 19739 Pa is quite close to the experimental water side pressure drop value of 19730.5 Pa. This leaves a good impression that the water side pressure drop is modelled correctly. When calculating the significance of the water side pressure drop for the base case experiment, one sees that the fresh water pressure drop counts for 1.74 kWh/m^3 of the total modelled energy consumption. Keep in mind that this is already (more than) half of the economically competitive energy consumption of 2-3.5 kWh/m^3.

For the validation of the model below only the Billet & Schultes graphs will be presented. L. van der Most will be the successor of this project and her follow-up task is to design an OTWP pilot facility using this model as well as an Aspen model. Since Aspen does not provide Mackowiak's correlations yet, the Billet & Schultes heat transfer graphs are displayed below so that these can be compared with Aspen model values in the future. The tables will

still provide results from Mackowiak and Onda et al. correlations.

5.2. Changes in Relative Humidity

5.2.1. Heat Transfer

The relative humidity in the base case has been changed from 80% to 70% and 90% RH. The heat transfer comparisons are given in figures 5.22 and 5.23.

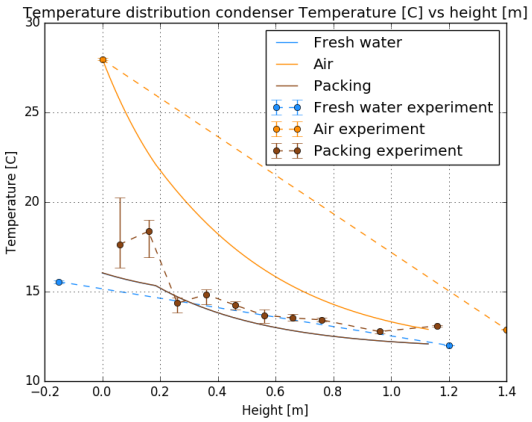

Figure 5.22: 70% RH Billet & Schultes comparison temperature curves

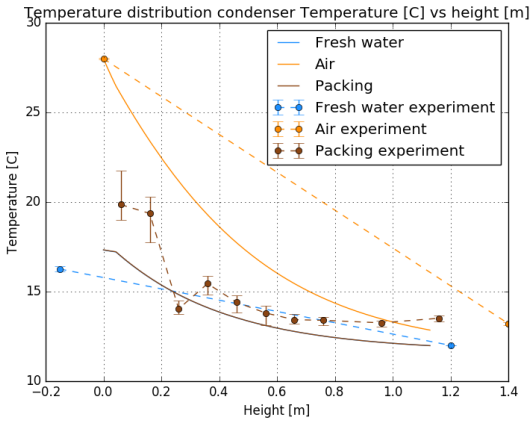

Figure 5.23: 90% RH Billet & Schultes comparison temperature curves

As can be seen above, trends in the temperature curves are similar to the ones during the base case. The air temperature curve of both the 70% RH model and the 90% RH model still predict the measured output values from experiments quite well, this should help to accurately find psychrometric water production values. The fresh water output is higher for 90% RH than for 70% RH in both the model and experimental values. This shows that more sensible heat is transferred for 90% RH than for 70% RH, which makes sense since 90% RH arrives quicker at its saturation temperature.

Another trend that occurs more explicitly in the figures above than in the base case (in particular for 90% RH), is that the experimental packing temperature has a tendency to follow the air temperature at the beginning of the column. Afterwards it quickly jumps to values that resemble the water temperature more. According to a Sulzer representative [45], a reason for this deviation could be that the distribution of water in the packing starts well, yet ends worse, which decreases the interaction between air and water. This is caused by the fact that water tends to flow down the sides of the column instead of in between the packing at large packing heights. A possible solution for optimizing water flow in the packing is to use metal sheets of 3mm wide around the packing that force water to flow back into the packing. An example of these wall wipers is given in figure 5.24.

Figure 5.24: Wall wipers around a Mellacarbon packing used in to redistribute water into the packing

The packing temperature deviation at the start of the column can also be explained by the

fact that warm air blown into the bottom of the column influences the temperature sensors at the bottom of the packing. An open gas inlet from the side of the column is used for the inlet air flow (see figure 5.25). According to Sulzer Chemtech [45], the height of where the packed bed starts plays a large roll for heat transfer. It is important to have a large enough distance between the centerline of the nozzle and the beginning of the bed for the air to evenly enter the packing (see figure 5.26). Thus, for an increased gas flow an increased height in the column should be reserved without packing. A CFD simulation can calculate the value of this height for a certain gas flow.

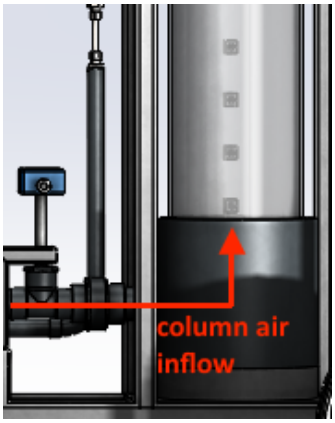

Figure 5.25: Rear view of inlet air flow experimental setup

Figure 5.26: Air flow CFD simulation to model starting height of packing. Picture taken during a meeting with Sulzer Chemtech [45]

5.2.2. Pressure Drop

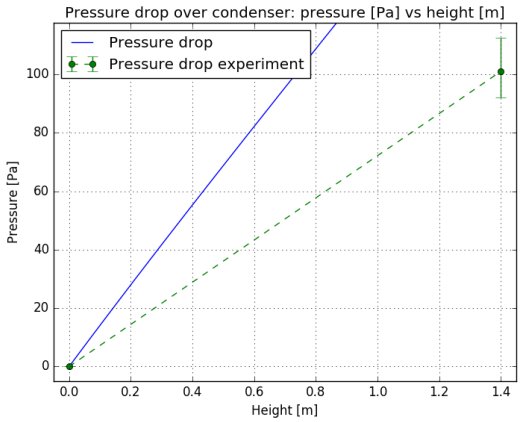

Figure 5.27: 70% RH Pressure Drop Billet & Schultes

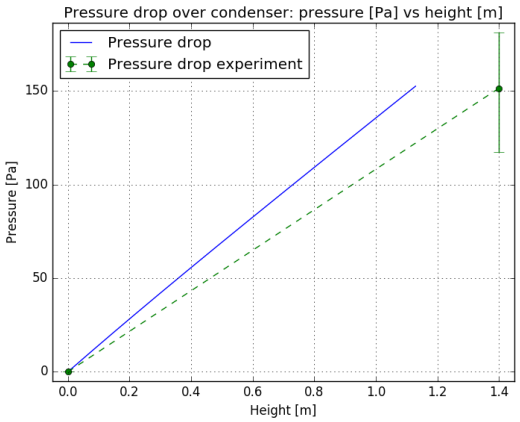

Figure 5.28: 90% RH Pressure Drop Billet & Schultes

The pressure drop is clearly modelled correctly in the 90% RH model and as expected, follows approximately the same curve as the base case (figure 5.19). It is expected that changing the relative humidity should not change the pressure drop significantly, as the small added mass in the humid air flow is negligible for the pressure drop. However as shown in both the model as well as the experiments, the air side pressure drop does deviate for different relative humidities and thus the added mass does tend to play a significant role

(please see table 5.4 below for correct 70% pressure drop value, the correct value in figure 5.28 falls out of range).

5.2.3. Mass transfer and techno economics

Table 5.4: Evaluation water production, pressure drop and energy consumption as well as model error deviations at 70% RH

Variable	Value Experiment	Value Experiment	Value Experiment
Water production acc. to experiment [kg/hr]	0.688	0.688	0.688
Water production acc. to exp. psychrometrics [kg/hr]	0.914	0.914	0.914
Air side pressure drop acc. to experiment [Pa]	101	101	101
Water side pressure drop acc. to experiment [Pa]	19500	19500	19500
Energy consumption acc. to experiment [kWh/m^3]	18.03	18.03	18.03
Energy consumption acc. to exp. psychrometrics [kWh/m^3]	13.57	13.57	13.57
Variable	**Value Billet et al.**	**Value Mackowiak**	**Value Onda et al.**
Water production acc. to model [kg/hr]	0.926	0.91	0.97
Water production acc. To psychrometrics model [kg/hr]	0.923	0.907	0.969
Air side pressure drop acc. to model [Pa]	140	142	-
Water side pressure drop acc. to model [Pa]	19623	19623	-
Energy consumption acc. to model [kWh/m^3]	16.14	16.63	-
Deviations	**Percentage Billet et al.**	**Percentage Mackowiak**	**Percentage Onda et al.**
fresh water side pressure drop model vs experiment	0.63%	0.63%	-
column air side pressure drop model vs experiment	38.61%	40.59%	-
Temp air out model vs experiment	-0.40%	0.99%	-4.37%
Temp fw out model vs experiment	9.30%	7.04%	11.55%
Water production model vs experiment	34.59%	32.27%	40.99%
Water production model vs exp. psychrometrics	1.31%	-0.44%	6.13%
Water production experiment vs exp. psychrometrics	-24.73%	-24.73%	-24.73%
Water production model vs model psychrometrics	0.33%	0.33%	0.10%
Energy consumption model vs experiment	-10.50%	-7.78%	-
Energy consumption model vs exp. psychrometrics	18.90%	22.51%	-

Table 5.5: Evaluation water production, pressure drop and energy consumption as well as model error deviations at 90% RH

Variable	Value Experiment	Value Experiment	Value Experiment
Water production acc. to experiment [kg/hr]	1.105	1.105	1.105
Water production acc. to exp. psychrometrics [kg/hr]	1.490	1.490	1.490
Air side pressure drop acc. to experiment [Pa]	152.7	152.7	152.7
Water side pressure drop acc. to experiment [Pa]	19487	19487	19487
Energy consumption acc. to experiment [kWh/m^3]	15.85	15.85	15.85
Energy consumption acc. to exp. psychrometrics [kWh/m^3]	11.75	11.75	11.75
Variable	**Value Billet et al.**	**Value Mackowiak**	**Value Onda et al.**
Water production acc. to model [kg/hr]	1.526	1.51	1.573
Water production acc. To psychrometrics model [kg/hr]	1.526	1.51	1.574
Air side pressure drop acc. to model [Pa]	138.28	140	-
Water side pressure drop acc. to model [Pa]	19740	19740	-
Energy consumption acc. to model [kWh/m^3]	9.66	9.87	-
Deviations	**Percentage Billet et al.**	**Percentage Mackowiak**	**Percentage Onda et al.**
fresh water side pressure drop model vs experiment	1.30%	1.30%	-
column air side pressure drop model vs experiment	-9.44%	-8.32%	-
Temp air out model vs experiment	-2.84%	-1.49%	-7.24%
Temp fw out model vs experiment	19.25%	17.37%	21.13%
Water production model vs experiment	38.10%	36.65%	42.35%
Water production model vs exp. psychrometrics	2.42%	1.34%	5.57%
Water production experiment vs exp. psychrometrics	-25.84%	-25.84%	-25.84%
Water production model vs model psychrometrics	0.00%	0.00%	-0.06%
Energy consumption model vs experiment	-39.04%	-37.71%	-
Energy consumption model vs exp. psychrometrics	-17.80%	-16.01%	-

As expected the water production rates as well as the process efficiency increases for higher relative humidity values for both the experiment and the model. Unfortunately, water production rates in tables 5.4 and 5.5 deviate a lot between the model and the experiment. The experiment production rates also deviate from their own psychrometric values, while model values perfectly follow psychrometrics. Possible explanations for the experimental deviations have been previously analyzed in section 5.1.4. Heat and mass transfer is described more accurately by Mackowiak's droplet model than Billet & Schultes film flow model. When analyzing the techno economics of the model with experiment psychrometrics, the percentage errors stay between 16% and 23%.

5.3. Changes in nozzle type, inlet water temperature and air flow

In the previous section, packing temperatures were continuously higher than modelled, especially at the bottom of the column. This test explicitly increases heat and mass transfer between water and air to see if the packing temperature sensors can be modelled correctly. This is done by:

1. decreasing the initial water temperature to 8°C, hereby increasing the temperature difference between air and water
2. changing the nozzle to a smaller spray nozzle type. MP218 is replaced by MP125 since the latter has a better ("mistier") water distribution at this flow rate.
3. maximizing the air flow to 50 L/s (= 0.05795 kg/s), which inevitably increases the mass flow ratio to 0.78. Previous validations showed that the air temperature approaches inlet water conditions well, and the model suggests that this happens relatively fast. It can therefore be concluded that mass and heat transfer can be increased by increasing the air flow to provide a more gentle slope of the modelled air curve.

The experiment input values are displayed in table 5.6.

Table 5.6: Experiment with new nozzle, higher air flow rate and lower inlet water temperature

Variable	Value
Air flow in	50 L/s (= 0.05795 kg/s)
Fresh water flow in	0.074 L/s (= 0.074 kg/s)
Temperature air in	29.19 °C
Temperature fresh water in	8.03 °C
Relative humidity	80 %
Packing Height	1130 mm
Packing type	16 mm Metallic Pall Rings
Nozzle type	MP125

5.3.1. Heat transfer

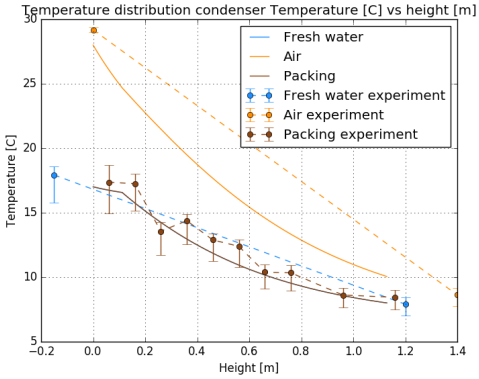

Figure 5.29: Total Temperature Distribution Billet & Schultes for MP125 nozzle, $T_{L,in}$ = 8 °C and air flow rate = 0.05795 kg/s

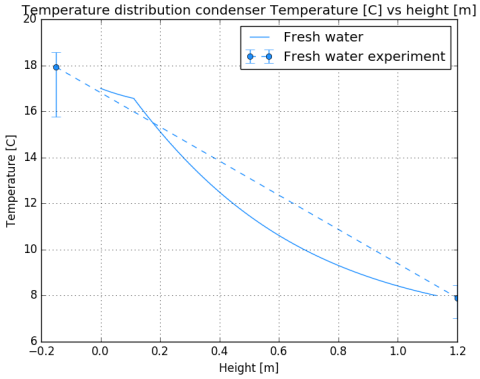

Figure 5.30: Water Temperature Distribution Billet & Schultes for MP125 nozzle, $T_{L,in}$ = 8 °C and air flow rate = 0.05795 kg/s

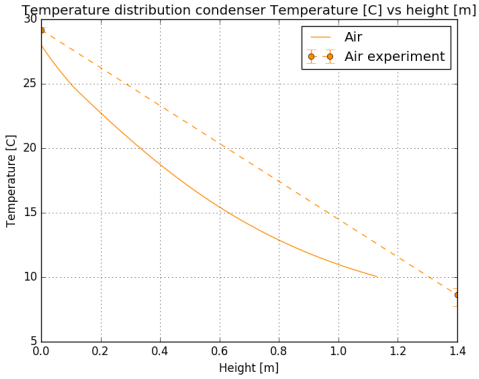

Figure 5.31: Air Temperature Distribution Billet & Schultes for MP125 nozzle, $T_{L,in}$ = 8 °C and air flow rate = 0.05795 kg/s

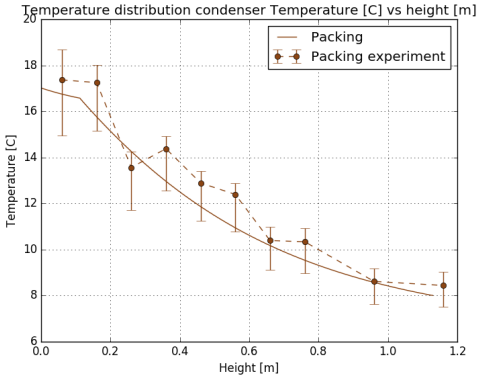

Figure 5.32: Packing Temperature Distribution Billet & Schultes for MP125 nozzle, $T_{L,in}$ = 8 °C and air flow rate = 0.05795 kg/s

As can be seen in the figures 5.29 - 5.32, the packing temperature as well as the water temperature are much more accurate than in the previous chapter. The air temperature is modelled slightly higher, but stays within 10% of the experimental value as is shown in table 5.7.

5.3.2. Pressure drop

The air side experimental pressure drop is almost twice the size of the modelled pressure drop. This is also true for Mackowiak's pressure drop as can be seen in figure 5.34. The nozzle type is a variable changed in the experiment that is not yet calculated in the model. The difference in air side pressure drop could be caused by the difference in aerodynamics of the spray nozzles. Examples of this are also given in appendix A on commissioning. The size difference between the MP125 and MP218 nozzle is quite minimal though. In fact, the MP125 is even smaller, suggesting that the nozzle type cannot provide the large difference in pressure drop.

When analyzing different experiments, it can be shown that when the air flow is increased to the maximum flow rate, the increase in pressure drop is significantly more than the mod-

elled pressure drop. L. van der Most, a student currently modelling the OTWP setup for Bluerise in Aspen [10], experiences the same issues with the pressure drop at higher flow rates. Apparently something in the experiment increases the pressure drop more than theory suggests at high flow rates. An educated guess would be that due to the small column diameter, turbulence increases at a faster rate than is currently modelled. Analyzing the Reynolds numbers at high flow rates and revising the obtained friction factors would be a good future step to fix this issue.

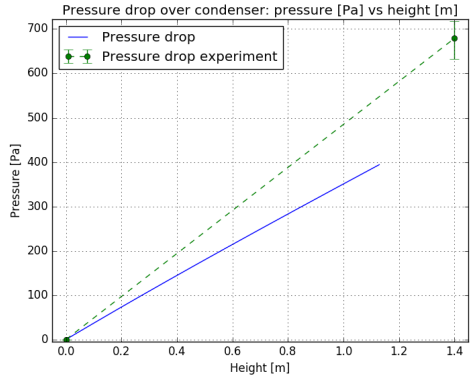

Figure 5.33: Billet & Schultes comparison pressure drop for MP125 nozzle, $T_{L,in}$ = 8 °C and air flow rate = 0.05795 kg/s

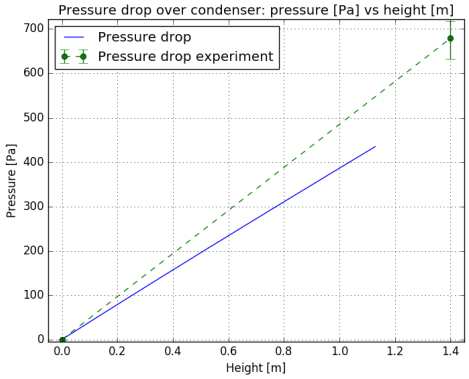

Figure 5.34: Mackowiak comparison pressure drop for MP125 nozzle, $T_{L,in}$ = 8 °C and air flow rate = 0.05795 kg/s

5.3.3. Mass transfer and techno economics

Table 5.7: Evaluation water production, pressure drop and energy consumption as well as model error deviations for MP125, 50 L/s air flow rate and 8 °C water temp. inflow

Variable	Value Experiment	Value Experiment	Value Experiment
Water production acc. to experiment [kg/hr]	2.144	2.144	2.144
Water production acc. to exp. psychrometrics [kg/hr]	2.770	2.770	2.770
Air side pressure drop acc. to experiment [Pa]	679.4	679.4	679.4
Water side pressure drop acc. to experiment [Pa]	19519	19519	19519
Energy consumption acc. to experiment [kWh/m^3]	55.35	55.35	55.35
Energy consumption acc. to exp. psychrometrics [kWh/m^3]	42.84	42.84	42.84
Variable	**Value Billet et al.**	**Value Mackowiak**	**Value Onda et al.**
Water production acc. to model [kg/hr]	2.646	2.545	2.75
Water production acc. To psychrometrics model [kg/hr]	2.648	2.547	2.75
Air side pressure drop acc. to model [Pa]	356	390.82	-
Water side pressure drop acc. to model [Pa]	19742	19742	-
Energy consumption acc. to model [kWh/m^3]	20.97	23.93	-
Deviations	**Percentage Billet et al.**	**Percentage Mackowiak**	**Percentage Onda et al.**
fresh water side pressure drop model vs experiment	1.14%	1.14%	-
column air side pressure drop model vs experiment	-47.60%	-42.48%	-
Temp air out model vs experiment	6.16%	10.56%	0.98%
Temp fw out model vs experiment	-6.54%	-9.76%	-2.52%
Water production model vs experiment	23.41%	18.70%	28.26%
Water production model vs exp. psychrometrics	-4.48%	-8.12%	-0.72%
Water production experiment vs exp. psychrometrics	-22.60%	-22.60%	-22.60%
Water production model vs model psychrometrics	-0.08%	-0.08%	0.00%
Energy consumption model vs experiment	-62.11%	-56.77%	-
Energy consumption model vs exp. psychrometrics	-51.05%	-44.14%	-

As shown in table 5.7, mass transfer is predicted quite well by all models when compared to experimental psychrometric values. Onda et al.'s correlations even predict psychrometric experimental water production rates within 1% error. Interesting to see is that Mackowiak has the worst mass transfer predictions under these conditions, while previously always providing the best predictions. The energy consumption is horribly predicted. This is mainly due to the large deviation in the air side pressure drop predictions. It can be seen how important it is to keep the air side pressure drop low, as the psychrometric experimental energy consumption predictions in kWh/m^3 are double that of the model predictions.

5.4. Changes in Packing Height

The previous chapter showed the importance of low air side pressure drops. The main initiator of pressure drop in a packed bed column is obviously the packing itself. Therefore, the model and the experimental water production rates are tested by lowering packing heights in the experiment. At a certain point, it is expected that water production rates will lower significantly due to the fact that not enough packing is used for sufficient heat and mass transfer between air and water. This can help identify the ideal packing height for the experiment at a flow rate of 30 L/s. Also, the model reliability is tested for very low packing heights.

5.4.1. Heat transfer

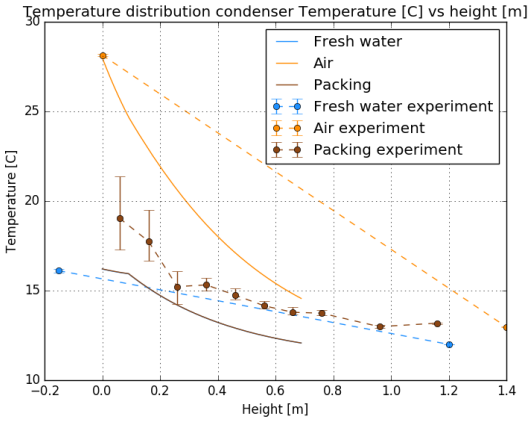

Figure 5.35: 690 mm packing Billet & Schultes comparison temperature curves

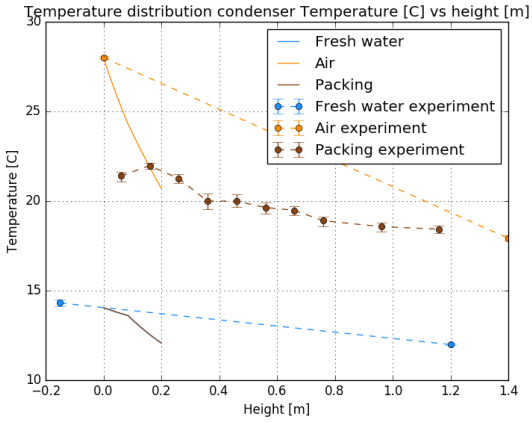

Figure 5.36: 200 mm packing Billet & Schultes comparison temperature curves

As can be seen from figure 5.35, a packing height of 690 mm still provides sufficient cooling for heat transfer. Here, the air temperature is modelled slightly too high, the modelled packing temperatures fall in between their expected experimental values and the water predictions are quite accurate. This suggests that the packing absorbs more heat from the air in the experiment, which also provides an explanation for the lower experimental air temperature.
Figure 5.36 clearly shows that the packing height is too low for sufficient heat transfer. A very interesting conclusion clearly shown in this experiment is that the temperature sen-

sors inside the column tend to follow air temperatures after after 200 mm of packing material. The same effect can be seen for the other experiment after 690 mm of packing material. By following the "packing temperature line" after 200 mm in figure 5.36 and after 690 mm in figure 5.35, the data points show that heat is also transferred in the (relatively large) column space without packing material. Another conclusion would be that as long as the temperature sensors in the packing are dry, then the air temperature will be measured in the column instead of the packing temperature, as previously thought above. In order to test this, it is recommended to build a casing around the temperature sensors to protect them from being wetted. For instance, a half shell around the top half of each temperature sensor inside the column should suffice.

5.4.2. Pressure drop

The pressure drop is modelled correctly for the 690 mm packing height in figure 5.37. Values experimented at 200 mm show larger deviations between the model and the experiment pressure drop. This deviation of around 40 Pa could possibly come from the low hanging spray nozzle in combination with the connected shaft added to the condenser column for low packing heights.

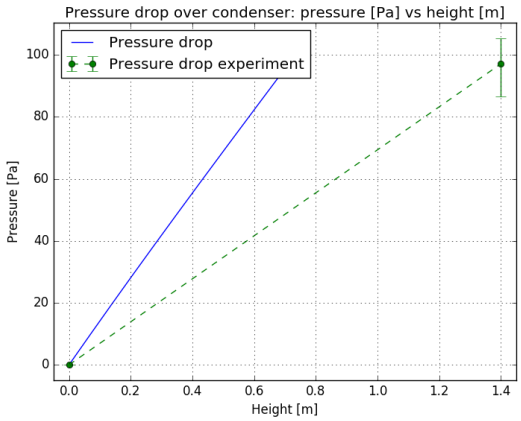

Figure 5.37: 690 mm Pressure Drop Billet & Schultes

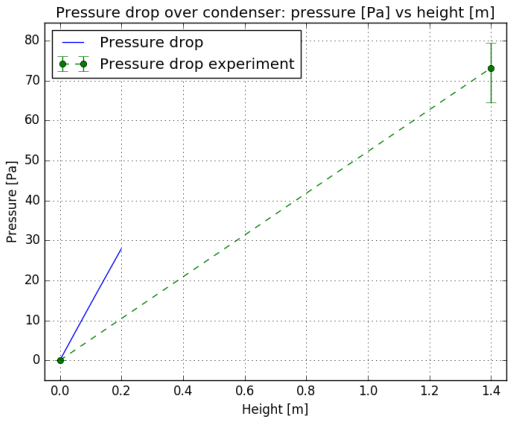

Figure 5.38: 200 mm Pressure Drop Billet & Schultes

5.4.3. Mass transfer and techno economics

From the results in table 5.8 it can be seen that the water production rates predicted by the model deviate less than 10% from the psychrometric water production rates. The output air temperature value used for psychrometrics is taken as the mean of temperature sensor values located just below and just above 690 mm packing height. This is considered correct as it has been shown that these sensors tend to follow air temperature values in section 5.4.1. The same was done for the 200 mm packing, although it can be seen in table 5.9 that the model values do no represent the experimental values well for this height.

The total energy consumption from the real experiment is 14.07 kWh/m^3 for a packing height of 690 mm. This is the lowest experimental energy cost measured during the course of this project. Even if psychrometric values were used, the experimental setup would still operate above 10 kWh/m^3. Unfortunately this is still far above the economically feasible

value of 2-3.5 kWh/m^3.

Table 5.8: Evaluation water production, pressure drop and energy consumption as well as model error deviations for 690 mm packing height

Variable	Value Experiment	Value Experiment	Value Experiment
Water production acc. to experiment [kg/hr]	0.855	0.855	0.855
Water production acc. to exp. psychrometrics [kg/hr]	1.170	1.170	1.170
Air side pressure drop acc. to experiment [Pa]	97.1	97.1	97.1
Water side pressure drop acc. to experiment [Pa]	19538	19538	19538
Energy consumption acc. to experiment [kWh/m^3]	14.07	14.07	14.07
Energy consumption acc. to exp. psychrometrics [kWh/m^3]	10.28	10.28	10.28
Variable	**Value Billet et al.**	**Value Mackowiak**	**Value Onda et al.**
Water production acc. to model [kg/hr]	1.119	1.08	1.211
Water production acc. To psychrometrics model [kg/hr]	1.116	1.078	1.21
Air side pressure drop acc. to model [Pa]	86	87	-
Water side pressure drop acc. to model [Pa]	19740	19740	-
Energy consumption acc. to model [kWh/m^3]	8.97	9.405	-
Deviations	**Percentage Billet et al.**	**Percentage Mackowiak**	**Percentage Onda et al.**
fresh water side pressure drop model vs experiment	1.03%	1.03%	-
column air side pressure drop model vs experiment	-11.43%	-10.40%	-
Temp air out model vs experiment	4.79%	7.99%	-3.26%
Temp fw out model vs experiment	-1.70%	-3.65%	8.03%
Water production model vs experiment	30.88%	26.32%	41.64%
Water production model vs exp. psychrometrics	-4.36%	-7.69%	3.50%
Water production experiment vs exp. psychrometrics	-26.92%	-26.92%	-26.92%
Water production model vs model psychrometrics	0.27%	0.19%	0.08%
Energy consumption model vs experiment	-36.25%	-33.15%	-
Energy consumption model vs exp. psychrometrics	-12.76%	-8.53%	-

Table 5.9: Evaluation water production, pressure drop and energy consumption as well as model error deviations for 200 mm packing height

Variable	Value Experiment	Value Experiment	Value Experiment
Water production acc. to experiment [kg/hr]	0.359	0.359	0.359
Water production acc. to exp. psychrometrics [kg/hr]	0.353	0.353	0.353
Air side pressure drop acc. to experiment [Pa]	73.3	73.3	73.3
Water side pressure drop acc. to experiment [Pa]	19559	19559	19559
Energy consumption acc. to experiment [kWh/m^3]	25.96	25.96	25.96
Energy consumption acc. to exp. psychrometrics [kWh/m^3]	26.40	26.40	26.40
Variable	**Value Billet et al.**	**Value Mackowiak**	**Value Onda et al.**
Water production acc. to model [kg/hr]	0.48	0.425	0.668
Water production acc. To psychrometrics model [kg/hr]	0.47	0.416	0.668
Air side pressure drop acc. to model [Pa]	25.44	25.8	-
Water side pressure drop acc. to model [Pa]	19740	19740	-
Energy consumption acc. to model [kWh/m^3]	9.47	10.8	-
Deviations	**Percentage Billet et al.**	**Percentage Mackowiak**	**Percentage Onda et al.**
fresh water side pressure drop model vs experiment	0.93%	0.93%	-
column air side pressure drop model vs experiment	-65.29%	-64.80%	-
Temp air out model vs experiment	-15.38%	-8.01%	-42.23%
Temp fw out model vs experiment	-15.15%	-22.08%	9.09%
Water production model vs experiment	33.70%	18.38%	86.07%
Water production model vs exp. psychrometrics	35.98%	20.40%	89.24%
Water production experiment vs exp. psychrometrics	1.70%	1.70%	1.70%
Water production model vs model psychrometrics	2.13%	2.16%	0.00%
Energy consumption model vs experiment	-63.52%	-58.39%	-
Energy consumption model vs exp. psychrometrics	-64.13%	-59.09%	-

5.5. Importance Evaporative Cooling

The significance of assuming if evaporative cooling takes place is modelled in figures 5.39-5.42 using Billet & Schultes's model. The base case with 70% RH is used because low relative humidities wil experience the largest effect of evaporative cooling (since more water needs to evaporate to reach saturation).

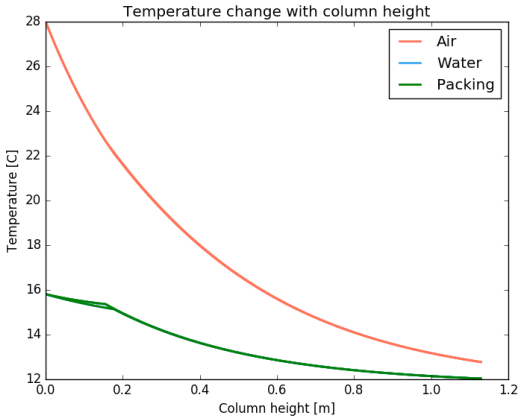

Figure 5.39: Base case 70% RH Billet & Schultes temperature comparison evaporative cooling vs no evaporative cooling

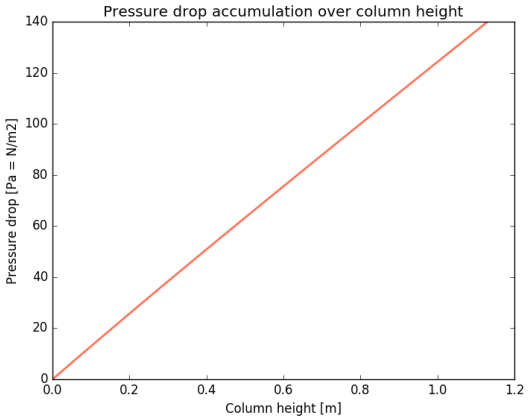

Figure 5.40: Base case 70% RH Billet & Schultes pressure drop comparison evaporative cooling vs no evaporative cooling

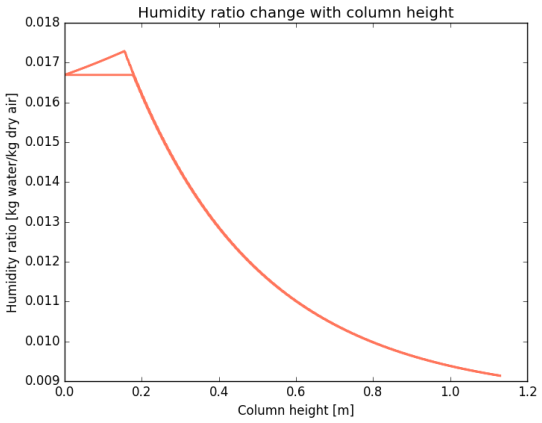

Figure 5.41: Base case 70% RH Billet & Schultes humidity comparison evaporative cooling vs no evaporative cooling

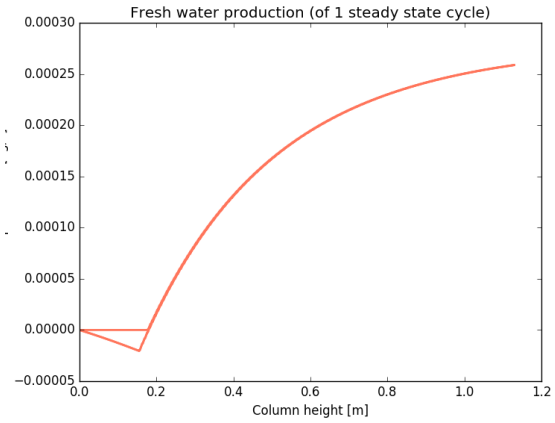

Figure 5.42: Base case 70% RH Billet & Schultes water production comparison evaporative cooling vs no evaporative cooling

Figure 5.39 shows that evaporative cooling has a negligible effect on the temperature curve. This suggests that it is not possible to relate experimental temperature graphs with modelled graphs to find out if evaporative cooling occurs or not. The pressure drop depends on the flow rate and the packing type, and thus it is expected that evaporative cooling should not change the pressure drop. Fortunately this is also the case in figure 5.40.

Figures 5.41 and 5.42 do show visible deviations when modelling with and without evaporative cooling. From table data, the water production with evaporative cooling is 0.93131 kg/hr and without evaporative cooling 0.93176 kg/hr. This is a water production deviation of 0.05%. As expected, water production without evaporative cooling results in a higher

production rate, yet the production difference is so low, that the mass transfer effect of evaporative cooling may be neglected, even for low RH tropical air conditions.

As described by Klausner et al. [27], evaporative cooling does seem to occur in most systems, and thus it will be used in model predictions, despite its minimal impact.

6

Conclusions and Recommendations

This master thesis project improves a previously researched OTWP model and validates the model by testing its output values against experiments done using an experimental setup at the TU Delft P&E laboratory. The theoretical background in chapter 2 as well as the mass and heat transfer correlations in chapter 3 provide a solid base for any person interested in learning more about the thermodynamics behind OTWP. Chapter 4 clearly explains how each submodel is built and improved. The heat exchanger and humidifier models in this chapter primarily use experimental data to arrive at correct conclusions on heat and mass transfer (see for instance the calculation of the Nusselt number in section 4.4.2) and thus both the models have been left out of the validation section in chapter 5. Below the main results and recommendations are given backed by previously analyzed experiments.

6.1. Main Conclusions

The 1968 mass and heat transfer correlations created by Onda et. al [38] and originally used in Klausner et al.'s water condensation model [1] are a great way to introduce OTWP. Yet the Onda et al. correlations do not provide the best accuracy for building a reliable model. Using the same film flow concept to model mass and heat transfer, the correlations provided by Billet & Schultes in 1999 [9] provide a model which is much more accurate and reliable for the OTWP experimental setup, as can be seen in the previous chapter on validation 5.

Mackowiak's suspended bed of droplets model is fundamentally different than the film flow model for mass and heat transfer created by Onda et al. or Billet & Schultes. As explained in chapter 3 on mass and heat transfer correlations, Mackowiak's model assumes heat and mass transfer between droplets of water and air, instead of a film of water and air. It is applicable if the average air velocity is higher than the critical air velocity. Yet, due to the way the critical velocity equation is defined, the average velocity will always meet this case, therefore allowing this theory to always be applied. It is thus important to rely on experimental data from Mackowiak to learn more about the reliability of the droplet model.

When looking at the current validated experimental results in chapter 5, both Billet's model and Mackowiak's model are quite accurate in determing experimental heat transfer values. Air side temperature predictions fall below an error percentage of 10% while the model's fresh water side temperature predictions stay within a 20% error range. The air side pressure drops are quite accurate when Mackowiak and Billet & Schultes models are compared to each other, and relatively accurate when compared to the experimental setup. When operating at high flow rates however, the pressure drop model fails to predict correct values.

It is recommended to reanalyze and validate the flow regimes in the condenser column for high flow rates.

Both of the mass transfer results of Mackowiak and Billet & Schultes constantly deviate around 25-35% of the experimental values. The poor mass transfer results automatically have a negative effect on the energy consumption predictions as well. However, when mass transfer results are compared to experimental psychrometric air data values, the mass transfer deviations stay well under 10% of the outcome. Energy consumption predictions (in kWh/m^3) stay within an error range of 10%-20% when compared to psychrometric values. The main reason why the experiment deviates from expected psychrometric values is thought to depend on the poor water distribution in the column by the MP218 nozzle. Yet even when using the MP125 nozzle, which should operate well under the base case water flow conditions (appendix F), experimental water production rates still deviate a lot from psychrometrics (see section 5.3). Section 5.1.4 thoroughly analyzes possible explanations for this deviation, yet eventually arrives at the conclusion that there is either a water leakage or some other resistance to mass transfer in the column that cannot be explained by psychrometric data.

Whatever the reason might be, it can certainly be concluded that the current experimental setup, as well as the current model predictions under the same operating conditions, do not provide economically competitive results for a future OTWP pilot plant. The lowest experimental prediction was 14 kWh/m^3 water produced, while the lowest model predictions under the same operating conditions was 9 kWh/m^3.

In order to optimize this experimental setup, or even a future setup, it is going to be very important to minimize the air side pressure drop. Current state of the art packings provided by companies such as Sulzer Chemtech. [45] can provide extremely low air side pressure drops at high air flow rates. Structured packings can operate at much better conditions than the random Pall ring M16 packings currently used in the setup.

An equally important part is optimizing the fresh water side pressure drop (see section 5.1.4). A possible improvement for optimizing the water side pressure drop is using gravity-based nozzles in the experimental setup [45]. As the name implies, these nozzles do not provide a pressure drop in the system as they operate under gravity conditions. This would mean that only height losses would provide a significant pressure drop on the water side.

Finally, if the psychrometric water production deviation cannot be solved, then operating at lower inlet water temperatures would be the only way to drive mass transfer rates up. One must not forget though, that when using cold ocean water obtained from the ocean instead of using waste water obtained from OTEC, one must also provide the required salt water pump energy requirements.

6.2. Optimization Pilot Plant

This thesis optimized the experimental setup and improved the model to validate experimental results. Optimization for a future pilot plant design is a part left for a future study.

Still, during the process of experimenting, building a model, and validating both experiments and the model, information is obtained that can help with the design of a future pilot plant. Therefore, a quick explanation below is given on how to find optimum values for the main contributors in designing a pilot plant aside from the packing type. These are: the air flow, the water flow, the packing height and the column diameter.

- The air flow is known if the wanted water production of the pilot plant and the tropical air and sea water conditions are known. For instance, if a pilot plant is to produce 25 m^3/day, and 28°C air of 80% relative humidity is to be cooled using a 12°C cold water feed, then the air flow needs to be at least 28.15 kg/s to reach the desired water production rate. This is because air cannot be cooled to a temperature lower than 12°C in this case and from the Mollier diagram or psychrometric chart (see figure 5.17), the maximum kg of water that can be extracted per kg of dry air is then 0.0104 kg water/kg dry air. This gives a minimum flowrate of 27.62 kg/s of dry air needed to be able to extract 25 m^3/day of fresh water, which is a minimum flow rate of 28.15 kg/s of humid tropical air.

- The optimum packing height depends on the efficiency of the packing itself, which for this project, is measured by the water production rate divided by the pressure drop at that height. The specific surface area a and the pressure drop per meter packing $\frac{\delta P}{H}$, both obtained from packing data are quick indicators to identify packing efficiencies. A high specific surface area of the packing will lead to a high water production rate, while the pressure drop per meter packing given by the packing manufacturer should be as low as possible. According to the current improved model and experiments, the packing height for the experimental setup was chosen too large. Lowering the packing height significantly reduced the pressure drop while water production stayed approximately the same See section 5.4 for validation.

- The column diameter and water feed flow are the hardest parts to determine, and are best analyzed by producing a sensitivity analysis using an OTWP model, such as the python model built for this project. Literature stresses the importance of the flooding capacity and that it should be kept below 70% to ensure no sudden increase in pressure drop across the bed. Yet literature does not provide any information on how low the flooding capacity should be for an optimum water production efficiency. This should be identified using a sensitivity analysis. For instance, according to experimental results, increasing the air flow rate of the base case (which automatically provides a higher flooding factor) did not result in a better energy consumption value. See section 5.3 for validation.

6.3. Improvements Experimental Setup:

The experimental setup is analyzed in appendix A. A quick overview as well as some future recommendations are presented here:

- A heater has been added to the TAG. The heater is used together with pressurized steam to regulate the temperature and humidity of the experiment. Prior to adding the heater, only steam was used which resulted in either too high humidities or too low temperatures.

- The system piping diameter was increased where possible and an air blower that could blow air at a higher pressure drop replaced the previous air blower. Prior to resizing, the flow rate of air was unable to reach air flow values anywhere close to values around the gas capacity factor since both the pressure drop was too large and the air blower too weak. The larger piping installation as well as the new air blower resulted that air flow rates of 50 L/s are now possible. This is still too low for flooding, yet high enough to be able to do a sensitivity analysis and test the model. Due to measuring components such as the flow rate sensor, it is not possible to increase the piping diameter further.

- The mixing tube had a butterfly valve to allow the bypass of air flow. This passage has been welded shut to ensure that maximum air flow is possible to the condenser. This setup never had a problem with low air flows, thus the bypass was never missed.

- The water tank is replaced by a tank with smaller dimensions. This ensures that the weight on the weight scale stays below 30 kg. The weight scale automatically turns off once values above 30 kg are reached, making it impossible to measure water production. Thus smaller dimensions are used to ensure the initial weight of the scale is well below 30 kg.

- The temperature sensors have been calibrated and should be recalibrated every 6 months as described by Delver et al. [14]. The last calibration was done in February/March 2017. Obviously it would be best if the temperature sensors were eventually replaced by better sensors, like has been done on the OTEC side. Prior to temperature sensor calibration, it was thought that the sensors would measure the air temperature. After temperature sensor calibration though, it became clear that the temperature sensors measure values close to the packing temperature within the column. However, at the bottom, the temperature sensors tend to tilt more towards the air temperature, while at the top the temperature sensors bend more closely to the water temperature. It is advised to build shells around the temperature sensors within the column, since if the temperature sensor is not in contact with water, the air temperature is measured. This has been verified in section 5.4.1. Measuring the air temperature can help to further improve the validation of the model.

- As previously mentioned, the condenser column has been insulated by wrapping a thick Armaflex slab around it. Prior to insulation, the heat exchange through the condenser column walls were significant [14]. The armaflex slab significantly reduces this heat loss.

6.4. Recommendations:

- Test temperature variation without packing and with the same water flow. This could give a good indication of how well air and water exchange heat and mass without a packing material. This could help improve the experimental model by adding a section to the condenser model that includes mass and heat transfer without packing.

- Increase the column diameter or decrease the column height of the DCD. Increased diameter will result in better water distribution throughout the packing, while a decreased column height can significantly decrease the pressure drop (see section 5.4).

As a side note when searching for new packings, the minimal column diameter needs to be 10x the diameter of a packing ring for the condenser column to function correctly [45]. For instance, our column has 16mm Pall ring packings, and thus the column diameter has to be at least 160mm. The column diameter is 240mm, and thus the condenser column should function correctly.

- Investigate the possibility of perhaps using a thin net or mesh throughout the column instead of a packing. The pressure drop through a net, although not yet tested, is assumed to be relatively low. Also, misting/nebulizing/spraying small droplets of water onto a thin gauze/net/mesh seems like a great way to increase the heat and mass transfer area. This concept of "misting" was also used to extract NOx emmissions from large ships to make sure emmissions were clean(er). Though this idea originally came from a project currently used in the Sahara desert, to obtain water out of the air using compact braided nets. Wind blows air through the braided nets and due to the fact that they are small and tightly braided, water in the air has the tendency to stick to the nets.

- More research is needed to come to definite conclusions on economic feasibility. This thesis validated a model against experimental results. It is recommended that this model be used for a feasibility study to come to definite conclusions if OTWP is a state of the art desalination process.

A

Commissioning

This chapter analyzes all the main components in the fresh water production setup. It also explains some of the steps taken to finish the experimental setup, what solutions were found to deal with unsolved problems and what variables are to be changed to arrive at useful conclusions. For a more thorough analysis of the setup itself, the bachelor and internship reports of Delver et al. [14] and Salet [41] can be used.

A.1. Analysis of Main Components

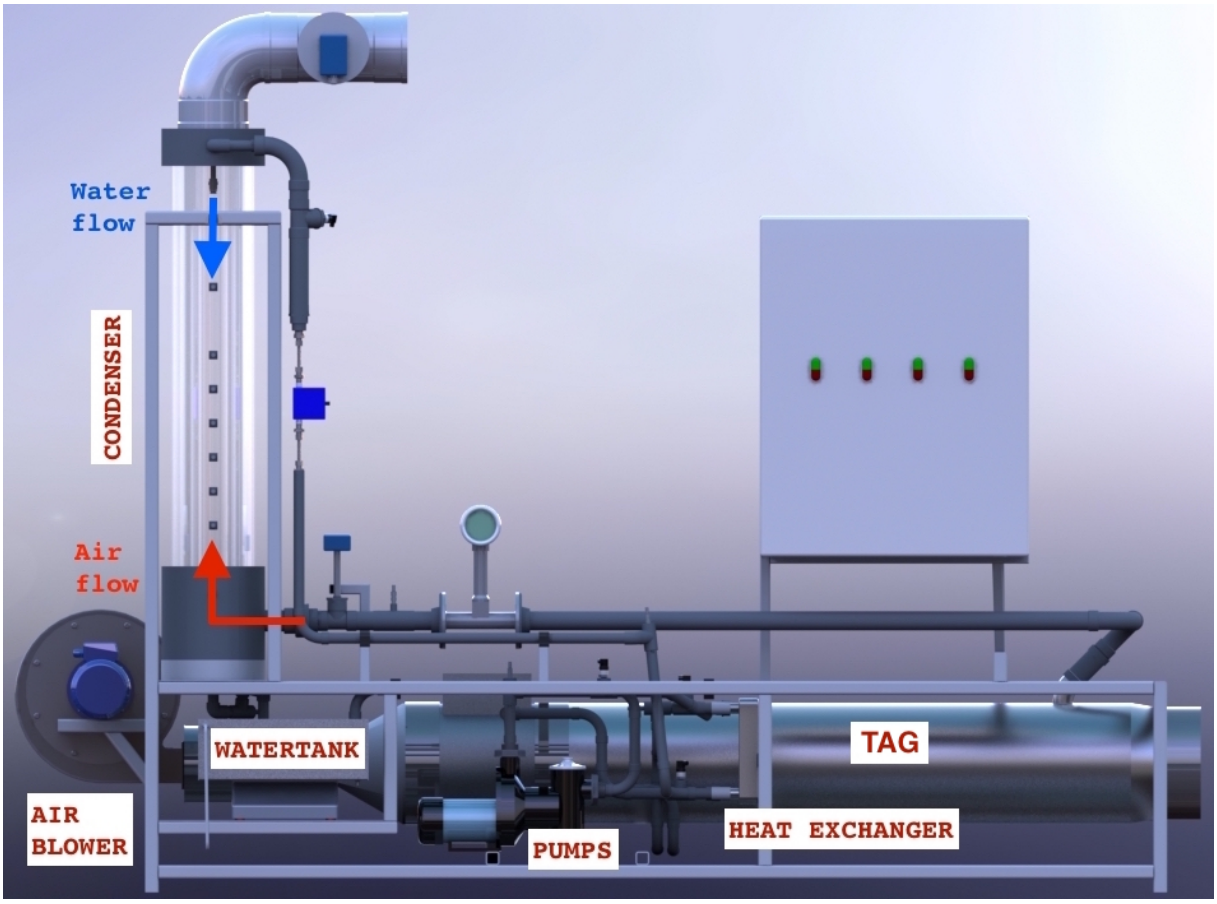

Figure A.1: 3D model design

There are 5 main components needed in a pilot OTWP design: the pumps, the heat exchanger, the direct contact condenser, the spray nozzle, and the air blower. The Experimental OTWP setup also needs an extra heater and steam nozzle added to the air blower to be able to deliver tropical air. These two components together are known to Bluerise as a Tropical Air Generator (TAG). In tropical regions, only the air fan is needed. Each component, its main deliverables as well as its complications will be explained below.

A.1.1. Pumps & Nozzle

The salt and fresh water pumps are responsible for the flow rate of water through the system. It is thus important to choose a pump that is powerful enough to overcome the required pressure drop in the setup needed for the ideal flow rate of salt and fresh water. Also, together with the airfan, the pumps are the only components consuming energy for the final design. Efficiency is maximized if a pump is chosen with the correct operating conditions. Since the nozzle's pressure drop is an important function for the operating conditions of the fresh water pump, it will be handled in this section as well.

Fresh Water and Salt Water Pump

Figure A.2: Fresh and salt water pumps in the experimental setup

The Hydro SS120 water pumps have to be able to overcome the pressure drop at the ideal flow rate conditions. Lopez [30] described the ideal operating point for the DCD column to be reached when the flooding factor is around 0.7. At an air flow rate of 0.19 kg/s, this corresponds to a fresh water flow rate of 0.2 kg/s = 0.72 m^3/hr = 12 L/min.

Lopez [30] ordered the Hydro SS1200 to be used as the current pump for both the fresh water and the salt water side. As can be seen from the pump characteristics below (see figure A.3), the requirements are just met for the fresh water pump.

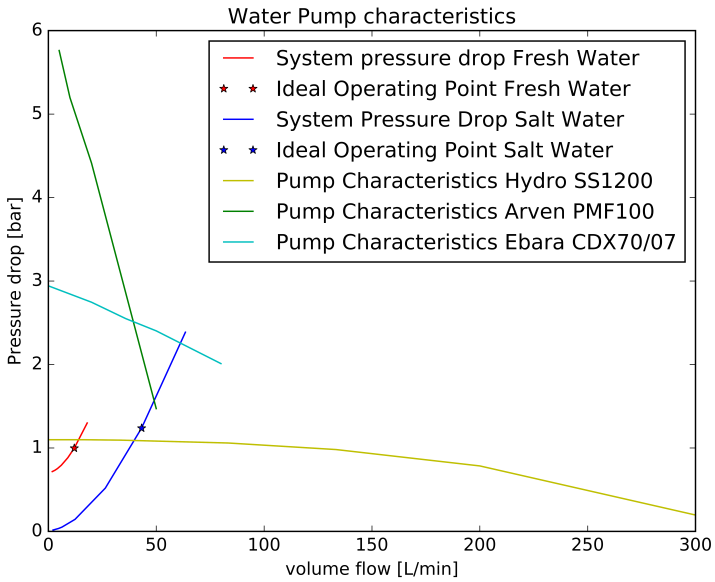

Figure A.3: Salt and Fresh Water Pump Characteristics. Ideal operating points calculated according to Lopez [30] values

This thesis showed that Lopez's operating conditions are far from ideal for the experimental setup. This can be seen in section 3.4.3 as well as in appendix H where the model energy consumption under Lopez operating conditions is shown for this setup. The air flow rate, as well as the fresh water flow rate and salt water flow rate will have to operate at a lower operating point. For the base case condition used in chapter 5 with a water flow rate of 4.5 L/min, both the pumps currently operate at a bare minimum capacity. If the air flow capacity in the condenser column can be increased so that the water flow can increase as well, then the current pumps are a good fit for the experimental setup.

A.1.2. Nozzle

Lopez [30] showed that the pressure drop within the column and nozzle would be the highest pressure drop in the system, it would therefore be best if the pressure drop over the nozzle is:

- low enough so that the pump has sufficient power available for the pressure drop in the heat exchanger, column height and piping
- high enough so that the nozzle can work properly and spray water droplets evenly over the column.

The current nozzle (MP125) delivers a pressure drop that is too high for the pump under Lopez conditions of 12 L/min water flow. In search for a better nozzle at the time, table A.1 was made.

Table A.1: Spraybest Nozzle Comparison

Type	Spray area	Spray Angle	Fitting	Metal	flowrate @ 1 bar	Price	Retailer
MP125	Full cone	60	3/8"	RVS 316	5.5 L/min	50,82 Euro	Spraybest
MP187	Full cone	60	3/8"	RVS 316	12.7 L/min	51,84 Euro	Spraybest
MP218	Full cone	60	1/2"	RVS 316	20.2 L/min	56,81 Euro	Spraybest
TF12	Double Ring	60	3/8"	RVS 316	13.7 L/min	90,64 Euro	Spraybest
WL6	Full cone	60	3/4"	RVS 316	14.1 L/min	74,59 Euro	Spraybest
SC3	Full cone	60	3/4"	RVS 316	16 L/min	40,17 Euro	Spraybest
EZWL4	Full cone	60	3/8"	RVS 316	9.4 L/min	*91,40 Euro*	Spraybest
HEAD49	Shower head	d=20cm	1/2"	Chrome ABS	16 L/min @ 2bar	25 Euro	Hudson Reed

It can be seen from table A.1 that the MP218 delivers the highest flow rate at a pressure drop of 1 bar. This is the best nozzle to work with, since at 12 L/min this nozzle will add the least amount of pressure drop to the total pressure drop on the fresh water side. The MP218 nozzle has thus been used in the setup. The difference in nozzle fitting is easily fixed using a transfer piece. Care must be taken that the nozzle is not too close to the fitting and that it obstructs water spraying over the column evenly. If this threatens to happen anyway, a solution could be to choose a larger spray angle, for instance of 90^o or 120^o.

Instead of using a spray nozzle, another possibility is to use a shower head to spray water into the column. The shower head analyzed comes from the company Hudson Reed and has a diameter of 20 cm. A typical shower head delivers 16 L/min at a pressure drop of 2 bar [40]. Since a normal shower head has no incentive to spray mist or small droplets, it has been verified that the shower head has the lowest pressure drop and thus delivers the highest flow rate. Unfortunately, the air flow pressure drop vastly increased due to the use of the showerhead. A cross nozzle with a lower cross-sectional surface area has therefore been made instead.

As explained in section A.1.1, fresh water flow rates do not need to exceed 4.5 L/min for the current setup. The MP218 nozzle is therefore still used as the basecase option in chapter 5 due to its already low air side pressure drop, and its very low water side pressure drop at this rate.

A.1.3. Heat Exchanger

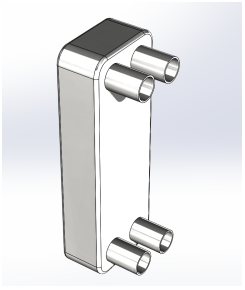

Figure A.4: Solidworks representation of heat exchanger in the experimental setup

Figure A.5: Redenko Cetetherm 410 Heat Exchanger in the experimental setup

The heat exchanger used is a Cetepac type 410Ni-20 compact fully welded plate heat exchanger. The hot and cold streams flow counter-currently through the 1 pass heat ex-

changer. There are 20 plates with 18 effective plates. The hot side has a volume of 0.4 dm3, the cold side volume is 0.5 dm3. The heat transfer and pressure drop over the heat exchanger is described in section 4.4.2. No real changes have been made to the heat exchanger in the experimental setup since the start of this project. Improvements have been made to model this heat exchanger, as is also explained in 4.4.2.

A.1.4. Direct Contact Condenser

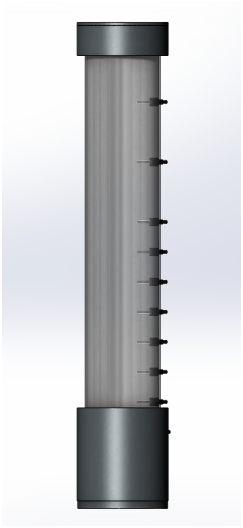

Figure A.6: Representation of condenser column

Figure A.7: 16 mm Pall rings random packing distributed in the condenser column

The DCD is the most important part of the system because it is here that the main product, fresh water, is extracted from air using a cold fresh water loop. The DCD contains a nozzle (explained in A.1.1), a tropical airflow managed by the TAG & fan (explained in A.1.5) and the fresh water flow managed by the fresh water pump (explained in A.1.1). The current experimental design specifications are:

- Diameter condenser column: 0.24 meter
- Height condenser column: 1 meter
- Packing: 50L of Pall ring M-16 (16 mm stainless steel pall ring)
- Nozzle: 0.2 diameter shower cap.

Choice of Packing Material
The metal Pall ring M-16 packing material had been previously ordered by Lopez and is currently used in the condenser column. During the timeframe of this thesis no change to the packing material has been made. The use of plastic random packings would have been interesting to analyze as plastic is much cheaper than metal. Unfortunately, due to the fact that plastic is a non-conductive material, it can build up significant amounts of static electricity. The static electricity build up has already overpowered multiple expensive modules once before, and thus plastic packings were never ordered. It could be interesting to eliminate static electricity by ionization for instance. This is left as work for future projects on the setup.

Temperature and pressure sensors
The DCD has 10 temperature sensors and 1 pressure drop sensor, as is shown in the P&ID in appendix B. Assuming the pressure increases/decreases linearly within the system, we can estimate the pressure at a certain point within the system. The temperature values will be known at different locations, yet difficulties exist whether the temperature values predict air, packing or water temperatures. Currently, the sensors inside the packed bed are said to model the packing temperature. Since the relative humidity, temperature and pressure (=atmospheric) of air is measured at the inlet and outlet of the condenser column, the absolute humidity values of the air in and outflow can be calculated. Since the air flow is measured as well, psychrometric water production rates can be calculated from the experiment (see figure 5.17 in chapter 5).

As briefly explained above, the main concern in the DCD column is the unpredictability of temperature sensor values when running experiments. Water droplets sticking to the sensor temperature sensor influence its temperature. This is because the water provides a protective film layer on the sensor, hereby changing the resistance, which will result in false temperature measurements in the experiment. Also, sensors have direct contact with metal particles, allowing them to interact with packings as well, which further increases the error margin of the sensor. A solution would be to build a protective omhulsel around the sensors, allowing the sensors to only be in contact with air. Once implemented, it is believed that the temperature sensors inside the packing will start to follow the model air temperature curve instead of the model packing temperature curve it tends to do now. This is further explained in the chapter 5.

Water tray and weight scale The Ranger Count 3000 weight scale has a default capacity of 30 kg and a readability of 1 g. Rapid stabilization ensures results are accurate within 1 second.

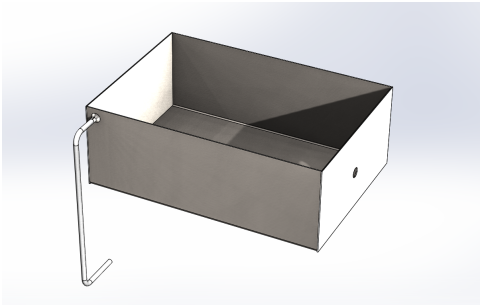

Figure A.8: Solidworks representation of water tray in the experimental setup

Figure A.9: Representation of weightscale used to measure water production in the experimental setup

Due to the fact that the weight scale has a maximum capacity of only 30 kg, the water tray collecting the fresh water was resized to smaller dimensions. This was needed because the fresh water pump needs a high enough water level so that it does not run dry, yet the weight scale needs the water in the tray to not exceed 30 kg. Resizing to smaller dimensions took care of the issue. a drain pipe was also added to the tray so that water would never over flow.

A.1.5. Tropical Air Generator

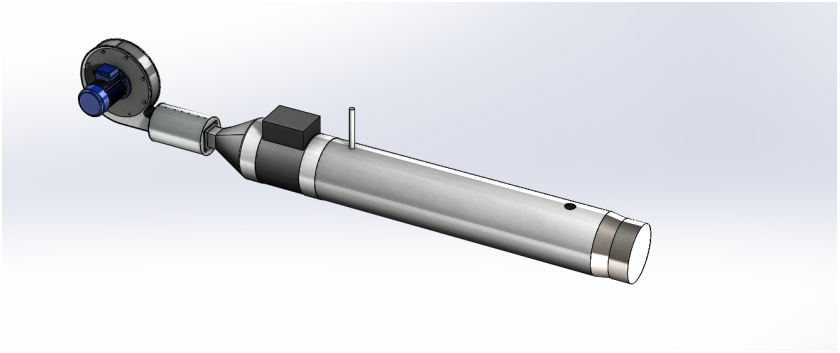

Figure A.10: Solidworks representation of humidifier in the experimental setup

The Tropical Air Generator (TAG), like the name indicates, produces tropical air so that it is possible to experiment under tropical weather conditions. When this thesis project started, the TAG had three main inputs that it could variate and control:

1. the amount of "Dutch air" inflow delivered by the fan
2. the amount of steam delivered to TAG, regulated by an electronic steam valve
3. the amount of humid air entering the DCD, regulated using a bypass valve that bypasses excess air to an external steam tube.

The main purpose is to regulate these three inputs so that the following outputs are true:

- Temperature of the humid air flow is 28 degrees Celsius when entering DCD
- Relative humidity should be able to be 65% as well as 90% when entering DCD
- Humid air flow within DCD must be able to reach 0.19 kg/s

Aligning all inputs to deliver the required output and also be able to change the relative humidity has been a major obstacle during the timeframe of this thesis. The electronic steam valve created short circuit when tested and damaged an output sensor. It has been replaced with a pneumatic steam valve which should be easier to regulate, yet does not give feedback of the flow value of steam. The bypass valve has been welded shut, since all of the (minimal) air flow is wanted inside the condenser column for validation. A heater has been added to the TAG system since it was not possible to arrive at different humidities while at a constant temperature prior to installation.

To arrive at different relative humidity levels one needs to arrive at the correct enthalpy values at a certain temperature and pressure. This can be done by regulating the steam and air inflow. The current humidifier with heater has been modeled in a new python model and is explained in chapter 4. The current TAG system needs approximately 30 minutes to arrive at the wanted temperature and relative humidity and is able to regulate:

1. the amount of "Dutch air" inflow delivered by the fan. All of the air flow will automatically enter the DCD.
2. the amount of steam delivered to TAG, regulated by a pneumatic steam valve

3. the amount of heat added to the air delivered by an external heater.

A.1.6. Air Fan

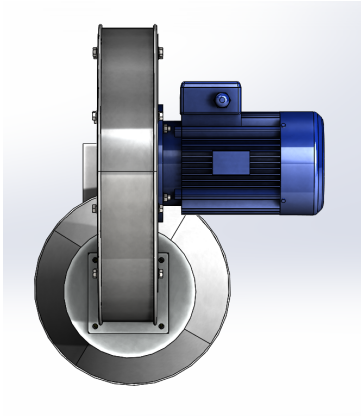

Figure A.11: Solidworks representation of the air fan in the experimental setup

A python model was created to calculate the pressure drop in the TAG at different air flows. The fan air flow supplying the OTWP system of air should be able to overcome a certain pressure drop in order to obtain the wanted air flow rate of 0.19 kg/s according to Lopez [30]. The fan used when this thesis project started was the U/CB 404 from Induvac. The fan was unable to overcome the pressure drop required in the system when an air mass flow of 0.19 kg/s is wanted.

The possibility of a new air fan was suggested, and measurements were done in an empty kolom to calculate the approximate pressure drop that an air flow needs to handle in order to deliver a correct air flow. T. Salet [41] thoroughly described this process in his internship work. Eventuall the U/AP351 was ordered and currently used in the experimental setup.

Unfortunately, as can also be seen in the appendix values of the model at Lopez conditions H, the pressure drop is currently predicted even much higher at air flow rates of 0.19 kg/s. The correct calculation of the system pressure drop is explained in section 4.5.1. The piping diameters have been increased where possible to help increase the air flow as explained by Salet [41]. The current maximum air flow that can be generated in the OTWP experiment using the U/AP351 air blower is 50 L/s (= 0.0575 kg/s).

A.2. Methodology of Experiment

Two important documents provide help to succesfully execute (future) experiments:

- Appendix B shows the start-up and shutdown procedure as well as the process instrumentation diagram (PID) to understand where each component is located.
- Appendix C is a measurement scheme showing which main input variables are changed to analyze the influence this has on the outcome of the experiment. A full overview of experiments can be found in the Bluerise dropbox [10], the measurement scheme

shows only the reliable uncontaminated experiments. The blank spaces are experiments that can still be done.

A list of the relevant input and output variables mentioned in appendix C are shown below. These variables have been determined in accordance with the main objective of this experiment, namely:

1. to find the column formation that results in the highest water production with the lowest possible energy consumption.

2. to correctly calibrate the numerical python model so that the model can be used to help design the larger OTWP plant in Curacao

The main input variables that affect water production and energy consumption are:

- the Relative humidity
- the Water-air ratio
- the Amount of water flow / amount of air flow at the inlet of the condenser column
- the Nozzle types for water distribution
- the Packing material and packing height

The main outputs that fully depend on the input variables above are:

- Temperature distribution in column; obtained through the 10 temperature sensors in the column
- Pressure drop in column; obtained through the 2 pressure sensors in column and the assumption that the pressure changes linearly through the column
- Absolute humidity distribution before and after column; calculated using temperature, relative humidity and pressure drop in column
- Water and air mass flux in column; obtained through mass flow sensors
- Fresh water production in column; obtained by difference in weight of the scale under the water tank
- Energy consumption per m^3 water produced by the system; calculated through the energy consumption of the pumps and the airblower as well as the fresh water production rate

B

Start-up and Shutdown of Experiment

OTWP Demo Startup-Shutdown Procedure

STARTUP PROCEDURE

I. Cooling Pump OTEC side

1. Turn on OTEC side computer, use the following account information:
    1. Username: TUD207947\localadmin
    2. Password: Otecd3m0
2. Start labview interface:
    1. Open “OD cRIO.lvproj – Shortcut” on Desktop (if asked, click Launch Labview)
    2. In OD cRIO.lvproj – Project Explorer window, unfold “RT compact RIO target” and double click “cRIO Main.vi”
    3. In CRIO Main.vi window click the run button(arrow) on the top left
    4. Open “OD host.lvproj - Shortcut” on Desktop
    5. In OD host.lvproj – Project Explorer window, double click “Host Main.vi”
    6. In Host Main.vi window click the run button(arrow) on the top left
3. Wait for half a minute until all values start refreshing properly
4. Go to the tab “water settings”→ “HP-1 Cold water heat pump”→ “HP-1 PWM Period [s]” and make sure this value is 30(this in on the bottom right of the screen)
5. Go to “Cold Water Settings” → “Flow” → “auto” and set “P-3 auto Setpoint” to 0.3kg/s. Move away from the computer and on the physical OTEC demo button cabinet: Turn on “HP-1 Hp-2 P-5” and “P-3
6. When P-3 is on Go to “Water Cycle” tab and in “Cold Water Settings” → “Temperature” → “Auto”, set “TI-03 Auto Setpoint” to 11.5 degC.
7. Move away from the computer and turn on the power button of the heat pump display with label “HP-01”, attached to the left side of the demo button cabinet You should hear one ‘beep’ and ‘bubbling’ which is the start of the cooling.

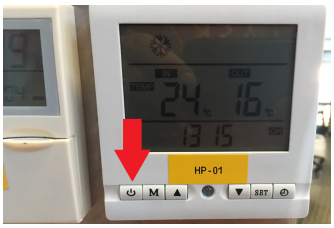

8. Make sure “Cold Water Settings” → “HP-2”is switched off(dark green). It is possible to cool faster with “HP-2” but **make sure it is switched off in time**, otherwise it keeps cooling too far below the desired temperatures.
9. Tip! Handle the OTEC interface easy. When clicking to fast from tab to tab or on random buttons may cause the system to freeze.

II. Steam + Water System checks:

1. Ask lab personnel to turn on steam (Michel, Jaap, or Aad), this takes approximately 15 minutes. (ensure that all steam valves not near setup are also opened and checked by Jaap, Aad or Michel)
2. Make sure the condensed steam valve V-7 is open manually, it is located under the TAG tube (if closed, it should never be closed!)
3. Make sure the steam inlet valve V-2 is closed manually, it is located on the left above the air blower (if it was open, it should not be open!)
4. Open valve V-3 manually (located under V-2) so that all steam air is initially bypassed and does not go into system. Idea is to throw out all condensed steam, so that only vapor steam is still in system (ps: never open bottom red valve V-8, hot condensed water will come out, only Marcel, Jaap or Aad can touch this).
5. After 1 minute or so, fully close valve V-3 and open valve V-2, check that pressure sensor PI-1 is around 4-5 bar. (when opening V-2, always do not open fully, since this can lead to not being able to close it due to temperature expansion)
6. Open valve V-4 so that pressure sensor PI-2 is around 1.5 bar (NOTE: clockwise rotation in this case is opening the valve more, counterclockwise is closing, for other valves it is the other way around)
7. Steam is now stopped at Valve V-6 and does not yet go into system since “Klep V-6” is turned off (will be turned on in next section). Make sure it is turned off by pressing the red button under the label “Klep V-6” on the demo button cabinet.
8. If you need to add fresh water to the system:
    a. Ensure that the “water drain” is placed above water tank so that no water leaves the tank.
    b. Open valve V-1 to add water to the tank using the rubber hose. Enough fresh water should be in the tank so that enough water can be pumped through the system, yet water level needs to be well below top drain as otherwise it will flow out and this will ruin water production measurements (measured using the weight scale MIT-1)

III. System OTWP Side:

Turn on OTWP side computer, use the following account information:

1. Username: TUD208401\localadmin
2. Password: Welkom01
3. Double click “OTWP Control system” on the dashboard
4. Wait for the system to start refresh properly(half a minute) if not redo procedure or call Bram Harmsen: +31-(0)6-164-939-46

Go to “Actuator Control” tab in the Fresh Water Control Interface and:

1. At “P-1 Cold Water Pump” → under “Auto TT-13” → set “P-1 auto Setpoint” to 12 degreesC(if this needs to be another temperature the settings at the OTEC side change too!!)
2. At P-2 Water Pump → under “auto” → set “P-2 auto Setpoint” to a desired fresh water flow set point of e.g. 0.074(50l/s air) or 0.448(30l/s air) for FT-22

Move away from the computer and on the physical OTWP demo button cabinet: Turn on “Pomp P-1” and “Pomp P-2”

Go back to “Actuator Control” tab in the Fresh Water Control Interface and:

1. At “air blower” → “Auto” set desired flow (between 20 and 50 l/s)

Move away from the computer and on the physical OTWP demo button cabinet: Turn on “Vent A-1”

Go back to “Actuator Control” tab in the Fresh Water Control Interface and:

1. At “HC-1 Air Heater” → “Auto” set heater to 28 degreesC
2. At V-1 Steam Valve → under “Manual” → set “V-1 manual Setpoint” to 5%

Move away from the computer and on the physical OTWP demo button cabinet: Turn on “Klep V-6”

Wait for the whole system to settle!

Tips for good experiments:

1. Always check the PID values for “P-1 Cold water pump”, “HC-1 Air Heater”, “V-1 Steam valve” and “HP-1 PWM Period [s]”(OTEC Side) These are the most important parameters to reach steady state and it will be hard to reach steady state if these values are wrong. Look at the screenshots of different experiments to see which values have been used previously.
2. The valve V-13 is closed a little to get the flow through the heat exchanger in the right range. When there is a problem with the value of TT-13, then this can be caused and fixed by opening or closing valve V-13 more.
3. To reach the desired humidity first try to reach the wanted value by tuning the “V-1 manual Setpoint” before switching to automatic! The switch from “manual” to “auto” for the steam valve V-1 is the smoothest when the desired humidity is set before the manual trial and error is done. When this is not the case, quickly set the “auto” desired percentage and switch back to “manual”.
4. If a green button light from P-1, P-2, or A-1 is off then this means that the frequency controller of either one of the pumps or the air blower is malfunctioning. This can be solved by resetting that particular frequency controller by pushing the red button (the button underneath the green button) on the cabinet, then push the green button again to turn it on.

SHUTDOWN PROCEDURE

I. Shutdown Procedure Steam + System checks:

1. Ask lab personnel to turn off steam (Michel, Jaap, or Aad)
2. Fully close steam inlet valve V-2 (you do not have to wait for steam to be turned off, closing V-2 already shuts down steam from OTWP demo). Check that PI-1 and PI-2 go to 0

II. Shutdown Procedure OTWP side:

1. Close the electronic steam valve V-1 using Labview
2. In the “Actuator Control” tab, switch off all processes by going to “Manual” and setting all “Manual Setpoints” to 0
3. Move away from the computer and on the physical OTWP demo button cabinet: Turn off “Klep V-6”, “Vent A-1”, “Pomp P-2” and “Pomp P-1” by pressing their red buttons in this respective order.
4. Close all tabs, click “save changes” when asked, and shut down computer

III. Shutdown Procedure Cooling Pump OTEC side:

1. On the OTEC computer, in the “Bluerise Otec Demo” page, click “STOP” (left handside under “Actions”).
2. Move away from the computer and on the physical OTWP demo button cabinet: Turn off “HP-1 HP-2 P-5”, “Koelpomp P-03”, and “Verlichting” by pressing their red buttons (everything else should be switched off as well, if not switch these off too)
3. Close all tabs, click “save changes” when asked, and shut down computer

Background:

Some things still need to be automated and some bugs need to be fixed, this live document is a way of making sure changes and bugs that have been identified can be implemented and checked, also before they are changed in the software.
Please add anything you think is relevant and let Bram know, so we can fix it and keep improving on the OTEC Demo.

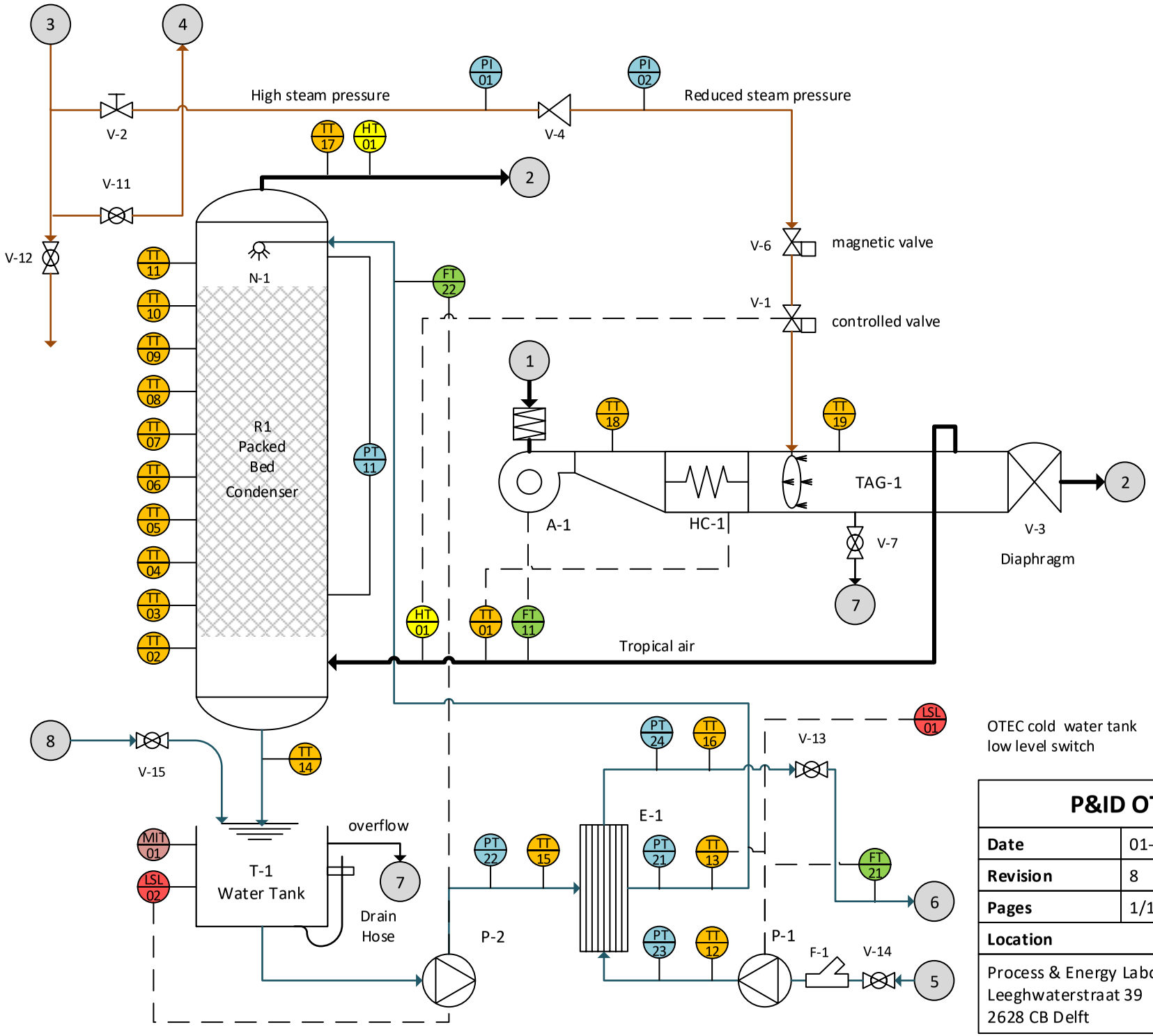

OTEC cold water tank
low level switch

Connections

1	Ambient air inlet
2	Ambient air outlet
3	Steam inlet
4	Steam return
5	OTEC cold water in
6	OTEC cold water out
7	Drain
8	Drinking water

Sensors

TT 01	Temperature transmitter
PT 01	Pressure transmitter
FT 11	Flow transmitter
HT 01	Humidity transmitter
MIT 01	Scale
LSL 01	Low level switch

P&ID OTWP demo installation

Date	01-06-2017
Revision	8
Pages	1/1
Location	

Process & Energy Laboratory
Leeghwaterstraat 39
2628 CB Delft

TU Delft Delft University of Technology

Bluerise harnessing the ocean's power

C

Measurement Scheme

Measurements Procedure

1. Startup procedure as described in the Start-up Shutdown checklist. If there are problems in the system, use the shutdown procedure as described in the Start-up Shutdown checklist.
2. Wait until a steady state situation is achieved, and the following sensors transmit constant values:
    a. Fresh water flow rate sensor FT-22 must have the desired flow rate
    b. Sea water flow rate sensor FT-21 must have the desired flow rate
    c. Temperature of cold incoming seawater TT-17 in external heat exchanger must be constant (under steady state conditions).
    d. Humid air flow rate sensor FT-11 must have the desired flow rate
    e. Humid air temperature sensor TT-01 must have desired tropical air temperature
    f. Humid air humidity sensor HT-01 must have the desired relative humidity of 80% (initial value, will be changed later on)
3. Move away from computer and see if absolute weight on weight scale is well below 30 kg, as the scale does not measure weights above 30 kg. Write down weight of weight scale and now calibrate scale by setting the starting point to 0 kg by clicking ‘Tare’ on weight scale. Note: the scale might fluctuate when system is running due to impulses of dropping water in the tank, this is fine and a mean value can be calculated when system is running.
4. If the steady state values above have been reached and the weight scale has been calibrated, start the following measurements:
5. Measurables Heat Exchanger (HEX):
    a. Measure the temperature of the cold fresh water out of the heat exchanger using sensor TT-13
    b. Measure the pressure drop in heat exchanger on the fresh water side using the difference in pressure sensors PT-21 and PT-22
6. Measurables Direct Contact Condenser (DCC):
    a. Measure the water production using the weight scale under the tank (MIT-1)
    b. Measure the pressure difference over the condenser using pressure sensor PT-11.
    c. Measure the temperature profile in the condenser using TT-02 t/m TT-11. Obviously the expectation is that temperature decreases with increasing height.
    d. Measure the humidity of air at the top of condenser (HT-2). Note: expected is that the air at the top has a relative humidity of 100%.
7. Measurables Pumps:
    a. Measure the pump work done using labview, in Curacao this is the energy input needed to keep the system running and thus also determines the cost of water production.
8. Double check during measurements that steady state values of fresh water flow, sea water flow and air flow remain constant.
9. Save results (stop clock).
10. Close down procedure as described in the document.

Methodology of Experiment

The main objective for OTWP experiments is to find the column formation that results in the highest water production with the lowest possible energy consumption. Furthermore, values obtained from the experiment can be used to correctly calibrate the numerical python model so that the model can be used to help design the larger OTWP plant in Curacao.

The main variables in this plant that affect water production and energy consumption are:

- Relative humidity of air inlet
- Flooding percentage: depends on the column diameter, the total amount of water inlet, the total amount of air inlet and the ratio between water and air in the column.
- Nozzle types: shower head with larger pressure drop in column yet less pressure drop in water flow or spray nozzle with larger pressure drop in water flow yet less pressure drop in column. Also perhaps dependent on which theory is better, droplet-flow theory or film theory
- Packing material (plastic or metal) + good column isolation

The outputs that matter most are:

- Temperature distribution air/water in column over height (from Temp sensors TT-03 t/m TT-011 = precies 1 meter)
    - (TT-02 = -11 cm), TT-03 = 0 cm, TT-04 = 10 cm, TT-05 = 20 cm, TT-06 = 30 cm, TT-07 = 40 cm, TT-08 = 50 cm, TT-09 = 60 cm, TT-10 = 80 cm, TT-11 = 100 cm
- Temperature distribution water side in column over height (from tu=he 2 water temp sensors TT-13 and TT-14 located before and after column)
- Fresh water production in tank over time (from weight scale MIT-1)
- Pressure drop in column over time (from pressure difference sensor PT-11)
- Mass flowrate in kg/s over time instead of the current L/s:
    - Easy for waterside since water can be assumed incompressible and thus density is assumed to remain constant at different pressures, thus density is only a function of temperature.
    - For air a bit harder since we will need RH sensor, pressure sensor, en temperature sensor in order to obtain the density of air (a compressible gas) so that we can convert from L/s to kg/s.
        - Use coolprop to analyze these values or also see: https://www.gribble.org/cycling/air_density.html
        - PROBLEM: Pressure is not measured at air inlet, ideally place a pressure sensor before air inlet.
- **Power consumption graph wanted for OTEC pump, fresh water pump, and the air blower. Ideal situations can also be calculated using data obtained from pressure sensors and mass flow sensors.**
- Absolute humidity distribution in column → can perhaps be obtained using mollier diagram/psychrometric chart and the known temp and pressure in column at each location in the column
- Water and air mass flux in column → can be obtained from mass flowrate and tube/condenser column cross sectional area

The measurement scheme below should be followed and filled in for the first couple of test runs:

MEASUREMENT SCHEME 2017 (M16 PALL RING PACKING AND 0.24M COLUMN DIAMETER)

Packing height 1130 mm

70% RH

80% RH

Nozzle type	FMP218
Packing height (mm)	1130
TT-13 (degC)	12
FT-11 (L/s)	30
FT22 (L/s)	**0.0748**
HT-01 (%)	80

90% RH

Nozzle type	FMP218
Packing height (mm)	1130
TT-13 (degC)	12
FT-11 (L/s)	30
FT22 (L/s)	**0.0748**
HT-01 (%)	90

Nozzle type	MP125(low)
Packing height (mm)	1130
TT-13 (degC)	12
FT-11 (L/s)	30
FT22 (L/s)	**0.0748**
HT-01 (%)	90

Packing height 690 mm

70% RH

Nozzle type	FMP218
Packing height (mm)	690
TT-13 (degC)	12
FT-11 (L/s)	30
FT22 (L/s)	**0.0748**
HT-01 (%)	70

80% RH

Nozzle type	FMP218
Packing height (mm)	690
TT-13 (degC)	12
FT-11 (L/s)	30
FT22 (L/s)	**0.0748**
HT-01 (%)	80

Nozzle type	No nozzle
Packing height (mm)	690
TT-13 (degC)	12
FT-11 (L/s)	30
FT22 (L/s)	**0.0748**
HT-01 (%)	80

90% RH

Nozzle type	FMP218
Packing height (mm)	690
TT-13 (degC)	12
FT-11 (L/s)	30
FT22 (L/s)	**0.0748**
HT-01 (%)	90

Nozzle type	No nozzle
Packing height (mm)	690
TT-13 (degC)	12
FT-11 (L/s)	30
FT22 (L/s)	**0.0748**
HT-01 (%)	90

Packing height 285 mm

70% RH

Nozzle type	FMP218
Packing height (mm)	285
TT-13 (degC)	12
FT-11 (L/s)	30
FT22 (L/s)	**0.0748**
HT-01 (%)	70

80% RH

Nozzle type	FMP218
Packing height (mm)	285
TT-13 (degC)	12
FT-11 (L/s)	30
FT22 (L/s)	**0.0748**
HT-01 (%)	80

90% RH

Nozzle type	FMP218
Packing height (mm)	285
TT-13 (degC)	12
FT-11 (L/s)	30
FT22 (L/s)	**0.0748**
HT-01 (%)	90

Packing height 200 mm

70% RH

80% RH

Nozzle type	FMP218
Packing height (mm)	200
TT-13 (degC)	12
FT-11 (L/s)	30
FT22 (L/s)	**0.0748**
HT-01 (%)	80

Nozzle type	Cross Nozzle
Packing height (mm)	200
TT-13 (degC)	12
FT-11 (L/s)	30
FT22 (L/s)	**0.0748**
HT-01 (%)	80

90% RH

Nozzle type	FMP218
Packing height (mm)	200
TT-13 (degC)	12
FT-11 (L/s)	30
FT22 (L/s)	**0.0748**
HT-01 (%)	90

Nozzle type	Cross Nozzle
Packing height (mm)	200
TT-13 (degC)	12
FT-11 (L/s)	30
FT22 (L/s)	**0.0748**
HT-01 (%)	90

Packing height 1130 mm en FT-22 = 0,0488 L/s

70% RH

Nozzle type	FMP218
Packing height (mm)	1130
TT-13 (degC)	12
FT-11 (L/s)	30
FT22 (L/s)	0.04488
HT-01 (%)	70

Nozzle type	No nozzle
Packing height (mm)	1130
TT-13 (degC)	12
FT-11 (L/s)	30
FT22 (L/s)	0.0448
HT-01 (%)	66

80% RH

Nozzle type	No nozzle
Packing height (mm)	1130
TT-13 (degC)	12
FT-11 (L/s)	30
FT22 (L/s)	0.0448
HT-01 (%)	80

90% RH

Nozzle type	No nozzle
Packing height (mm)	1130
TT-13 (degC)	12
FT-11 (L/s)	30
FT22 (L/s)	0.0448
HT-01 (%)	90

Packing height 690 and FT-22 = 0,0488 L/s

70% RH

80% RH

90% RH

Packing height 285 and FT-22 = 0,0488 L/s

70% RH

80% RH

90% RH

Packing height 200 and FT-22 = 0,0488 L/s

70% RH

80% RH

90% RH

Nozzle type	FMP218
Packing height (mm)	200
TT-13 (degC)	12
FT-11 (L/s)	30
FT22 (L/s)	0.0488
HT-01 (%)	90

Nozzle type	Cross Nozzle
Packing height (mm)	200
TT-13 (degC)	12
FT-11 (L/s)	30
FT22 (L/s)	0.0488
HT-01 (%)	90

Packing height 1130 and FT-11 = 40 L/s

70% RH

80% RH

90% RH

Packing height 690 en FT-11 = 40 L/s

70% RH

80% RH

Nozzle type	FMP218
Packing height (mm)	690
TT-13 (degC)	12
FT-11 (L/s)	40
FT22 (L/s)	0.0748
HT-01 (%)	80

90% RH

Nozzle type	FMP218
Packing height (mm)	690
TT-13 (degC)	12
FT-11 (L/s)	40
FT22 (L/s)	0.0748
HT-01 (%)	90

Packing height 285 mm and FT-11 = 40 L/s

70% RH

80% RH

Nozzle type	FMP218
Packing height (mm)	285
TT-13 (degC)	12
FT-11 (L/s)	40
FT22 (L/s)	0.0748
HT-01 (%)	80

90% RH

Nozzle type	FMP218
Packing height (mm)	285
TT-13 (degC)	12
FT-11 (L/s)	40
FT22 (L/s)	0.0748
HT-01 (%)	90

Packing height 200 and FT-11 = 40 L/s

70% RH

80% RH

90% RH

D

Billet & Schultes

Table D.1: Billet and Schultes Characteristics for Random Packings [7] [8] [9] [42] [47]

Characteristics from Billet and Schultes

Packing	Material	Size $[mm]$	N $[1m^-3]$	a $[m^2/m^3]$	ϵ	F_p $[m^{-1}]$	C_l	C_{fl}	C_h	C_p	C_L	C_G
Bialecki	Metal	50	6,278	121.0	0.966		2.916	1.896	0.798	0.719	1.721	0.302
rings		35	18,200	155.0	0.967		2.753	1.885	0.787	1.011	1.412	0.390
		25	48,533	210.0	0.956		2.521	1.856	0.692	0.891	1.461	0.331
Hiflow	Metal	50	5,00	92.3	0.977	52.5	2.702	1.626	0.876	0.421	1.168	0.408
rings		25	40,790	202.9	0.962	137.8	2.918	2.177	0.799	0.689	1.641	0.402
	Plastic	90		69.7	0.968	29.5				0.276		
		50	6,815	117.1	0.925	56.6	2.894	1.871	1.038	0.327	1.478	0.345
		25	46,100	194.5	0.918		2.841	1.989		0.741	1.577	0.390
Pall	Metal	50	6,300	112.6	0.951	88.6	2.725	1.580	0.784	0.763	1.192	0.410
rings		35	19,517	139.4	0.965	131.2	2.629	1.679	0.644	0.967	1.012	0.341
		25	53,900	223.5	0.954	183.7	2.627	2.083	0.719	0.957	1.440	0.336
		16	210,000	316.0	0.933	315			0.590	0.990		
	Plastic	50	6,765	111.1	0.919	85.3	2.816	1.757	0.593	0.698	1.239	0.368
		35	17,000	151.1	0.906	131.2	2.654	1.742	0.718	0.927	0.856	0.380
		25	52,300	225.0	0.887	180.4	2.696	2.064	0.528	0.865	0.905	0.446
		15	213,000	350.0	0.870	320						
Raflux	Plastic	15	193,522	307.9	0.894		2.825	2.400	0.491	0.595	1.913	0.370
Ralu	Metal	50	6,300	105	0.975		2.725	1.580	0.784	0.763	1.192	0.345
rings		38	14,500	135	0.965		2.629	1.679	0.644	1.003	1.277	0.341
		25	51,000	215	0.960		2.627	2.083	0.714	0.957	1.440	0.336
	Plastic	50	5,770	95.2	0.983		2.843	1.812	0.640	0.468	1.520	0.303
		38	13,500	150	0.930		2.843	1.812	0.640	0.672	1.320	0.333
		25	36,000	190	0.940		2.841	1.989	0.719	0.800	1.320	0.333
Raschig	Metal	0.3	180,000	315	0.960		3.560	2.340	0.750	0.760	1.500	0.450
Super		0.5	145,000	250	0.975		3.350	2.200	0.620	0.780	1.450	0.430
rings		1	32,000	150	0.980		3.491	2.200	0.750	0.500	1.290	0.440
		2	9,500	100	0.985		3.326	2.096	0.720	0.464	1.323	0.400
		3	4,300	80	0.982		3.260	2.100	0.620	0.430	0.850	0.300
	Plastic	2	9,000	100	0.960		3.326	2.096	0.720	0.377	1.250	0.337
Tellerette	Plastic	25	37,037	190.0	0.930		2.913	2.132	0.588	0.538	0.899	

Table D.2: Billet and Schultes Characteristics for Structured Packings [7] [8] [9] [42]

Characteristics from Billet and Schultes

Packing	Material	Size	a $[m^2/m^3]$	ϵ	C_l	C_{fl}	C_h	C_p	C_L	C_G
Euroform	Plastic	PN-110	110.0	0.936	3.075	1.975	0.511	0.250	0.973	0.167
Gempak	Metal	A2 T-304	202.0	0.977	2.986	2.099	0.678	0.344		
Impulse	Metal	100	91.4	0.838	2.664	1.655	1.900	0.417	1.317	0.327
		250	250.0	0.975	2.610	1.996	0.431	0.262	0.983	0.270
Mellapak	Metal	250 Y	250.0	0.970	3.157	2.464	0.554	0.292		
Montz	Metal	B1-100	100.0	0.987			0.626			
		B1-200	200.0	0.979	3.116	2.339	0.547	0.355	0.971	0.390
		B1-300	300.0	0.930	3.098	2.464	0.482	0.295	1.165	0.422
	Plastic	C1-200	200.0	0.954				0.453	1.006	0.412
		C2-200	200.0	0.900	2.653	1.973		0.481	0.739	
Ralu Pak	Metal	YC-250	250.0	0.945	3.178	2.558	0.650	0.191	1.334	0.385

E

Packing Tables from Mackowiak

Packing	Material	Size			$N \cdot 10^{-3}$ [$1\ m^{-3}$]	a [$m^2 m^{-3}$]	ε [$m^3 m^{-3}$]	G [kg/m^3]	ψ_{Fl} (a) $Re_V < 2100$		ψ_{Fl} (b) $Re_V \geq 2100$		$\psi_{Fl, m}$ (c)	$C_{Fl, 0}$ [−]	μ-factor [−]	φ_P-factor [−]
		$d \cdot 10^3$ [m]	$h \cdot 10^3$ [m]	$s \cdot 10^3$ [m]					K_1	K_2	K_3	K_4				
Pall rings	metal	15	15	0.4	224.0	360.0	0.936	512	10	−0.18	3.23	−0.0343	2.42	0.566	0.500	0.280
by Raschig,	(V2A,V4A)	25	25	0.5	51.5	215.0	0.942	464	10	−0.18	3.23	−0.0343	2.42	0.566	0.500	0.280
VFF, rvt		25	25	0.4	51	215.0	0.956	352	10	−0.18	3.23	−0.0343	2.42	0.566	0.500	0.280
		35	35	0.6	19.0	145.0	0.948	416	10	−0.18	3.23	−0.0343	2.42	0.566	0.500	0.280
		38	38	0.6	16.0	151.8	0.953	376	10	−0.18	3.23	−0.0343	2.42	0.566	0.500	0.280
		50	50	0.8	6.1	110.0	0.952	384	10	−0.18	3.23	−0.0343	2.42	0.566	0.500	0.280
		80	80	1.2	1.6	78.0	0.960	320	10	−0.18	3.23	−0.0343	2.42	0.566	0.500	0.280
		58	58	0.6	6.0	105.0	0.970	240	8	−0.18	2.85	−0.0453	1.95	0.566	0.500	0.417
Pall rings	metal	30 oK	30	0.5	32.5	168.9	0.957	344	10	−0.17	4.13	−0.0522	2.62	0.566	0.260	0.244
by Glitsch	30 P	30 mK	30	0.3	28.5	180.0	0.975	200	8	−0.18	2.85	−0.0453	1.95	0.566	0.270	0.390
Pall rings	plastic	15	15	1.0	215.00	350	0.880	108	10	−0.18	3.23	−0.0343	2.42	0.566	0.572	0.309
by Raschig,	(PP)	25	25	1.3	51.00	220	0.890	99	10	−0.18	3.23	−0.0343	2.42	0.566	0.572	0.309
VFF, rvt		35	35	1.3	18.00	160	0.905	85.5	10	−0.18	3.23	−0.0343	2.42	0.566	0.572	0.309
		50	49	1.3	6.70	110	0.920	72	10	−0.18	3.23	−0.0343	2.42	0.566	0.572	0.309
Pall rings	plastic	37	37	1.3	15.50	148.0	0.912	81.3	10	−0.18	3.23	−0.0343	2.42	0.566	0.572	0.309
by ENVIMAC	(PP)	50	50	1.5	6.70	110.0	0.922	72.0	10	−0.18	3.23	−0.0343	2.42	0.566	0.572	0.309
		80	80	1.6	1.50	66.0	0.957	45.0	10	−0.18	3.23	−0.0343	2.42	0.566	0.572	0.309
Pall rings	plastic	90	90	2.0	1.24	90	0.94	62.5	5.585	−0.021	1.76	−0.0510	1.09	0.566	0.509	0.664
by Raschig	(PP)															

Packing	Material	Size			$N \cdot 10^{-3}$ [1 m^{-3}]	a [$m^2 m^{-3}$]	ε [$m^3 m^{-3}$]	G [kg/m^3]	ψ_{Fl} (a) $Re_V < 2100$		ψ_{Fl} (b) $Re_V \geq 2100$		$\psi_{Fl, m}$ (c)	$C_{Fl, 0}$ [−]	μ-factor [−]	φ_P-factor [−]
		$d \cdot 10^3$ [m]	$h \cdot 10^3$ [m]	$s \cdot 10^3$ [m]					K_1	K_2	K_3	K_4				
Raflux type by rvt	plastic (PP)	90	90	0.8	1.24	86	0.96	38	6.576	−0.21	2.07	−0.0510	1.23	0.566	0.397	0.604
Pall rings	ceramic	25	25	3.0	39.9	220	0.73	670	10.00	−0.18	3.23	−0.0343	2.42	0.566	0.572	0.280
by Raschig		50	50	5.0	6.4	120	0.77	623	12.68	−0.23	3.81	−0.0812	1.93	0.566	0.572	0.430
Białecki	metal	12	12	0.3	420	388.2	0.932	544	11.50	−0.18	3.77	−0.0343	2.82	0.566	1.050	0.158
rings	(prod. 1974)	27	25	0.5	52.0	225.0	0.945	440	10.17	−0.17	4.13	−0.0522	2.66	0.566	0.485	0.208
		38	35	0.6	19.0	155.0	0.950	400	10.17	−0.17	4.13	−0.0522	2.66	0.566	0.485	0.208
		53.5	50	0.8	6.5	110.0	0.965	280	10.17	−0.17	4.13	−0.0522	2.66	0.566	0.485	0.208
	metal	50	50	0.6	6.7	112.4	0.967	264	11.50	−0.18	3.77	−0.0343	2.82	0.566	0.515	0.158
	(prod. 1986)	36	35	0.6	19.0	164.0	0.956	352	11.50	−0.18	3.77	−0.0343	2.82	0.566	0.515	0.158
		25	25	0.6	52.0	223.0	0.954	368	11.50	−0.18	3.77	−0.0343	2.82	0.566	0.515	0.158
	ceramic	100	100	10	–	69.5	0.766	514.8	2.381	−0.04	2.38	−0.038	1.73	0.566	–	0.493
Białecki rings	plastic (PP)	49	49	1.6	6.4	115	0.93	63	10.17	−0.17	4.13	−0.0522	2.66	0.566	0.485	0.028
PSL rings	metal (Al)	50	50	0.4	6.5	115.2	0.9754	66.42	10	−0.18	3.23	−0.0343	2.42	0.566	0.336	0.320
	(V2A, V4A)	50	50	0.4	6.5	115.2	0.9754	200	10	−0.18	3.23	−0.0343	2.42	0.566	0.366	0.320
Glitsch	metal (0.5A)	16	5	–	560.8	356.8	0.955	360	6.53	−0.148	4.330	−0.0920	2.00	0.566	0.383	0.415
rings	(1.0A)	25	8	–	160.0	234.7	0.971	232	5.40	−0.140	3.241	−0.0733	1.75	0.566	0.247	0.475
CMR-304	(1.5A turbo)	34	11	0.4	60.8	176.5	0.974	208	5.40	−0.140	3.241	−0.0733	1.75	0.566	0.247	0.475
	(1.5A)	34	11	0.4	60.8	170.0	0.976	192	5.40	−0.140	3.241	−0.0733	1.75	0.566	0.247	0.475
	(2.0A)	43	14	0.4	33.0	150.7	0.989	88	8.12	−0.180	2.903	−0.0445	1.98	0.566	0.140	0.437
	(2.5A)	51	17	0.4	10.0	123.0	0.989	96	8.12	−0.180	2.903	−0.0445	1.98	0.566	0.175	0.437
	(3.0A)	66	22	0.5	–	101.2	0.988	96	8.11	−0.180	2.903	−0.0445	1.98	0.566	0.175	0.437

Packing	Material	Size			$N \cdot 10^{-3}$ [1 m^{-3}]	a [$m^2 m^{-3}$]	ε [$m^3 m^{-3}$]	G [kg/m^3]	ψ_{Fl} (a) $Re_V < 2100$		ψ_{Fl} (b) $Re_V \geq 2100$		$\psi_{Fl, m}$ (c)	$C_{Fl, 0}$ [−]	μ-factor [−]	φ_P-factor [−]
		$d \cdot 10^3$ [m]	$h \cdot 10^3$ [m]	$s \cdot 10^3$ [m]					K_1	K_2	K_3	K_4				
Glitsch rings CMR-304	plastic (size 1A) (PP) (size 2A)	44	16.5	1.0	25.5	196.2	0.935	58.5	5.0	−0.14	3.00	−0.0733	1.58	0.566	0.350	0.496
		69	24.6	0.9	6.3	130.2	0.941	53.1	10.0	−0.18	3.23	−0.0343	2.42	0.566	0.500	0.345
Top-Pak	metal (V4A)	45	38	0.5	6.85	105	0.975	118	8.0	−0.18	2.85	−0.045	1.95	0.566	0.370	0.474
type VFF	size 1 (Al)	45	38	1.1	6.85	105	0.956	190	8.0	−0.18	2.85	−0.045	1.95	0.566	0.370	0.424
	size 2 (V4A)	80	63	0.7	2.80	75	0.980	160	9.1	−0.18	3.37	−0.045	2.21	0.566	0.270	0.424
VSP rings	metal (size 1)	32	25	0.3	33.5	200	0.972	224	9.1	−0.18	3.37	−0.050	2.20	0.566	0.270	0.38
type VFF	(size 2)	50	40	0.4	7.8	104	0.980	160	9.1	−0.18	3.37	−0.050	2.20	0.566	0.270	0.38
Interpak	metal	10	10	0.3	2000.0	620	0.920	656	12.78	−0.18	5.90	−0.079	3.00	0.566	–	0.107
type VFF		15	15	0.3	565.0	350	0.954	362	12.78	−0.18	5.90	−0.079	3.00	0.566	–	0.107
		20	20	0.4	202.5	225	0.962	301	12.78	−0.18	5.90	−0.079	3.00	0.566	–	0.107
		30	30	0.5	–	160	0.965	275	12.78	−0.18	5.90	−0.079	3.00	0.566	–	0.107
Raschig rings	ceramic	8	8	1.5	500.0	550	0.650	770	34.6	−0.307	6.05	−0.069	3.05	0.566	1.000	0.000
		15	15	2.7	200.0	292	0.667	732.6	34.6	−0.307	6.05	−0.069	3.05	0.566	1.000	0.000
		25	25	4.0	46.0	177	0.693	675.4	34.6	−0.307	6.05	−0.069	3.05	0.566	1.000	0.000
		35	35	4.0	18.5	140	0.710	638	34.6	−0.307	6.05	−0.069	3.05	0.566	1.000	0.000
		50	50	5.0	6.4	98	0.730	594	34.6	−0.307	6.05	−0.069	3.05	0.566	1.000	0.000
		53	50	6.0	6.0	100.5	0.772	636	34.6	−0.307	6.05	−0.069	3.05	0.566	1.000	0.000
		100	100	10.0	0.844	52.5	0.761	525.8	–	–	3.14	−0.0343	2.30	0.566	1.000	0.000

Packing	Material	Size			$N \cdot 10^{-3}$ [1 m^{-3}]	a [$m^2 m^{-3}$]	ε [$m^3 m^{-3}$]	G [kg/m^3]	ψ_{Fl} (a) $Re_V < 2100$		ψ_{Fl} (b) $Re_V \geq 2100$		$\psi_{Fl, m}$ (c)	$C_{Fl, 0}$ [−]	μ-factor [−]	φ_P-factor [−]
		$d \cdot 10^3$ [m]	$h \cdot 10^3$ [m]	$s \cdot 10^3$ [m]					K_1	K_2	K_3	K_4				
Raschig rings	glass	8	8	0.7	500	500	0.726	685	17.508	−0.209	5.264	−0.0525	3.38	0.566	–	0.000
		10	10	1.0	300	450	0.740	650	17.508	−0.209	5.264	−0.0525	3.38	0.566	–	0.000
		15	15	1.5	225	375	0.771	572.5	17.508	−0.209	5.264	−0.0525	3.38	0.566	–	0.000
		20	20	2.0	97.9	243.6	0.793	517.5	17.508	−0.209	5.264	−0.0525	3.38	0.566	–	0.000
		25	25	2.0	54.1	203	0.829	427.5	17.508	−0.209	5.264	−0.0525	3.38	0.566	–	0.000
		40	40	4.0	20	160	0.870	325	17.508	−0.209	5.264	−0.0525	3.38	0.566	–	0.000
		50	50	4.0	6.5	120	0.856	360	17.508	−0.209	5.264	−0.0525	3.38	0.566	–	0.000
Raschig rings	metal (V2A,V4A)	15	15	0.5	240.0	350	0.92	640	36.245	−0.19	12.0	−0.0455	8.18	0.566	2.000	0.000
		25	25	0.8	51.5	220	0.92	640	36.245	−0.19	12.0	−0.0455	8.18	0.566	2.000	0.000
		35	35	1.0	19.0	150	0.93	560	36.245	−0.19	12.0	−0.0455	8.18	0.566	2.000	0.000
		50	50	1.0	6.5	110	0.95	400	36.245	−0.19	12.0	−0.0455	8.18	0.566	2.000	0.000
Nutter rings by Sulzer	metal (no. 0.7)	–	–	0.3	167400	226	0.978	176	11.196	−0.206	3.518	−0.051	2.31	0.693	0.867	0.326
	(no. 1.0)	–	–	0.3	67100	168	0.978	178	11.196	−0.206	3.518	−0.051	2.31	0.693	0.867	0.326
	(no. 1.5)	–	–	0.3	26800	124	0.978	181	11.196	−0.206	3.518	−0.051	2.31	0.693	0.867	0.326
	(no. 2.0)	–	–	0.3	13600	96	0.979	173	11.196	−0.206	3.518	−0.051	2.31	0.693	0.867	0.326
	(no. 2.5)	–	–	0.3	8800	83	0.982	145	11.196	−0.206	3.518	−0.051	2.31	0.693	0.867	0.326
	(no. 3.0)	–	–	0.3	4200	66	0.984	133	11.196	−0.206	3.518	−0.051	2.31	0.693	0.867	0.326
Intalox saddles by VFF	ceramic (1/2″)	12.5	–	–	387.0	327	0.648	774.4	6.664	−0.188	3.969	−0.120	1.465	0.566	0.705	0.560
	(3/4″)	20	13	0.8	136.9	252	0.698	664.4	6.664	−0.188	3.969	−0.120	1.465	0.566	0.705	0.560
	(1.0″)	25	22	3.8	68.0	197	0.704	651.2	15.5	−0.255	3.800	−0.071	2.10	0.566	0.705	0.340
	(1.5″)	38	37	6.1	20.0	133	0.743	565.4	15.5	−0.255	3.800	−0.071	2.10	0.566	0.705	0.340
	(2.0″)	50	42	6.1	9.0	99	0.770	506	15.5	−0.255	3.800	−0.071	2.10	0.566	0.705	0.340
	plastic (1.0″)	25	–	–	90.0	255	0.89	99	–	–	8.11	−0.108	3.20	0.566	0.720	0.048
	(1.5″)	38	–	–	26.0	170	0.91	81	–	–	8.11	−0.108	3.20	0.566	0.720	0.114
	(2.0″)	50	42	2.5	8.5	120	0.91	81	10	−0.18	3.23	−0.034	2.45	0.566	0.652	0.280

Table 6-1a. (continued)

Packing	Material	Size			$N \cdot 10^{-3}$ [1 m^{-3}]	a [$m^2 m^{-3}$]	ε [$m^3 m^{-3}$]	G [kg/m^3]	ψ_{Fl} (a) $Re_V < 2100$		ψ_{Fl} (b) $Re_V \geq 2100$		$\psi_{Fl, m}$ (c)	$C_{Fl, 0}$ [−]	μ-factor [−]	φ_P-factor [−]
		$d \cdot 10^3$ [m]	$h \cdot 10^3$ [m]	$s \cdot 10^3$ [m]					K_1	K_2	K_3	K_4				
Intalox	plastic	50	–	–	5.80	110	0.94	54	3.210	−0.075	3.210	−0.075	1.7	0.566	0.375	0.485
Super saddles		90	–	–	1.25	90	0.96	36	2.315	−0.075	2.305	−0.075	1.2	0.566	0.255	0.640
RMSR	metal	25	–	0.4	–	235	0.96	305	7.397	−0.206	2.325	−0.051	1.44	0.566	0.482	0.555
(Rauschert		40	–	0.4	–	170	0.97	241	10.328	−0.206	3.246	−0.051	2.05	0.566	0.422	0.378
metal		50	–	0.5	–	115	0.97	198	7.397	−0.206	2.325	−0.051	1.44	0.566	0.429	0.555
saddle		60	–	0.5	–	90	0.98	159	7.397	−0.206	2.325	−0.051	1.44	0.566	0.311	0.555
rings)		70	–	0.5	–	67	0.98	116	5.853	−0.206	1.893	−0.051	1.09	0.566	0.504	0.647
by rvt		70	–	0.6	–	67	0.98	138	5.853	−0.206	1.839	−0.051	1.09	0.566	0.504	0.647
IMTP #40	metal	40	27	0.6	52.4	128.7	0.984	128	8.75	−0.18	3.17	−0.050	2.00	0.566	0.273	0.395
I-13 rings TU Wrocław/PL	metal (V2A)	25	25	0.5	51.5	218.5	0.948	416	10.17	−0.17	4.13	−0.0522	2.60	0.566	0.562	0.165
Berl saddles	ceramic	10	10	–	620	386	0.595	891	6.664	−0.188	3.969	−0.12	1.465	0.566	–	0.570
		15	15	–	228	303	0.595	891	7.08	−0.188	3.442	−0.0937	1.566	0.566	–	0.541

(a) $\psi_{Fl} = K_1 \cdot Re_V^{K_2}$ *for* $Re_V < 2100$; (b) $\psi_{Fl} = K_3 \cdot Re_V^{K_4}$ *for* $Re_V \geq 2100$; (c) $Re_V \in \{2100 - 10000\}$
oK = with collar
mK = without collar
prod. = production year

V4A ≡ stainless steel 1.4571 (SS 316Ti)
V2A ≡ stainless steel 1.4301 (SS 304)

Koch-Glitsch Italia S.r.l –Bergamo (Italy)
Sulzer Chemtech AG – Winterthur (Switzerland)
Raschig GmbH – Ludwigshafen (Germany)
rvt ≡ RVT Process Equipment GmbH – Steinwiesen (Germany)
VFF ≡ Vereinigte Füllkörper-Fabriken GmbH & Co. KG – Ransbach-Baumbach (Germany)

F

MaxiPass

MaxiPass®

Maximum Free Passage

DESIGN FEATURES

- Ultimate clog-resistant design with largest free passage available in a full cone nozzle
- Two unique S-shaped internal vanes allow free passage of particles
- High energy efficiency
- Easily handles dirty, lumpy liquids
- Male and female connections
- Flanged connection available
- Patented design

SPRAY CHARACTERISTICS

- High reliability spray performance under the most difficult conditions

Spray pattern: Full Cone
(Square patterns to special order)
Spray angles: 30°, 60°, 90° and 120°*
Flow rates: 2.60 to 3540 L/min
(Flow rates up to 17,000 L/min available; call BETE Applications Engineering for details.)

Wide Angle Metal

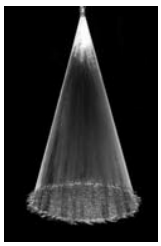

Full Cone 30° (NN)

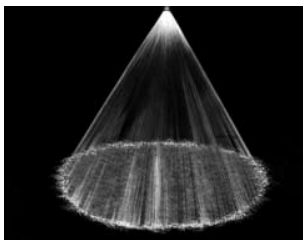

Full Cone 60° (N)

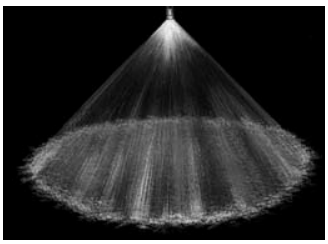

Full Cone 90° (M)

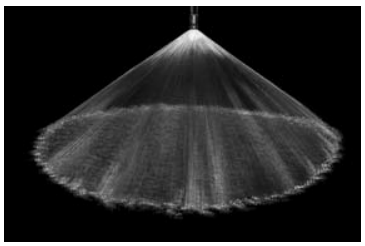

Full Cone 120° (W)

Dimensions are approximate. Check with BETE for critical dimension applications.

MaxiPass Flow Rates and Dimensions

Full Cone, 30° (NN), 60° (N), 90° (M) and 120° (W) Spray Angles, 3/8" to 4" Pipe Sizes, BSP or NPT

Male or Female Pipe Size	Nozzle Number	K Factor	LITERS PER MINUTE @ BAR 0.2 bar	0.3 bar	0.5 bar	0.7 bar	1 bar	2 bar	3 bar	5 bar	Approx. Free Passage Dia. (mm)	Approx. Dimensions (mm) Overall Length 30° A	60° A	90° A	120° A	B	Wt.** (kg) Metal
3/8	MP125	5.53	2.60	3.14	3.99	4.68	5.53	7.66	9.27	11.8	3.18	76.2	38.1	38.1	38.1	22.2	0.09
	MP156	8.79	4.13	4.99	6.35	7.43	8.79	12.2	14.7	18.7	3.97						0.09
	MP187	12.7	5.96	7.21	9.17	10.7	12.7	17.6	21.3	27.1	4.76						0.07
1/2	MP187	12.7	5.96	7.21	9.17	10.7	12.7	17.6	21.3	27.1	4.76	102	47.6	47.6	47.6	25.4	0.13
	MP218	20.2	9.48	11.5	14.6	17.1	20.2	28.0	33.9	43.0	5.56						0.11
	MP250	22.7	10.7	12.9	16.4	19.2	22.7	31.4	38.0	48.4	6.35						0.11
3/4	MP281	27.9	13.1	15.8	20.1	23.6	27.9	38.6	46.8	59.4	7.14	102	63.5	60.3	63.5	31.8	0.23
	MP312	33.8	15.9	19.2	24.4	28.6	33.8	46.8	56.6	72.0	7.94						0.23
	MP343	41.4	19.4	23.5	29.9	35.0	41.4	57.3	69.4	88.2	8.73						0.20
	MP375	48.8	22.9	27.7	35.2	41.3	48.8	67.6	81.8	104	9.53						0.20
1	MP375	48.8	22.9	27.7	35.2	41.3	48.8	67.6	81.8	104	9.53	111	74.6	74.6	74.6	38.1	0.35
	MP406	58.5	27.5	33.2	42.2	49.2	58.5	81.0	98.0	125	10.3						0.33
	MP437	68.4	32.1	38.8	49.4	57.8	68.4	94.7	115	146	11.1						0.33
1 1/4	MP437	68.4	32.1	38.8	49.4	57.8	68.4	94.7	115	146	11.1	137	85.9	85.9	85.9	50.8	0.61
	MP500	87.9	41.3	49.9	63.5	74.3	87.9	122	148	187	12.7	137	85.7	85.7	85.7	50.8	0.61
	MP531	97.6	45.8	55.4	70.5	82.5	97.6	135	164	208	13.5	137	85.7	85.7	85.7	50.8	0.61
	MP562	107	50.2	60.8	77.3	90.5	107	148	179	228	14.3	137	85.7	85.7	85.7	50.8	0.61
1 1/2	MP562	107	50.2	60.8	77.3	90.5	107	148	179	228	13.97	184	111	111	111	57.2	0.91
	MP593	122	57.3	69.3	88.1	103	122	169	205	260	15.1	184	111	111	111	57.2	0.91
	MP625	130	61.0	73.8	93.9	110	130	180	218	277	15.9	184	111	111	111	57.2	0.91
	MP656	158	74.2	89.7	114	134	158	219	265	337	16.7	184	111	111	111	57.2	0.91
	MP687	166	77.9	94.3	120	140	166	230	278	354	17.5	184	111	111	111	57.2	0.91

Flow Rate ($^{l}/_{min}$) = K (*bar*) $^{0.47}$ ** Weights given are for 60°, 90° and 120°

Standard Materials: Brass, 316 Stainless Steel, PVC, Polypropylene, and PTFE. (PTFE not available in 3/8" and 1/2" sizes).

*The spray angle of wide and medium angle whirl nozzles is affected by increasing pressure. Contact BETE Applications Engineering when using the MaxiPass above 3 bar (40 PSI).

Spray angle performance varies with pressure. Contact BETE for specific data on critical applications.

TO ORDER: *specify pipe size, connection type, nozzle number, spray angle, and material.*

A cutaway view of the MaxiPass nozzle showing the S-shaped vanes that enable the nozzle to successfully handle large particles without clogging.

MaxiPass™ Free Passage

Traditional Full Cone Free Passage

A comparison of the free passage available with the BETE MaxiPass nozzle compared to the free passage of a traditional full cone nozzle. The BETE MaxiPass is designed to pass solid particles that are 2-3 times larger in diameter than particles that will pass through a traditional full cone nozzle.

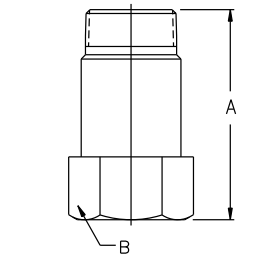

3/8" – 1 1/2" PIPE SIZES

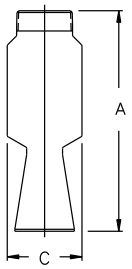

30° (NN)

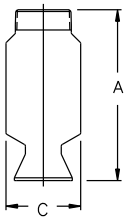

60° (N)

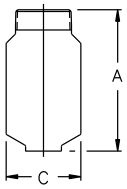

90° (M)

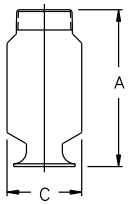

120° (W)

For plastic dimensions, please call BETE Customer Service.

Dimensions are approximate. Check with BETE for critical dimension applications.

MaxiPass Flow Rates and Dimensions

Full Cone, 30°(NN), 60° (N), 90°(M) and 120°(W) Spray Angles, 3/8" to 4" Pipe Sizes, BSP or NPT

Male or Female Pipe Size	Nozzle Number	K Factor	LITERS PER MINUTE @ BAR 0.2 bar	0.3 bar	0.5 bar	0.7 bar	1 bar	2 bar	3 bar	5 bar	Approx. Free Passage Dia. (mm)	Approx. Dimensions (mm) Overall Length 30° A	60° A	90° A	120° A	C*	Wt.** (kg) Metal
2	MP750	202	94.8	115	146	171	202	280	339	430	19.1	210	178	146	159	66.8	1.59
	MP812	221	104	126	160	187	221	306	370	471	20.6	210	183	146	159	66.8	1.59
	MP875	273	129	155	197	231	273	378	458	582	22.2	210	183	146	159	66.8	1.59
	MP937	306	144	174	221	259	306	424	513	652	23.8	229	194	152	165	82.6	1.70
	MP1000	358	168	203	259	303	358	496	600	763	25.4	262	194	152	168	82.6	1.70
	MP1125	439	206	249	317	371	439	608	736	935	28.6	262	194	152	171	82.6	1.70
2 1/2	MP1000	358	168	203	259	303	358	496	600	763	25.4	262	194	152	168	82.6	2.04
	MP1125	439	206	249	317	371	439	608	736	935	28.6	267	213	165	178	82.6	2.04
	MP1250	527	247	299	381	446	527	730	883	1120	31.5	305	244	165	181	82.6	2.04
	MP1375	632	297	359	456	535	632	875	1060	1350	34.9	305	244	213	229	102	2.84
	MP1500	774	363	440	559	655	774	1070	1230	1650	38.1	330	267	213	229	102	2.84
3	MP1500	774	363	440	559	655	774	1070	1230	1650	37.1	343	279	229	248	121	3.29
	MP1625	911	428	517	658	770	911	1260	1530	1940	41.3	343	279	229	251	121	3.29
	MP1750	1040	488	591	751	880	1040	1440	1740	2220	44.5	343	279	229	251	121	3.29
4	MP1750	1040	488	591	751	880	1040	1440	1740	2220	44.5	406	356	225	248	121	3.63
	MP1875	1170	549	664	845	989	1170	1620	1960	2490	47.6	406	356	225	248	121	3.63
	MP2000	1370	643	778	989	1160	1370	1900	2300	2920	49.8	406	356	286	311	152	7.26
	MP2125	1530	718	869	1100	1290	1530	2120	2560	3260	54.0	406	356	286	311	152	7.26
	MP2250	1660	779	943	1200	1400	1660	2300	2780	3540	57.2	406	356	286	311	152	7.26

Flow Rate ($^{l}/_{min}$) = K (*bar*) $^{0.47}$ *C dimension for 30° (NN) is larger **Weights given are for 60°, 90° and 120°

Standard Materials: Brass, 316 Stainless Steel, PVC, Polypropylene, and PTFE.

Spray angle performance varies with pressure. Contact BETE for specific data on critical applications.

G

Model Table Output

MACKOWIAK BASE CASE			
HUMIDIFIER			
Unit	Inlet	Outlet	
T air	20	28	
h steam	2790183.88479		
phi	0.375	0.8	
omega	0.0054542823582	0.0192335922397	
m dot air	0.0347798695071	0.0365136971261	
m dot steam	0.00098727818912		
eta mixing	0.5		
CONDENSER			
Unit	Inlet	H evap = 97.000000	Outlet
T water	11.9937679936	16.1307393525	16.36
T air	28.0	24.7633733305	12.9980259379
m dot water	0.0746256082988	0.0749797924059	0.074962525948
m dot humid air	0.0347798695071	0.0347971359649	0.0344429518578
m dot dry air	0.0341235510406	0.0341235510406	0.0341235510406
omega	0.0191497601915	0.0196557584641	0.00927629629431
a w	56.9606717405	56.9687083242	56.7821792774
k_l	2.44598318956e-05	2.44640673869e-05	2.43623935351e-05
k_g	0.00833919544079	0.00835789978859	0.00831776587178
f	0.113106075588		0.0
dP	0.0	12.5571330445	141.052123221
cond eff			0.951008904389
N hl	0.0253882286607	0.0253914852667	0.0253017482003
Production Model	1.21290353727	kg/hr	
Production Psy	1.21160062521	kg/hr	
Model and psy diff:	0.107536430258	%	
Energy Req. kJ/kg (air fan only)	38.3642941119	kJ/kg produced	
Energy Req. kWh/m^3 (air fan only)	10.6514301064	kWh/m^3 produced	
Energy Req. kWh/m^3 (all press. drop)	12.4111006378	kWh/m^3 produced	

Packing	
naam	Pall Ring M16
D pakking	0.016
a	315
vf	0.93
Phi p	0.28
mu p	0.5
Kolom	
D column	0.24
A kolom	0.0452389342117
z	1.13

PLATE HEAT EXCHANGER		
Unit	Fresh water	OTEC water
T in	16.36	11.3
T uit	11.9937679936	12.7
m dot	0.074962525948	0.233645189246
dP	190.525903467	970.24510493
Volume	0.0004	0.0005
alpha	1688.88720449	7573.24929858
Q	1378.29491235	
U	1334.84692091	
NTU_hex	2.83699621479	
name	Cetetherm CetePac CP410	
L plate	0.25	
B plate	0.111	
psi (wave corr. fact.)	1.22	
number of plates	18	
Effective Area HEX	0.60939	
beta (chevron angle)	30	
plate distance	0.001001001001	

PRESSURE DROP		
Unit	Fresh water	OTEC water
Pipes	19739.737493	15747.7002687
Total system	19930.2633965	16717.9453736

H

Table Output Lopez Cond.

TABLE RESULTS FOR LOPEZ [30]			
OPTIMAL OPERATING POINT			
HUMIDIFIER			
Unit	Inlet	Outlet	
T air	20	28	
h steam	2790183.88479		
phi	0.375	0.8	
omega	0.0054542823582	0.0192335922397	
m dot air	0.201723243141	0.211779443331	
m dot steam	0.00572621349689		
eta mixing	0.5		
CONDENSER			
Unit	Inlet	H evap = 143.000000	Outlet
T water	12.0026507882	20.4942432747	20.76
T air	28.0	24.994583323	14.0305793945
m dot water	0.200337841332	0.202321875519	0.202162015905
m dot humid air	0.201723243141	0.201883102755	0.199899068567
m dot dry air	0.197916596035	0.197916596035	0.197916596035
omega	0.0191497601915	0.0199574722147	0.00993287484677
a w	110.375492985	110.432011959	109.680921382
k_l	5.5926947297e-05	5.59624283566e-05	5.54777138572e-05
k_g	0.0524260100826	0.0525926510659	0.0520150626731
f	0.697833444721		0.0
dP	0.0	739.108170928	5637.45910236
cond eff			0.887767466904
N hl	0.0492167318199	0.0492408119652	0.0488729780226
Production Model	6.56702846449	kg/hr	
Production Psy	6.55503452983	kg/hr	
Model and psy diff:	0.182972867678	%	
Energy Req. kJ/kg (air fan only)	1650.22398707	kJ/kg produced	
Energy Req. kWh/m^3 (air fan only)	458.166137164	kWh/m^3 produced	
Energy Req. kWh/m^3 (all press. drop)	460.069036477	kWh/m^3 produced	

Packing		
naam	Pall Ring M16	
D pakking	0.016	
a	315	
vf	0.93	
Phi p	0.28	
mu p	0.5	
Kolom		
D column	0.24	
A kolom	0.0452389342117	
z	1.13	
PLATE HEAT EXCHANGER		
Unit	Fresh water	OTEC water
T in	20.76	2
T uit	12.0026507882	16.4
m dot	0.199900069195	0.121216546451
dP	1006.9987424	323.931674031
Volume	0.0004	0.0005
alpha	3476.13098019	4481.49696293
Q	7341.93684085	
U	1866.31272871	
NTU_hex	2.76074018274	
name	Cetetherm CetePac CP410	
L plate	0.25	
B plate	0.111	
psi (wave corr. fact.)	1.22	
number of plates	18	
Effective Area HEX	0.60939	
beta (chevron angle)	30	
plate distance	0.001001001001	
PRESSURE DROP		
Unit	Fresh water	OTEC water
Pipes	42743.6068491	4994.30307119
Total system	43750.6055915	5318.23474522

Model Inputs

'INPUT PROPERTIES OF MODEL:'

'Fluid properties'

```
# Volumetric Flows Fresh Water and Air
Vdot_g = 30          #[L/s] Volume flow in gas (FT-11)
Vdot_l = 0.075       #[L/s] Volume flow in liquid (FT-22)
```

'Temperatures Air and Fresh and Salt Water'

```
T_l_in = 12          #[C] temperature fresh water in CONDENSER (TT-13)
T_l_out_ass = 17     #[C] assumption temperature fresh water out CONDENSER (TT-14)
T_l_otec_from = 2    #[C] temperature cooling salt water in HEX (from otec) (TT-12)
T_l_otec_to = 12.7   #[C] assumption for temperature cooling salt water out HEX (to otec)
```

'At steady state conditions'

```
T_g = 28                  #[C] temperature air in CONDENSER (TT-01)
phi_in = 0.9              #[%] Relative humidity air condenser inlet (HT-01)
P_atm = 101325            #[Pa = N/m2] pressure inlet air and inlet fresh water (assumed
atmospheric for both) (PT-11)
```

'Model Properties'

```
T_rs = 0.1          #[degC] maximum difference allowed output temperature water
dt = 0.08           #[degC] step size temperature iteration (make it the same as bandwidth
for speed)
Fl_rs = 0.01        #[kg/m2.s] maximum difference allowed output mass flux water
df = 0.005          #[kg/m2.s] step size mass flux iteration (make it the same as bandwidth
for speed)
dz = 1e-3           #[m] step size height
ec = "evap"         #["name"] "evap" = evaporative cooling
                    #["name"] "noevap" = cooling with no mass transfer
project = "pilot" #["name"] if project = "experiment: experimental setup, use TAG model.
                    #["name"] if project = "pilot": pilot plant facility, no need for  TAG model.
condenser = "mackowiak"    #["name"] Choose "billet", "mackowiak" or "Onda". Determines
which condenser value is to be used
```

'Column Properties'

```
startpack = 0        #[m] height at which packing starts
startpress = 0       #[m] height at which pressure difference measurement starts
z = 1.130#1.13 #0.2 #1.27    #[m] total height of packing
D_t = 0.24           #[m] diameter of column
A_t = (np.pi*D_t**2)/4  #[m2] area of the column
```

'Packing Properties'

```
# Information can be found in Ocean Thermal Water demo --> Components -->
# Packings --> '16mm Metallic Pall Rings.pdf'
name_p = "Pall Ring M16"
D_pack = 0.016       #[m] packing diameter (packing data)
vf = 0.93            #[-] void fraction (packing data)
```

a = 315 #[m2/m3] specific area packing constant (packing data)
sig_c = 0.0728 #[N/m] critical surface tension packing (Klausner/Onda)
Phi_p = 0.280 #[-] form factor from empirical relation table 1 Mackowiack 2011 [ref 37 Lopez]
mu_p = 0.500 #[-] form factor from empirical relation table 6-1a Mackowiack 2010 [ref 36 Lopez]
K1 = 10 #[-] Packing specific constant table 6-1a Mackowiack 2010 [ref 36 Lopez]
K2 = -0.18 #[-] Packing specific constant table 6-1a Mackowiack 2010 [ref 36 Lopez]
K3 = 3.23 #[-] Packing specific constant table 6-1a Mackowiack 2010 [ref 36 Lopez]
K4 = -0.0343 #[-] Packing specific constant table 6-1a Mackowiack 2010 [ref 36 Lopez]
C_T = 1. #[m] Constant used for Sauter mean diameter (Mackowiack 2011 paper), valid for big deformed droplets with sig_l>15mN/m
C_m = 6 #[-] Constant evaluated from experimental data (Mackowiak 2015)
C_n = 1 #[-] Constant evaluated from experimental data (Mackowiak 2015)
C_v = 0.0285 #[-] Constant evaluated from experimental data (Mackowiak 2015)
degree = 45 #[deg] angle of flow channels in column (See Mackowiak 2010 book page 72-77)
C_h = 0.59 #[-] Packing specific constant (Billet Schultes)
C_L = 1.440 #[-] Packing specific constant (Billet Schultes)
C_G = 0.336 #[-] Packing specific constant (Billet Schultes)
Cff = 2.083 #[-] packing specific constant (Billet 1999 from table 2)
C_p0 = 0.957 #[-] Packing specific constant for pres. drop (Billet 1999, took 25mm Pall Rings constant)

'Air Fan/Water Pump Efficiencies'
phi_f = 0.4 #[-] assumed air fan efficiency
phi_b = 0.88 #[-] belt efficiency for air fan<10kW (see fan efficiency engineering toolbox)
phi_m = 0.87 #[-] motor efficiency for air fan<10kW (see fan efficiency engineering toolbox)
phi_pump = 0.7 #[-] water pump efficiency

'Heat Exchanger Properties'
# Information can be found in Ocean Thermal Water demo --> Components -->
# full data --> Heat Exchanger --> 'Heat exchanger - Cetetherm 410.pdf'
name_he = "Cetetherm CetePac CP410"
L_p = 0.25 #[m] length of the plates
B_p = 0.111 #[m] width of the plates
delta = 0.4e-3 #[m] plate thickness
n = 18 #[-] number of effective plates
psi = 1.22 #[-] correction for wave in plates
beta = 30 #[degree] chevron angle
D_port = 0.025 #[m] port diameter
V_h = 0.4e-3 #[m3] volume hot side
V_c = 0.5e-3 #[m3] volume cold side

```
   dev = 50          #[W] maximum difference allowed of the calculated total heat transfer
with the given total heat transfer
   Ft = 0.95         #[-] correction factor for the maximum log mean temperature difference
(which is the maximum mean temperature difference that can be achieved)
   fouling = 30000     #[W/m2K]fouling factor fresh water
   lamda_ss = 16      #[W/m.K] thermal conductivity stainless steel (see
http://www.engineeringtoolbox.com/thermal-conductivity-d_429.html)

   # Pressure Drop Constants HEX for determining the friction coefficients
   B0 = 64
   B1 = 597
   C1 = 3.85
   aa = 3.8

   'Tubing Properties'
   # Properties obtained by measuring tubing and equipment in Ocean Thermal Water demo

   # Fresh Water
   tubing_l = [[2, 0.032], [0.5,0.008], [2,0.01]]  #(length [m], diameter [m]) all tubing fresh
water
   equipment_l = [[2.5, 0.032, 4],[1.3, 0.032, 2], \
   [1, 0.032, 1],[1, 0.016, 1], [0.24, 0.05, 1],   \
   [0.04, 0.032, 1], [0.04 ,0.008, 1],           \
   [0.36,0.032,1],[3,0.016,1]] #(friction factor [-], diameter [m], number count[-]) all
equipment fresh water
   dP_nozzle = 0#5e3          #[Pa] pressure drop nozzle
   H_l = 1.5 #2             #[m] elevation height fresh water
   dP_foot = 0#1e3           #[Pa] pressure drop foot valve

   # Otec Salt Water
   tubing_otec = [[8 , 0.032], [0.5, 0.008]]          #(length [m], diameter [m]) all tubing otec
salt water
   equipment_otec = [[2.5, 0.032, 7], [2, 0.05, 2],     \
   [1, 0.032, 2], [1.3, 0.032, 2], [0.04, 0.008, 1],    \
   [0.024, 0.032, 1], [0.24, 0.05, 1],[0.04, 0.032, 1]] #(friction factor [-], diameter [m], number
count[-]) all equipment otec salt water
   H_otec = 0               #[m] elevation otec water cycle


   'Values Needed for TAG model'
   phi_lab = 0.375        #[%] Relative humidity lab
   T_lab = 20           #[C] temperature lab
   T_steam = 170         #[C] volgens Jaap van Raamt van P&E lab
   P_steam=5e5           #[Pa] Pressure steam
   eff_humidifier = 0.5    # mixing efficiency humidifier
```

Bibliography

[1] F. Alnaimat, J. Klausner, and R. Mei. Transient analysis of direct contact evaporation and condensation within packed beds. *International Journal of Heat and Mass Transfer*, 54, 2011.

[2] D.R. Baker and H.A. Shryock. A Comprehensive Approach to the Analysis of Cooling Tower Performance. *Journal of Heat Transfer*, 1961.

[3] Q. Bauer, M. Etten, K. Lie, and C. Molhoek. Verdampingskoelen: Drinkwater productie met direct contact condensatie. Bachelor's Thesis, TU Delft, 2014.

[4] R. Billet. Packed Column Analysis and Design. *Ruhr University Bochum*, 1999.

[5] R. Billet and J. Mackowiak. . *Inz. Chem. Proc. (Orig. Engl.)*, (3), 1982b.

[6] R. Billet and J. Mackowiak. Application of modernpackings in thermal separation processes. *Chem. Eng. Tech.*, (11), 1988.

[7] R. Billet and M. Schultes. Predicting Mass Transfer in Packed Columns. *Chem. Eng. Technol.*, (16), 1993.

[8] R. Billet and M. Schultes. Fluid Dynamics and Mass Transfer in the Total Capacity Range of Packed Columns up to Flood Point. *Chem. Eng. Technol.*, (18), 1995.

[9] R. Billet and M. Schultes. Prediction of Mass Transfer Columns with Dumped and Arranged Packings. *IChemE*, 1999.

[10] Bluerise B.V. Information upon request.

[11] K. Bornhutter and A. Mersmann. Mass Transfer with Modern Large Size Packings. *Chem. Ing. Tech.*, (63), 1991.

[12] K. Bornhutter and A. Mersmann. Mass Transfer in Packed Columns: The Cylinder Model. *Chem. Ing. Tech.*, (16), 1993.

[13] E.J. Cussler. Diffusion: Mass transfer in fluid systems. *New York: Cambridge University Press*, 1997.

[14] T. de Vries E.A. van de Zande D.C. Delver, T.M.J. Mersie. Ocean Thermal Water Production: een toevoeging op de Ocean Thermal Energy Conversion. Bachelor's Thesis, TU Delft, 2017.

[15] Ernst R.G. Eckert and Richard J. Goldstein. *Measurement Techniques in Heat Transfer*. Technivision Services, 1976.

[16] H.T.A. El-Dessouky, A. Ai-Haddad, and F. Ai-Juwayhel. A modified analysis of counterflow wet cooling towers. *Journal of Heat Transfer*, 119, 1997.

[17] J. Evans. Centrifugal pump efficiency, 2016. URL `https://www.pumpsandsystems.com/topics/pumps/pumps/centrifugal-pump-efficiency-what-efficiency`.

[18] N. Frössling. Uber die Verdunstung fallender Tropfen. *Gerlands beitr. geophys*, 1938.

[19] C.J. Geankoplis. *Transport processes and separation process principles (2003)*. Prentice Hall, 2003.

[20] Andrzei Gorak and Zarko Olujic. *Distillation: Equipment and Processes*. Elsevier, 2014.

[21] R.J. Goudriaan. Performance analysis of ammonia and ammonia-water as working fluids for Ocean Thermal Energy Conversion power plants. Master's thesis, TU Delft, 2017.

[22] R. Higbie. The rate of absorption of a pure gas into a still liquid during short periods of exposure. *Trans. Am. Inst. Chem. Eng.*, (35), 1935.

[23] R.I. Hirshburg and L.W. Florschuetz. Laminar wavy-film flow: Part ii, condensation and evaporation. *Heat Transfer*, pages 104:459–464, 1982.

[24] J.P. Holman. *Heat Transfer*. McGraw-Hill, 2010.

[25] W. Kays, M. Crawford, and B. Weigand. *Convective Heat and Mass Transfer*, volume 4. McGraw-Hill, 2004.

[26] J. F. Klausner, R. Mei, Y. Li, and J. Knight. Innovative fresh water production process for fossil fuel plants. *University of Florida*, 2003.

[27] J. F. Klausner, Y. Li, and R. Mei. Evaporative heat and mass transfer for the diffusion driven desalination process. *Heat Mass Transfer*, 42, 2006.

[28] F. Kreuk, V. Klaassens, M. van Beurden, and L. van der Bijl. Fresh water production as add-on to ocean thermal energy conversion. Bachelor's Thesis, TU Delft, 2016.

[29] Y. Li, J. Klausner, R. Mei, and J. Knight. Direct contact condensation in packed beds. *Intenational Journal of Heat and Mass Transfer*, 49, 2006.

[30] M. Lopez. Ocean Thermal Water Production. Master's thesis, TU Delft, 2016.

[31] J. Mackowiak. Pressure Drop in Irrigated Packed Columns. *Envicon Engineering*, 1991.

[32] J. Mackowiak. *Fluid Dynamics of Packed Columns: Principles of the Fluid Dynamic Design of Columns for Gas/Liquid and Liquid/Liquid Systems*. Springer, 2010.

[33] J. Mackowiak. Model for the prediction of liquid phase mass transfer of random packed columns for gas-liquid systems. *Chem. Eng. Res. Des.*, (89), 2011.

[34] J. Mackowiak. Progress in design of random packing for gas-liquid system. *Chem. Eng. Res. Des.*, (99), 2015.

[35] J. Mackowiak and R. Billet. New Method of Packed Column Design for Liquid/Liquid Extraction Process with Random and Stacked Packings. *Ger. Chem. Eng*, (1), 1986.

[36] F. Merkel. Verdunstungskuhlung. *VDI Forschungsarbeiten*, (275), 1925.

[37] L.F. Moody. Friction Factors for Pipe Flow. *Transactions of the A.S.M.E*, 66, 1944.

[38] K. Onda, H. Takeuchi, and Y. Okumoto. Mass transfer coefficients between gas and liquid phases in packed columns. *Journal of Chemical Engineering of Japan*, 1968.

[39] F. Osterle. On the analysis of counter-flow cooling towers. *International Journal of Mass and Heat Transfer*, 34, 1991.

[40] Hudson Reed. Hudson Reed Douchekop, 2016.

[41] T. Salet. Improvement of an Ocean Thermal Water Extraction Demo. Internship Thesis, TU Delft, 2016.

[42] J. D. Seader and E. J. Henley. *Separation Process Principles*, volume 2. John Wiley & Sons Inc., 2006.

[43] R. K. Sinnott and G. P. Towler. *Chemical engineering design principles, practice and economics of plant and process design*. Elsevier ltd., 2013.

[44] M. Spyrou. The Diffusion Coefficient of Water. Report, University of Surrey, 2008.

[45] Sulzer Chemtech Nederland B.V. Information obtained from meeting with technical expert.

[46] J.W. Sutherland. Analysis of mechanical-draught counterflow air/water cooling towers. *Journal of Heat Transfer*, 105, 1983.

[47] ThePallRingCompany. 16 mm metal Pall Rings Pressure Drop Graph , march 2016. URL `http://www.pallrings.co.uk/wp-content/uploads/2013/04/16mm_Metal_PR_PressureDrop.jpg`.

[48] The Engineering Toolbox. Fan Power Consumption, 2016. URL `http://www.engineeringtoolbox.com/fans-efficiency-power-consumption-d_197.html`.

[49] S. van der Drift. Atmospheric water extraction with deep ocean water: a techno-economic assessment. Master's thesis, TU Delft, 2014.

[50] VDI. *VDI Heat Atlas*, volume 2. Springer, 2010.

[51] F. M. White. *Fluid Mechanics, 7th edition*, volume 4. McGraw-Hill, 2011.